Femtosecond Photodissociation Dynamics of Alkali Halides

Thesis by

Peijun Cong

In Partial Fulfillment of the Requirements

for the Degree of

Doctor of Philosophy

California Institute of Technology

Pasadena, California

1992

(Submitted September 17, 1991)

To my wife, my parents, and my late great-grandma

Abstract

Femtosecond Transition-State Spectroscopy (FTS) is a time-resolved spectroscopic technique by which the real time dynamics of the transition state of a chemical reaction can be studied with femtosecond resolution. This technique has been applied to study a number of chemical reactions. This thesis presents one such system, the photodissociation of alkali halides, and that of NaI in particular.

Upon excitation to the covalent state, the alkali halide molecule will encounter a curve crossing during its way to dissociation. This curve-crossing phenomenon manifests itself in the dynamics of the photodissociation process. Experimentally, wave-packet trapping and leaking that are due to the curve crossing are observed. Taking full advantage of the femtosecond resolution offered by the FTS technique, the wave-packet dephasing dynamics is separated from the population decay. The Landau-Zener coupling-matrix element is also obtained from the time-resolved data, which is in close agreement with previous literature values. Furthermore, the combination of the temporal resolution and the spectral resolution of the FTS methodology allows the wave-packet motion to be monitored at a specific internuclear separation, which covers a wide range of distances. This feature of the FTS technique makes the mapping of reaction trajectories possible. A classical mechanics-based inversion procedure is then developed to obtain the relevant potential-energy curves involved in the photodissociation reaction from the results of such trajectory mapping experiments. The potentials inverted this way are tested by quantum dynamical simulation and compared with those obtained by other workers from different techniques. The long-time behavior of the wave-packet motion after many oscillations is also discussed.

Acknowledgements

Upon completing this thesis, there are numerous individuals to whom I am thankful. First of all, I would like to express my gratitude to my research advisor, Professor A. H. Zewail, for giving me the opportunity to be involved in a number of interesting and exciting projects and for allowing me the time to explore thoroughly some seemingly simple (but more complex, in reality!) problems. Through the many hours I spent thinking about these problems, I feel I have matured a good deal scientifically.

Among the many past and present members of the Zewail research group who have helped me over the years, I can mention only a few here. Martin Gruebele and Jennifer Herek proofread the whole thesis and their comments not only improved the quality of its English but also the quality of its science. As the one-stop program source of all the computations I carried out, the value of Martin's advice on the calculations presented in this thesis is simply incalculable. The work presented in this thesis resulted from collaborations with many individuals. Chapter 4 is the fruit of collaboration with Dr. Gareth Roberts, Jennifer Herek, and Dr. Amine Mokhtari, while Amine also contributed significantly to the experimental aspects of Chapter 5. I also want to thank Mark Rosker and Todd Rose for laying the groundwork on the FTS of alkali halides, Mark Rosker and Marcos Dantus for constructing the femtosecond laser system employed in this thesis, and Bob Bowman for lending his expertise (magic touch) on more than one occasion when the laser seemed to be hopelessly misaligned.

Besides the work presented in this thesis, I was also involved in the design and construction of a picosecond-laser molecular-beam system with Larry Peng, Jack Breen, and Dean Willberg. Larry introduced me to the nuts and bolts of jet spectroscopy, while Jack taught me about vacuum, electronics, and resourcefulness, *i.e.*, the art of making a functional instrument out of odds and ends. Dean almost single-handedly built the

picosecond mode-locked Q-switched laser system when he was not helping us to fix the vacuum system.

Life at Caltech would not be so enjoyable if it was only for pure research. I happened to share the same office with many interesting individuals who made life in the Zewail group even more interesting. I cannot imagine life in the Sub-Basement of Noyes without those late-night Strawberry Donut runs (a tradition imported from Claremont Colleges by Zeta (Khundkar) and Chuck (Williamson)), the birthday cakes (a tradition left by Jack), the Couch laughters, and those occasionally successfulsoccer/basketball/ volleyball/softball teams fielded out of the Sub-Basement with Michael (Gutmann), Earl (Potter), Søren (Pederson), Larry, Bob, and K. D., among many others. Even though Earl has always taken the wrong side on the heated debate of the virtues of IBM and Macintosh, he is the guy you want to have on your team when the game is basketball. Michael deserves special credit for introducing FEUERZANGENBOWLE to this group and for sponsoring the poolside German reunification party.

Table of Contents

Chapter 1

Introduction

One of the primary goals of modern chemical dynamics is to understand the behavior of chemical reactions at a molecular level.[1] Historically, major breakthroughs in this field have been marked by the introduction and combination of sophisticated experimental and theoretical tools originally developed in other fields. For example, two experimental techniques, molecular beams and lasers, were invented by physicists with no particular chemical applications in mind; however, they revolutionized the study of chemical reaction dynamics.

Molecular beams and crossed-molecular beams were first employed by practicing chemical dynamists in the late 1950's and early 1960's, even though these techniques had been around since the early part of this century. The pioneering work of Herschbach[2] and his contemporaries in molecular-beam chemistry made feasible the observation of chemical reactions under single-collision conditions. This was accomplished by crossing two collisionless beams of reactants so that the only possible collisions would occur between reactant molecules from different beams. The initial conditions of the molecules were controlled by spatial collimation and velocity selection. The post-collision observables were kinetic energies and angular distributions of the scattered molecules, which might be the unreacted molecules or the collision-induced reaction products. These measurements provided valuable information about the energetics and critical geometries of the transition states that led to the chemical reaction. The contributions of molecular-beam chemistry have been reviewed by some of the principal participants.[2-4]

In contrast, lasers, as intense, monochromatic, and coherent light sources, took much less time to find widespread applications in molecular spectroscopy and chemical kinetics studies. The technique of photofragment spectroscopy,[5-7] developed in the early 1970's, is a variation of the crossed-molecular beam experiment in which one molecular beam is replaced by a laser beam. The purpose of this photon beam is to initiate a

dissociation reaction by promoting the reactant molecules to an energized, unstable state, which will eventually fragment. Since this process starts from the transition state, it is also called a "half-collision," as opposed to the "full-collision" processes studied by crossed-molecular beams. The kinetic energy and angular distributions of the photofragments may be measured in similar fashion as in the true, crossed-molecular-beam experiments, or more commonly, may be probed by another laser beam. The latter version of the photofragment spectroscopy is often referred to as the pump-probe method.

For both the crossed-molecular beam method and the pump-probe photofragmentation technique with nanosecond laser pulses, only the post-collision observables can be measured, with a few notable exceptions.[8-10] Some important aspects of the transition states can therefore be inferred only indirectly from such measurements. For example, the lifetime of the transition states is estimated by the anisotropy of the final-product angular distribution and the rotational period of the collision complex. The difficulty in directly measuring the lifetimes lies in the fact that these transition states are very short-lived. Consider a diatomic molecule with a reduced mass of 40 a.m.u. and a bond length of 2 Å; if 1 eV of recoil energy (i.e., 1 eV above the dissociation limit) is deposited by a laser pulse, the terminal velocity of the two atoms flying apart will be 2.2 km/s, or 0.022 Å/fs (1 fs = 1 x 10^{-15} s). If we define that a chemical bond is broken when it is stretched out to twice the initial separation, the time it takes to break the afore-mentioned bond with 1 eV of excess energy will be approximately 90 fs. Therefore, in order to observe such a simple bond-breaking process directly in the time domain, the time resolution required is 90 fs or better. These ultrashort laser pulses were made available in the early 1980's by a research team led by C. V. Shank at Bell Laboratories via the now common ring-cavity colliding-pulse mode-locking technique (i.e., CPM), which is capable of producing 60 fs laser pulses with a wide tuning range.[11]

Zewail and his colleagues at the California Institute of Technology have pioneered

the application of ultrashort laser techniques to study chemical reaction dynamics.[12] Even before the construction of the Femtosecond Laser Facility at Caltech, Scherer, Knee, Smith, and Zewail employed a subpicosecond (0.35 to 0.4 ps) laser source to explore the dissociation dynamics of ICN $\rightarrow$ I + CN; the conclusion these workers reached was that the time resolution provided by the subpicosecond laser pulses was still not adequate to resolve the ultrafast dynamics and to observe the transition state directly.[13] In 1987, after the completion of a CPM-based femtosecond laser system, Dantus, Rosker, and Zewail published the first direct observation of transition states of the ICN photodissociation reaction.[14] Subsequently, many other reaction systems have been studied by this femtosecond transition-state spectroscopy (FTS) technique,[15-20] including the subject of this thesis, the predissociation of NaI.[18] A major effort currently under way in this laboratory is to extend the FTS technique to femtosecond transition-state diffraction (FTD).[21] The goal of FTD is to measure the structural changes of a molecule in a transition state by measuring the electron-diffraction patterns with femtosecond resolution.

The concept of FTS is a simple one (see Figure 1.1). At time zero (defined as the temporal center of the pump pulse), a coherent wave packet is prepared on the excited potential-energy surface (PES) V_1 from ground state V_0, with its center r_0 close to the equilibrium bond length. This wave packet will then evolve under the influence of the excited PES. For the simplified case sketched in Figure 1.1, the wave packet will propagate toward longer internuclear separation. After a certain time delay τ, the system is irradiated by another femtosecond pulse, the probe pulse. The photons in the probe pulse will be absorbed only if the center of the wave packet $r(\tau)$ is at such a configuration that the energy of the photons matches the difference between V_1 and a higher excited state V_2. The FTS signal will then be some measure of the absorption of the probe pulse by the molecules while they are falling apart, as a function of both the delay time τ and the probe wavelength λ. This could be accomplished by measuring the change in the transmission of

the probe. However, such a measurement will not be background-free. The detection of laser-induced fluorescence (LIF) or multiphoton ionization (MPI) caused by the probe pulse would be much better choices.

When the probe wavelength is tuned to match the asymptotic difference between V_1 and V_2 (hc/λ_2^{∞}), the observed FTS signal, produced by LIF from V_2, will reflect the build-up of the free fragment. This kind of experiment is called a "clocking" experiment, since it directly measures the time required to break the chemical bond. When the probe wavelength is detuned from λ_2^{∞} to λ_2^{*}, the free fragments will no longer be able to absorb the probe photon; instead, the molecules in the transition state may do so. The FTS transient will then be expected to build up, as the molecules enter the "window" opened by the probe photon, and subsequently to decay, as the molecules leave the probe window and move on to become free fragments. By constructing a two-dimensional data base, with one dimension being the delay time, and the other one being the wavelength of the probe photon, information about the shape of the PES can be obtained, as has been demonstrated for the case of ICN.[15,16] It is interesting to note that the capability of observing the transition state of FTS relies on two factors: One is obviously the time resolution offered by the femtosecond pump and probe pulses; the less obvious factor is the spectral resolution of the probe pulse that enables the detection of the transition state at a particular configuration. If the probe pulse is an infinitely short δ pulse, then all the spectral resolution is lost; thus, no matter what the delay time is, the molecule will be able to absorb the probe photon, so much of the temporal resolution is lost.

Since the first publication of FTS in 1987, a number of systems have been studied by this technique, including ICN, NaI, HgI_2, I_2, and Bi_2. Interested readers should consult a continuing series of papers[15-20] published by Zewail and his coworkers,

(subtitled FTS I through VI thus far). The Ph.D. thesis by Dantus is also an excellent source to find much of ground work about FTS, especially the experimental apparatus employed in these experiments.[12]

The focus of this thesis is on the photodissociation dynamics of alkali halides. Among all of the reaction systems studied so far by the FTS technique, alkali halides present a particularly interesting and rewarding case. As these heteronuclear diatomics are the simplest systems for studying the nonadiabatic charge-transfer processes, they have attracted many researchers since the early part of this century. Thus, there exists a wealth of literature describing both the spectroscopy and dynamics of alkali halides that provides a reference frame against which the achievements of the current time resolved work can be measured. Chapter 2 of this thesis reviews the spectroscopy and dynamics of alkali halides, as well as presents the theoretical framework needed in subsequent chapters for understanding the curve-crossing phenomenon in alkali halides. Chapter 3 describes the experimental methodology of FTS as applied to the photodissociation of alkali halides and some new developments in understanding the essential features of these FTS experiments. In the following chapter, a new procedure is presented for inverting the FTS data to the PES's of the dissociation reaction; these PES's are then employed in quantum dynamical simulations of the FTS experiments to test the validity of the inversion method. In the final chapter, the dynamics of the wave-packet evolution after many oscillations are discussed, including a complete account of the experimental results and various theoretical models that have been developed in an attempt to explain the somewhat unexpected experimental findings.

References:

1. R. D. Levine and R. B. Bernstein, *Molecular Reaction Dynamics*, 2nd ed., Oxford University Press, New York (1987).

2. D. Herschbach, *Angew. Chem. Int. Ed.* **26**, 1221 (1987).

3. Y. T. Lee, *Angew. Chem. Int. Ed.* **26**, 936 (1987).

4. J. C. Polanyi, *Angew. Chem. Int. Ed.* **26**, 1221 (1987).

5. R. N. Zare, D. R. Herschbach, *Proc. IEEE* **51**, 173 (1963).

6. (a) S. J. Riley and K. R. Wilson, *Farad. Disc. Chem. Soc.*, 53, 132 (1972);

   (b) G. E. Busch and K. R. Wilson, *J. Chem. Phys.* 56, 3626 (1972).

7. M. J. Dzvonik, S. Yang, and R. Bersohn, *J. Chem. Phys.* 61, 4408 (1974).

8. D. Imre, J. L. Kinsey, A. Sinha, and J. Krenos, *J. Phys. Chem.* **88**, 3956 (1984).

9. P. R. Brooks, R. F. Curl, and T. C. Maguire, *Ber. Bunsenges. Phys. Chem.* **86**, 401 (1982); P. R. Brooks, *Chem. Rev.* **88**, 407 (1988).

10. R. B. Metz, T. Kitsopoulos, A. Weaver, and D. M. Neumark, *J. Chem. Phys.* **88**, 1463 (1988).

11. (a) R. L. Fork, B. I. Greene, and C. V. Shank, *Appl. Phys. Letters*, **38**, 671 (1981);

    (b) For a recent comprehensive review of the technology for generating and amplifying ultrashort (picosecond or shorter) laser pulses, see: J. D. Simon, *Rev. Sci. Instrum.* **60**, 3597 (1989).

12. For recent reviews of the research interests of Zewail's group, please see: L. R. Khundkar and A. H. Zewail, *Ann. Rev. Phys. Chem.* **41**, 15 (1990); M. Gruebele and A. H. Zewail, *Phys. Today* **43**, No. 5, 24 (1990); A. H. Zewail, *Science* **242**, 1645 (1988); A. H. Zewail and R. B. Bernstein, *Chem. Eng. News*, **66**, 24 (1988).

The breadth and depth of the research activities of Zewail's group are also represented by the titles of recent Ph.D.theses:

P. M. Felker, "*Picosecond Dynamics of Intramolecular Vibrational Energy Redistribution (IVR) in Jet Cooled Molecules,*" Caltech (1985);

L. R. Khundkar, "*Microcanonical Rates of Unimolecular Reactions Studied by Time-resolved Photofragment Spectroscopy,*" Caltech (1988);

N. F. Scherer, "*Time-resolved Studies of Molecular Reaction Dynamics and Development of Experimental Methodology,*" Caltech (1989);

J. S. Baskin, "*Real-time Observation and Analysis of Coherence and Alignment in Molecular Systems: Isolated Molecules and Chemical Reactions,*" Caltech (1990);

D. H. Semmes, "*Picosecond Studies of the Vibrational Predissociation of van der Waals complexes,*" Caltech (1990);

L. W. Peng, "*Reactions in Small Clusters studied by Time-resolved Laser Spectroscopy,*" Caltech (1991);

M. Dantus, "*Femtosecond Transition-state Spectroscopy of Chemical Reactions,*" Caltech (1991).

13. N .F. Scherer, J. L. Knee, D. Smith, and A. H. Zewail, *J. Phys. Chem.* **89**, 5141 (1985).

14. M. Dantus, M. J. Rosker, and A. H. Zewail, *J. Chem. Phys.* **87**, 2395 (1987).

15. M. J. Rosker, M. Dantus, and A. H. Zewail, *J. Chem. Phys.* **89**, 6113 (1988).

16. M. Dantus, M. S. Rosker, and A. H. Zewail, *J. Chem. Phys.* **89**, 6128 (1988).

17. R. B. Bernstein and A. H. Zewail, *J. Chem. Phys.* **90**, 829 (1989).

18. T. S. Rose, M. S. Rosker, and A. H. Zewail, *J. Chem. Phys.* **91**, 7415 (1989).

19. R. M. Bowman, M. Dantus, M. Gruebele, and A. H. Zewail, *J. Chem. Phys.* **91**, 7447 (1989).

20. R. M. Bowman, J. Gerdy, G. Roberts, and A. H. Zewail, *J. Phys. Chem.* in press.

21. J. C. Williamson and A. H. Zewail, *Proc. Nat. Acad. Sci.* **88**, 5021 (1991);

J. M. Thomas, *Nature* **351**, 694 (1991).

Figures

Captions:

Figure 1.1

The schematics of the femtosecond transition-state spectroscopy as applied to a set of idealized PES's of a diatomic molecule. At time $t = 0$, a femtosecond pump pulse with a wavelength of λ_1 prepares a coherent vibrational wave packet on the excited state (V_1) from the ground state (V_0), as indicated by the vertical transition to V_1. The average internuclear separation increases as the wave packet evolves on this repulsive potential. At $t = \tau$, another femtosecond pulse of wavelength λ_2^* (or λ_2^∞) promotes the somewhat dispersed wave packet from V_1 to a higher PES, V_2. The signal detected in FTS experiments originates from the fluorescence emitted from this potential.

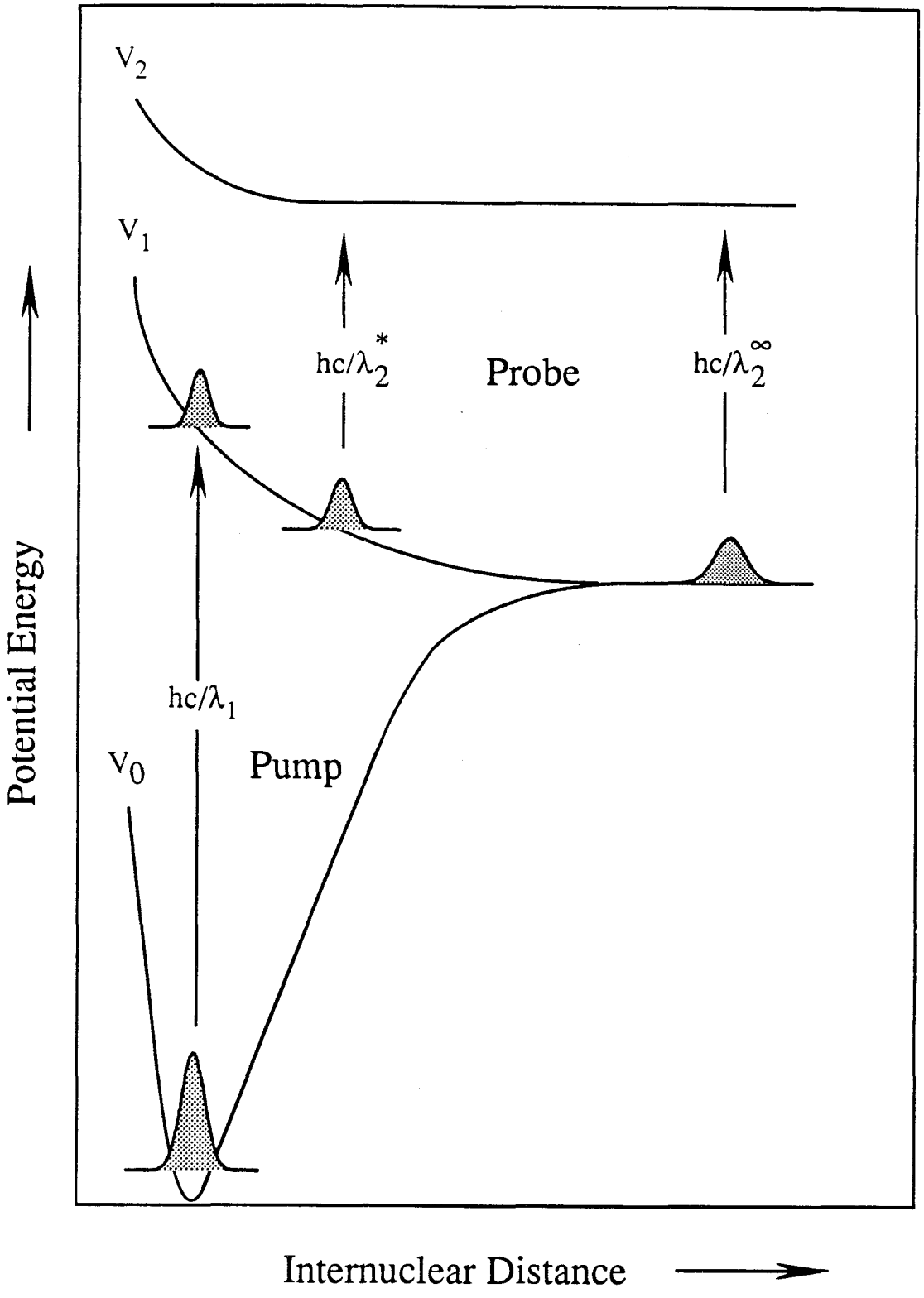
V2
V1
V0
hc/λ2*
Probe
hc/λ2∞
hc/λ1
Pump
Potential Energy
Internuclear Distance

Figure 1.1

Chapter 2

An Overview of Photodissociation of Alkali Halide Molecules

I. Introduction: a Historical Perspective

The field of photodissociation of alkali halide molecules is almost as old as modern physical chemistry. The first reported optical study of an alkali halide dates back to 1914, when McLennan observed the emission spectrum of KI,[1] just about the same time as Bohr's old quantum theory was formulated.[2] In the late 1920's, more work was reported by various authors. Most of these studies utilized the atomic fluorescence technique to determine the dissociation energies of alkali halides, e.g., NaI, CsI.

One particularly important contribution to the spectroscopy of alkali halides during this period was the work by James Franck, on a series of alkali halides spectra at the Zweites Physikalisches Institut at Göttingen.[3] Franck and co-workers were the first to consider the possibility that the photodissociation of an alkali halide might leave the two atoms in their ground states, and thereby established the absorption spectrum technique as a viable way to deduct the dissociation energy of alkali halides. At the same time, they also attracted attention to the curve-crossing problem in alkali halides, in which the energy of the separated neutral atoms lies below that of the separated ionic pair, while at the equilibrium configuration of their ground electronic states the order is reversed.

An interesting side note with some historical signifance is that Franck published a paper in 1926 titled "Elementary Processes of Photochemical Reactions" in the *Transactions of the Faraday Society*,[4] in which he stated "We may assume that when light is absorbed the nuclei can only alter their *potential* energy, as the raising of the electron system to another quantum state alters the strength of the chemical binding of the molecule." This idea later came to be known as the Franck-Condon principle of vertical transitions in molecular spectroscopy.[5] One manifestation of the vertical transition principle was presented in the experiments by Hogness and Franck on the photodissociation of NaI.[6] They observed that the linewidth of Na D line emission was

much broader than the Doppler linewidth dictated by the temperature, which implied that the photodissociated products carried very high kinetic energies with them; when they tuned the photodissociation UV light source to shorter wavelengths, the width became even broader. As will be seen in later parts of this thesis, the same qualitative principle still applies to the understanding of today's femtosecond time-resolved photodissociation experiments.

In the early 1930's, the studies of alkali halide spectroscopy were advanced to a new level, as represented in the doctoral thesis of H. Levi.[7] In her thesis, an extensive study of the fluctuation bands of several alkali halides was made by a combination of absorption and emission spectra. Dissociation energies were determined fairly accurately for a number of alkali halides, in good agreement with currently accepted values. This is quite a remarkable feat, given the degree of sophistication of instruments in the 1930's. Attempts were also made to invert the spectra to both the ground and excited electronic-state potentials in Levi's thesis.

Since then, the field has progressed steadily, with the advances in quantum chemistry, the introduction of molecular beam techniques to chemistry, the invention of lasers and the subsequent birth of the field of laser spectroscopy. As a matter of fact, alkali halides played a crucial role in the "*early alkali age*" of molecular-beam chemistry.[8] In the 1920's, Michael Polanyi showed that many alkali reactions proceed at rates corresponding to "reaction at every collision" in a series of classic studies. This extraordinarily large reaction probability was ascribed to a charge transfer mechanism, the "harpooning" mechanism as called by M. Polanyi: When an alkali atom flies by another halogen-containing molecule, the S electron in the outermost shell will jump over to the halogen atom, and then with the aid of the Coulomb attraction, the alkali ion will pull the halogen atom over from the negatively charged molecule to form an alkali halide molecule. Because of the large reaction probability and the relative ease of detecting alkali halides and alkali

atoms by surface ionization techniques, the $M + RX \rightarrow M^+X^- + R$ reactions, where M, R, and X are alkali, alkyl, and halogen groups, respectively, were the first group of elementary chemical reactions studied by crossed-molecular-beam techniques.

A comprehensive review of the optical spectroscopy of alkali halide molecules was given by Berry,[9] which covered all the major developments in this field through 1977. Since 1978, the field of photodissociation of alkali halides has experienced such tremendous progress that some long-standing questions have finally been answered. Among the remarkable experiments done in the last decade, Tiemann and his co-workers applied LIF techniques to obtain the partially bound state A 0^+ spectra of NaI and LiI;[10] van Veen *et al.* measured the relative ratio of the parallel vs. perpendicular transition strength of several alkali halides in the near-ultraviolet region;[11] J. C. Polanyi's group at University of Toronto performed LIF experiments on KI and NaI and characterized a previously unknown upper bound state.[12] Most recently, the femtosecond transition state spectroscopy techniques developed by Zewail and his coworkers have been applied to examine the photodissociation processes in NaI.[13] This study clearly demonstrates the behavior of a wave packet propagating in a partially leaking potential well formed by the avoided crossing of the attractive Coulombic curve and the repulsive covalent curve.

This chapter will focus on recent advances in the field of optical spectroscopy and photodissociation reaction dynamics of alkali halides and will present a summary of the current status. The remainder of this chapter is structured as follows: In part II, a brief review of the origin of the curve-crossing problem is given; construction of the molecular states from atomic bases and the curve-crossing mechanism will be discussed. In the following section, a general quantum-mechanical treatment of the curve-crossing problem is outlined. The representation theory, the Landau-Zener curve-crossing model,[14-17] and the semiclassical theory of curve crossing will also be discussed.[18] In part IV, recent spectroscopic results are presented and discussed in detail; special emphasis is put on the

inversion of spectroscopic data to potential-energy curves, and comparison of potential curves from different theories and experiments.

II. The Origin of the Curve-Crossing Problem in Alkali Halides

The alkali halide molecules provide the ideal testing case for understanding the curve-crossing problem. The ionic ground states of these molecules are all $X\ ^1\Sigma^+$, because both the alkali and halogen ions are close-shelled, there is no electronic and spin angular momentum. The dissociation limit corresponding to the metal ion and the halide ion, $M^+ (^1S) + X^- (^1S)$, differs in energy from that of the atoms $M^0 (^2S_{1/2}) + X^0 (^2P_{3/2})$ by the amount Q, which is equal to the difference between the ionization potential (IP) of the metal M and the electron affinity (EA) of the halogen X; Q = IP(M) - EA(X) (see Table 2.1). Because all ionization potentials of alkali atoms are greater than any electron affinity of a halogen atom, Q is always positive, and the dissociation limit of lowest energy is always the atomic limit, for all alkali halides. (See Figure 2.1 for a typical potential diagram of an alkali halide molecule.)

The combination of $^2S_{1/2}$ and $^2P_{3/2}$ gives rise to eight *covalent* molecular states; *i.e.*, (2 x 1/2 + 1) x (2 x 3/2 + 1) = 8, with the overall angular momentum quantum number ranging from 2 to 0 and term symbols from Δ to Σ. Compared with the strongly bound ionic ground state, none of the covalent states is found to be bound; except for a shallow van der Waals well, no potential wells deeper than a few hundred wavenumbers have been observed for these states. Among all the covalent states, one must be a $^1\Sigma^+$ (Hund's case (a)) or a 0^+ state (Hund's case (c)), which has the same symmetry as the ground ionic state. Hence, all alkali halide molecules possess at least one crossing of the two states, the ionic ground state and excited covalent state, which have the same symmetry (see Table 2.2 for the crossing distances). In fact, except for CsI, the M ($^2S_{1/2}$) and X ($^2P_{1/2}$) atomic asymptotic limit is also lower than M^+ and X^-; thus, all alkali halides except CsI have at

least two crossings with the ionic curve.

When an alkali halide molecule is promoted to the lowest covalent state by light , one might picture the subsequent behavior of the molecule as follows: Absorption of a photon carried the system vertically from the ground state to the repulsive branch of the 0^+ state* and produced a change in the electronic wavefunction, which amounts to an electron being transferred from the halogen atom to the metal atom along the internuclear axis. The nuclei move apart across the relatively flat region of the potential curve toward the crossing point R_X. Just as the crossing region is reached, the electronic wavefunction readjusts itself, and an electron jumps back from the metal to the halogen to form an ionic pair. Static electric force between the two oppositely charged ions pulls the nuclei back toward each other. As the nuclei pass the crossing region again, the electron returns to the metal, and the two particles, now neutral, come together once more. This picture holds under the adiabatic hypothesis; that is to say, the electrons move fast enough compared to the heavy nuclei to behave by themselves as a closed system with the internuclear distance as a parameter. Thus, the electronic motion is separable from that of the nuclei and the electronic charge cloud is described at any internuclear distance by an eigenfunction of the electronic Hamiltonian. If the alkali halide molecules do satisfy this hypothesis in their first covalent state 0^+, then this description must be correct for the motion of the electrons during a single vibration. One may, however, question the validity of the hypothsis on the following qualititive argument: Electronic velocities are roughly $1800^{1/2}$, or about 40 times faster than the nuclear velocities. Therefore, in the time that the nuclei move 0.1 Å, the electrons can move about 4 Å. Hence, if the crossing region occurs at a seperation of 10

---

* To simplify the discussion without losing generality, the upper state is assumed to be described by Hund's case (c) coupling. If the upper state is Hund's case (a) coupled, the 0^+ state should be replaced by $^1\Sigma^+$.

Å, and is 0.1 Å wide, an electron cannot be expected to make a successful jump over 10 Å from one nucleus to the other; *it simply does not have enough time*. As a result, the electronic charge cannot be described by the eigenfunctions of the electronic Hamiltonian alone, and its motion cannot be separated from that of nuclei. Under this circumstance, the Born-Oppenheimer approximation breaks down, and the alkali halide molecule behaves diabatically.

From the above discussion, we can conclude that whether an alkali halide behaves adiabatically or diabatically depends critically on the radial crossing distance, the width of the coupling region, and the velocity of the nuclear motion at the crossing point. The crossing distance and the coupling-region width are determined by the nature of the electronic and nuclear wavefunctions involved, while the crossing velocity can be controlled to some degree by changing the excitation wavelength. This point will be further illustrated in later chapters on the FTS of alkali halides. If at the crossing point R_x the internuclear separation is too large and the nuclei move too fast over a narrow coupling region, the electron will not be able to jump over a long distance, so it will remain with one nucleus. On the other hand, if the distance is not too great and the velocity of the nuclei not too fast, then an electron transfer will occur at the crossing point; thus, the molecule behaves in the adiabatic limit. Alkali halide molecules have a range of crossing distances and coupling widths; thus, they provide various cases to study the curve-crossing phenomenon, from the diabatic limit to the adiabatic limit. However, before we proceed to discuss the spectroscopic manifestations of the curve crossing in alkali halides, we will first consider a general quantum mechanical treatment of the curve-crossing problem in the next section.

III. A Quantum Mechanical Treatment of the Curve-Crossing Problem

III.1 Formal Solution of the Coupling Problem

In a molecular system with nuclear spin, spin-orbit and other relativistic terms omitted, the total Hamiltonian can be expressed as follows:

$$H = T_N(R) + T_e(r) + V(r, R), \tag{2.1}$$

where $T_N(R)$ is the nuclear kinetic-energy operator while $T_e(r)$ is the electronic kinetic-energy operator. $V(r, R)$ represents the Coulomb attraction and repulsion terms among all the nuclei and electrons. Under normal conditions, since the electrons move so fast compared to the heavy nuclei because of the huge mass difference, their motion is practically decoupled from the nuclear motion (Born-Oppenheimer Approximation). On the basis of this argument, we can define the electronic Hamiltonian as the full Hamiltonian minus the nuclear kinetic-energy term:

$$H_{el} \equiv H - T_N(R) = T_e(r) + V(r, R). \tag{2.2}$$

Solving the Schoedinger equation for the electronic part only, we will have

$$H_{el}\psi^{el}(r,R) = V(R)\psi^{el}(r,R), \tag{2.3}$$

where the eigenvalue $V(R)$ and eigenfunction $\psi_{el}(r, R)$ depend only parametrically on the internuclear coordinate R. The nuclear part of the Schödinger equation is

$$H_N \equiv T_N(R) + V(R), \tag{2.4}$$

$$H_N\psi^N(R) = E\psi^N(R), \tag{2.5}$$

where E is the total energy of the system. The overall wavefunction of the molecular system can be expressed as a product of the electronic and nuclear eigenfunctions. The above equations reflect that the electrons move in a closed system by themselves with the internuclear distances as a set of parameters, or equivalently, the nuclei move in a potential determined by the wavefunction of the electrons. If the electronic wavefunction supports a

minimum in the potential, the nuclear motion will be quantized when the total energy of the nuclear motion is less than the asymptotic value of the electronic potential and the discrete states are the molecular vibrational states in that particular electronic state. If the electronic wavefunction does not support a potential well, the nuclear wavefunctions will be unbound and the energy spectrum of the nuclear motion will be continuous. In most cases, since the electronic wavefunction only depends weakly on the internuclear separation, the first derivative of the wavefunction relative to the internuclear distance will be negligible, which implying that the character of the electronic wavefunction does not vary much with the internuclear distance. However, this ideal picture breaks down when two electronic surfaces V_1 and V_2 with the same symmetry cross at certain point R_x. (see Figure 2.2). At this point,

$$V_1(R_x) = V_2(R_x), \tag{2.6}$$

$$<\psi_1^{el}(r,R_x)/H/\psi_2^{el}(r,R_x)> \equiv V_{12}(R_x) \neq 0. \tag{2.7}$$

Equation (7) comes about because $\psi_1^{el}(r,R_c)$ and $\psi_2^{el}(r,R_c)$ have the same symmetry; thus, the matrix element $<\psi_1^{el}(r,R_c)/H/\psi_2^{el}(r,R_c)>$ is non-vanishing. As a result, these two states are coupled. The Hamiltonian for such a coupled two-state problem can be expressed as a 2 by 2 matrix:

$$\begin{pmatrix} H_1 & H_{12} \\ H_{21} & H_2 \end{pmatrix}.$$

In the diabatic representation, where the electronic wavefunctions are smooth functions of the nuclear separation R (*i.e.*, $\frac{d\psi}{dR}$ is negligible.), the matrix is not diagonal. The two states are coupled by the off-diagonal potential terms. In the adiabatic presentation, where the electronic wavefunctions are eigenfunctions of the Hamiltonian, the matrix is diagonal;

however, the electronic wavefunctions are no longer smooth functions of R; they change character drastically around R_x. As a result, these two states will be coupled by the nuclear kinetic-energy operators. These two representations are equivalent and can be converted to each other by a unitary transformation:

$$\begin{pmatrix} H_+ & 0 \\ 0 & H_- \end{pmatrix} = \begin{pmatrix} cos\theta & -sin\theta \\ sin\theta & cos\theta \end{pmatrix} \begin{pmatrix} H_1 & H_{12} \\ H_{21} & H_2 \end{pmatrix} \begin{pmatrix} cos\theta & sin\theta \\ -sin\theta & cos\theta \end{pmatrix}, \tag{2.8}$$

where $tan2\theta(R) = 2V_{12}(R)/(V_2(R) - V_1(R))$. Similarly, the basis sets for these two different representations: (ψ_1, ψ_2) for the diabatic presentation and (ψ_+, ψ_-) for the adiabatic presentation, are related by the following equation:

$$\begin{pmatrix} \psi_+ \\ \psi_- \end{pmatrix} = \begin{pmatrix} cos\theta & sin\theta \\ -sin\theta & cos\theta \end{pmatrix} \begin{pmatrix} \psi_1 \\ \psi_2 \end{pmatrix}. \tag{2.9}$$

It is quite instructive to inspect the qualitative behavior of the last equation. When R is at the far left side of R_x and therefore $V2 \gg V1$, $tan2\theta(R) \rightarrow +0$ and $\theta(R) = 0$. Equation (9) goes to:

$$\begin{pmatrix} \psi_+ \\ \psi_- \end{pmatrix} = \begin{pmatrix} 1 & 0 \\ 0 & 1 \end{pmatrix} \begin{pmatrix} \psi_1 \\ \psi_2 \end{pmatrix}. \tag{2.9'}$$

When R is at the other side of R_x, $tan2\theta(R) \rightarrow -0$ and $\theta(R) = \pi/2$. then we have:

$$\begin{pmatrix} \psi_+ \\ \psi_- \end{pmatrix} = \begin{pmatrix} 0 & 1 \\ -1 & 0 \end{pmatrix} \begin{pmatrix} \psi_1 \\ \psi_2 \end{pmatrix}. \tag{2.9''}$$

If $R = R_x$, $tan2\theta(R) = \infty$ and $\theta(R) = \pi/4$. the eigenstates are mixed equally:

$$\begin{pmatrix} \psi_+ \\ \psi_- \end{pmatrix} = \begin{pmatrix} \frac{\sqrt{2}}{2} & \frac{\sqrt{2}}{2} \\ -\frac{\sqrt{2}}{2} & \frac{\sqrt{2}}{2} \end{pmatrix} \begin{pmatrix} \psi_1 \\ \psi_2 \end{pmatrix}. \tag{2.9'''}$$

Although these two representations are theoretically equivalent, often one presentation is the optimal choice for a particular problem at hand. For alkali halide systems explored in this thesis, the diabatic representation is chosen because the coupling term is explicitly expressed as the coupling between potentials. In the diabatic representation, the transition probability from one diabatic surface to the other can be written as follows, under perturbation approximation:

$$P_{12}(E) = <\psi_1^{el}(r,R_c)\psi_1^N(R)/H/\psi_2^{el}(r,R_c)\psi_2^N>, \qquad (2.10)$$

where E is the total energy of the system. There are numerous ways to solve equation (10). The semiclassical method of Landau[14] and Zener[15] is considered in the next section, followed by Child's semiclassical theory of predissociation.[18]

III.2 The Landau-Zener Curve-Crossing Probability

In the early 1930's, Landau[14] and Zener[15] independently treated the curve-crossing problem. The common assumption they made was that the coupling-matrix element was a constant and that the difference between two diabatic curves is linear:

$$V_{12} = V_{21} = Constant, \qquad (2.11)$$

$$V_1(R) - V_2(R) = -(F_1 - F_2)(R-R_x), \qquad (2.12)$$

where F_1 and F_2 are the derivatives of V_1 and V_2 at R_x, respectively. Landau applied a time-independent method to solve this problem and obtained two expressions for the weak coupling limit and the strong coupling limit, respectively. Zener employed a time-dependent perturbation theory and derived a general solution that would be valid at any coupling strength and would also agree with Landau's expressions at two extreme cases:

$$P_{12} = exp(-4\pi^2 V_{12}^2/h\nu/F_1-F_2/), \qquad (2.13)$$

where P_{12} is the probability for the system to make a transition from one adiabatic state to the other or to remain on the same diabatic state. In both derivations semiclassical (JWKB) approximations were invoked for the wavefunctions. Derivation of Equation (2.13) is mathematically not trivial. Fortunately, it can be found in a number of standard textbooks.[16,17] There are two parameters in (13) that are worth special attention. One is the coupling matrix element: The bigger this matrix element is, the smaller P_{12} will be. Therefore, V_{12} is a measure of the adiabacity of the system. The other important parameter is the velocity v at the crossing point; P_{12} increases as velocity v increases. This is intuitively obvious because the faster the nuclei move, the more the system will behave diabatically. If the nuclei move infinitely slowly, the electrons will always have enough time to adjust themselves, so as to make the system behave adiabatically.

While velocity of the nuclei can be controlled by external excitation, the coupling matrix element is intrinsic to the system; it is determined by the interaction between the two diabatic electronic wavefunctions. Thus, the determination of the coupling-matrix elements is of utmost importance to the understanding of the curve-crossing behavior of alkali halides. Grice and Herschbach[19] calculated the coupling matrix element for H_2 and a number of alkali hydrides as well as alkali halides using an approximation method based on asymptotic wavefunctions. Even though this method may be primitive compared to today's sophisticated quantum chemical computational techniques developed for powerful computers, the results of this simple calculation are quite accurate and have stood the test of time over the last twenty years. In fact, the Grice-Herschbach coupling-matrix element for NaI seems to be closer to experimentally determined values than the results from most recent *ab initio* calculations for the same molecule.[20] The reason for the remarkable success of the simple approximation for alkali halides relied on the judicious choice of the asymptotic wavefunctions and on the fact that the crossing distance in alkali halides is so large that the asymptotic wavefunction is very close to the exact wavefunction.

III.3 The Semiclassical Theory of Predissociation Caused by Curve-Crossing

In the late 1960's and early 1970's, Child and his co-workers developed a semiclassical theory of predissociation caused by curve crossing with arbitrary coupling strengths.[18] The derivation was based on applying curve-crossing connection formulas to JWKB wavefunctions (see Figure 2.3.). The goal of this theory was to calculate the absorption spectral lineshape with a mixed representation: the adiabatic *bound* upper state (V_+) and the diabatic *bound* lower state (V_2). The center of the spectral lineshape reflects the shift from the adiabatic (or the diabatic) eigenstate, and the linewidth is directly related to the lifetime of the predissociating level.

The main results can be summarized in the following equations,

$$A_+^2 = \frac{(1+u)\cos^2\theta_2}{\cos^2\theta_2 + 2u\cos(\theta_+ - \theta_2)\cos\theta_+\cos\theta_2 + u^2\cos^2\theta_+}, \tag{2.14}$$

$$u = \exp(2\pi\upsilon) - 1, \tag{2.15}$$

$$\upsilon = 2\pi V_{12}^2/h\nu/|F_1 - F_2|, \tag{2.16}$$

where A_+ is amplitude of the semiclassical wavefunction at the classical inner-turning point. The quantity A_+^2 represents the spectroscopic line shape, u is the coupling strength and υ is the Landau-Zener switching parameter. q_+ and q_2 are closely related to the complete phase integrals for the upper adiabatic (V_+) and diabatic (V_2) curves, respectively. They are

$$\theta_+ = \alpha_+ + \beta_+ + \chi, \tag{2.17}$$

$$\theta_2 = \alpha_- + \beta_+, \tag{2.18}$$

where $\alpha_\pm$ and β_+ are phase integrals evaluated on the upper and lower adiabatic curves:

$$\alpha_{\pm} = \int_{\alpha_{\pm}}^{r_x} k_{\pm}(r)dr, \tag{2.19a}$$

$$\beta_{+} = \int_{r_x}^{\beta_{+}} k_{+}(r)dr, \tag{2.19b}$$

k is the momentum vector and χ is a phase–correction factor caused by the avoided crossing:

$$\chi = arg\ \Gamma(i\upsilon) - \upsilon\ ln\ \upsilon + \upsilon + \pi/4. \tag{2.20}$$

Approximate equations for the positions E' and width Γ of predissociating states can be developed by noting that the denominator of Eq. (2.14) vanishes identically if by chance at a single energy E, where it supports bound levels for both adiabatic upper state and diabatic lower state. This condition gives rise to a sharp level at E' as manifested by the fact that Eq. (2.13) is reduced to a Lorentzian line shape

$$A_{+}^{2} = \left[\frac{h\upsilon}{1+\chi}\right] \frac{\Gamma/2\pi}{(E-E')^2 + \Gamma^2/4}\ , \tag{2.21}$$

where

$$E' = (E_2 + \chi E+)/(1 + \chi), \tag{2.22}$$

$$\Gamma = 2\pi\chi(\gamma + \chi)(E_2 - E_+)^2/h\upsilon(1+\chi)^3, \tag{2.23}$$

$$\gamma = \upsilon_2/\upsilon_+, \tag{2.24}$$

$$\chi = u\gamma. \tag{2.25}$$

An approximate and intuitive picture emerges from these equations. The diabatic and adiabatic wells each support hypothetical bound levels characterized by vibrational quantum number υ_+ and υ_2 and the common rotational quantum number J. If the energies

of these levels are plotted as a function of $J(J+1)$, two series of approximately linear curves result. The position and linewidth of a predissociating level depend on the two nearby energies E_2 and E_+, the coupling parameter u, and the frequency ratio γ. When the curves for E_2 and E_+ are close, meaning that the final energy level is bound in both wells, thus the lineshape will be sharp; on the other hand, when they are farther apart, the resonance is broad. This simple picture will prove to be very valuable in understanding the real time dynamics of the photodissociation of NaI.

IV. Spectroscopy and Potential-Energy Curves of Alkali Halides

IV.1 Summary of Recent Experimental Results

Recently, there have been a number of experiments that contributed a great deal toward a better understanding of the electronic structure and photodissociation dynamics of alkali halides. These works will be summarized in the following categories: molecular beam scattering and chemi-ionization, chemiluminescence, photofragmentation, and laser induced fluorescence (LIF).

Molecular-Beam Scattering and Chemi-ionization

In the late 1950's, molecular-beam scattering techniques were introduced for the studies of elementary chemical reactions.[8] The essence of these kinds of experiments is to prepare one (or both) of the reactants in a collision-free molecular beam, sending it through a reaction vessel containing the other reactant (or crossing two reactant beams), and then to detect the product angular distributions and deduce the differential-reaction cross sections.

In the early 1970's, Delvigne and Los performed a series of experiments on alkali halogen molecules or atoms with a combination of molecular-beam scattering and chemi-ionization techniques.[21] In particular, they measured the relative differential cross sections for the collision process: $Na + I \rightarrow Na^+ + I^-$ at kinetic energies from 13 to 85 eV. Their

measurements allowed estimations of the covalent potential parameters as well as the first experimental measurement of the coupling-matrix element(~ 0.05 eV). In order to account for the dicrepancy between experimental data and calculated values at large impact parameters, they invoked a Landau-Zener-like "rotational coupling" mechanism; the discrepancy could be partially removed. Limited by the experimental resolution (about 0.5 eV) and a distribution of the angular momentum quantum number ($\Omega = 0^{\pm}$, 1, 1, 2), the potential parameters could not be determined very accurately.

Kinsey's group at MIT performed similar experiments on the elastic scattering of potassium atoms by atomic iodine at thermal energies (0.08 - 0.20 eV).[22a] Attempts were made to synthesize the scattering data from assumed potential curves. One noteworthy conclusion from this study was that the welldepth of the 0^+ state cannot be more than 150 cm^{-1} for KI.

Chemiluminescence

In addition to their molecular beam scattering experiments on the KI system, Kinsey 's group also measured the chemiluminescence spectra of potassium iodide in a dilute diffusion flame.[22b] From the analysis of the fluctuation bands and the molecular-beam data, they were able to determine accurately the excited-state potential for potassium iodide.

More recently, laser-induced emission spectra of KI and NaI were recorded by Polanyi's group in an effusive molecular-beam machine. From these studies, they were able to characterize the potential curves of a previously unknown bound excited state, which led to the dissociation of KI and NaI to excited alkali atoms (^2P_J, J = 1/2, 3/2) and ground-state iodine atom ($^2P_{3/2}$).

Photofragmentation

Photofragmentation techniques were pioneered by Wilson and co-workers at UCSD[23] and further developed by Bersohn and his co-workers at Columbia[24] among many others. In a photofragmentation experiment, one measures the velocity and spatial distributions of the photofragments induced by a polarized laser beam. The velocity distribution of the photofragments depends on the energetics of the parent molecule, while the angular distribution reflects the symmetry nature of the electronic-excitation process and the lifetime of the dissociative complex.

Anderson *et al.* were the first to carry out photofragmentation experiments on alkali halides.[25] They photodissociated NaI at a fixed laser wavelength, namely, the second harmonic of a Ruby laser, 347.1 nm. They measured the spatial distribution of the products and determined the relative ratio of the parallel transition vs. perpendicular transition. Su and Riley[26] extended this work to all the alkali iodides and bromides at 266 nm. From the measurement of product time-of-flight and spatial distribution, these workers were able to determine the symmetries of the electronic transitions at 266 nm and the dissociation energies of all the alkali iodides and bromides.

In these photofragmentation experiments, the uncertainty about the lifetimes of the dissociating molecules hindered the interpretation of the experimental data. The most important parameter that can be extracted from the experimental data is the anisotropy parameter β. This parameter can be affected by the lifetime of the dissociating molecule. If the lifetime is short compared with the rotational period, then contributions of the parallel and perpendicular transitions to the spatial anisotropy parameter are 1 and -0.5, respectively. However, if the lifetime is much longer than the rotational period, the spatial anisotropy will be totally washed out; the anisotropy parameter will be 0.25 for both the parallel and perpendicular transitions. It is usually assumed that the 1 state dissociates promptly, while the 0^+ state may be a predissociating state; therefore, it may have a long

lifetime. It has be shown by Delvigne *et al.* that the 1 state may be coupled to the 0^+ state through rotational coupling; therefore, the 1 state may not dissociate promptly. One can argue, however, that this effect is important only for large impact parameters, and therefore, for rotationally highly excited molecules, which may be rare at normal temperatures. For the 0^+ state, however, the problem is more severe. There is a distribution of lifetimes for a predissociating molecule ranging from subpicoseconds to nanoseconds. From the experimental data, only lower (short lived) and upper (long lived) bounds can be given for the ratio between parallel and perpendicular transitions.

van Veen *et al.* further extended the photofragmentation experiment for KBr, KI, NaBr, and NaI by using a frequency-doubled tunable dye laser as the excitation laser. They not only measured the dissociation energies and the relative transition strength of the parallel and perpendicular transitions, but also constructed the repulsive branches of the 0^+ and 1 potential curves by application of the Franck-Condon principle. However, there was the same problem about the lifetime ambiguities.

Laser-Induced Fluorescence

Using high-resolution absorption and LIF techniques, fragmentary rotational fine structures were observed in the electronic transition $0^+ \leftarrow X\ ^1\Sigma^+$ of NaI and LiI by Tiemann and his co-workers.[10] The assignment was obtained with the help of Child's semiclassical theory. From this kind of assignment, RKR potentials for both the ground $X\ ^1\Sigma^+$ and the excited 0^+ states were obtained for the first time. The coupling-matrix element was deduced to be 0.054 eV (434 cm^{-1}). It is puzzling to note that the repulsive branch of the 0^+ potential of NaI could not reproduce the known Franck-Condon factors and did not agree with van Veen's photofragmentation work.

Ragone *et al.*[27] performed the only known supersonic molecular-beam-LIF work on NaI, but their interpretation was called into question by Schaefer *et al.* and has been a

topic of recent debate in the literature.[28a&b] Levy and Berry[28b] seem to agree with Tiemann and co-workers assignments,[28a,10] however, a re-analysis of the supersonic beam spectra has not appeared in the literature.

IV.2 Construction of the Potential-Energy Curves and Comparisons of Different Experiments

It has long been recognized that the ground state of an alkali halide molecule is mainly ionic in character. However, the measured dipole moment is generally smaller than would have been predicted by a totally ionic model: two oppositely charged particles separated by the equilibrium bond length. To remedy this simple point-charge picture, Rittner[29] proposed a model to describe the interaction between the alkali cation and the halogen anion: the ions are polarizable spheres; besides the Coulomb attraction, there are also charge-induced-dipole, dipole-dipole, charge-induced-dipole attractions, along with the usual van der Waals dispersive attraction. The following potential was suggested for the ground state of alkali halide molecules:

$$v(R) = Aexp(-R/\rho) - e^2/R - e^2(\alpha_{M^+}+\alpha_{X^-})/2R^4 - C_{MX}/R^6 - 2e^2\alpha_{M^+}\alpha_{X^-}/R^7. \quad (2.26)$$

The α's are the ionic polarizabilities (M^+ and $X^-$are alkali and halogen ions, respectively). The R^{-1}, R^{-4} and R^{-7} , and R^{-6} terms represent Coulomb, ion-induced dipole, and van der Waals interactions, respectively. The exponential term was included to describe the short-range repulsion; parameters A and ρ are obtained by fitting the equilibrium internuclear distance and vibrational spacing. This model was later known as the Rittner model and it was quite successful in predicting the binding energy and dipole moment, even vibrational anharmonicity to certain degree, given the available experimental data at the time.

Brumer and Karplus[30] re-examined this problem on the bases of a quantum-mechanical-exchange perturbation theory. They found that the dependence of the induced dipoles on internuclear distances made it appropriate to drop the R^{-6} and R^{-7} terms in the

original Rittner potential. A new set of parameters was given that agreed better overall with experimental data. This was called the truncated Rittner potential or T-Rittner potential. Despite its apparent success, it has not been universally adopted in the literature.

Faist and Levine have also suggested a slight modification to this Rittner potential in their paper on the chemi-ionization cross section of Na and I so that the potential would be well behaved at small R through the inclusion of an additional repulsive term with R^{-8} dependence as a cofactor before the exponential repulsion term.[31] This modified version of the Rittner potential has been the basis for a number of experimental and theoretical endeavors in recent years.

Experimentally, the binding energy and vibrational frequency of alkali halides were measured by absorption and emission spectroscopy. Infrared absorption spectra have been particularly useful in determining vibrational anharmonicities. Despite the rich experimental data on the ground-state potential and the various theoretical models, direct comparisons between the two have been rare. In Figure 2.4, various theoretical potential curves were plotted against the experimentally derived RKR turning points by Tiemann and his coworkers. As can be seen from this figure, the overall agreements are quite reasonable.

For the excited states, the picture is much less clear. Taking the first exicted state as an example, this state is mainly covalent in nature and is therefore not strongly bound or not bound at all, depending on the interaction strength between this state and the ground state. Deriving an unbound potential energy surface is obviously a more challenging task than for a strongly bound ground state. Another complicating factor is the excited state correlation with ground-state atoms, M ($^2S_{1/2}$) and X ($^2P_{3/2}$). Different total electronic angular momenta (for example, 0, 1, or 2) will give different potential energies at short R's. This means that in the Franck-Condon region the first excited state will split into a number of distinct states; among them some or all may be accessible in a single experiment,

thus making the interpretation of the experimental results even harder.

Since a major portion of this thesis is devoted to the discussion of the first excited state of NaI (Chapter 4), all relevant literature information will be deferred to later sections of this thesis.

V. Summary

In this chapter, a brief overview is given to present a simple picture of the current status of the field of photodissociation of alkali halide molecules, except for the time-domain work. To facilitate further discussions, some basic physical principles that will be involved in later chapters of this thesis are introduced. In particular, a qualitative picture of the origin of the curve-crossing problem is given, along with a detailed discussion of the quantum-mechanical treatment of the problem. In the following chapters, various aspects of the real-time dynamics of photodissociation of alkali halides, that of NaI in particular, will be discussed.

VI. References

1. J. C. McLennan, *Proc. Roy. Soc. London* **91**, 23 (1914).

2. N. Bohr, *Phil. Mag.* **26**, 1 (1913).

3. J. Franck, H. Kuhn, and G. Rollefson, *Z. Physik* **43**, 155 (1927).

4. J. Franck, *Trans. Faraday Soc.* **21**, 536 (1925).

5. G. Herzberg, *Spectra of Diatomic Molecules*, page 194 (Van Nostrand, 1950). E. Condon further developed Franck's main idea and gave it a quantum mechanical basis in *Physical Review* 32, 858 (1928). This vertical transition theory was immediately called the Franck-Condon principle in the literature.

6. H. Hogness, and J. Franck, *Z. Physik*, **44**, 26 (1927).

7. H. Levi, *Doctoral Dissertation*, Friedrich-Wilhelms-Univ., Berlin (1934).

8. (a) D. R. Herschbach, *Angew. Chem. Int. Ed. Engl.* **26**, 1221 (1987). This Nobel lecture provided a vivid account of the early days of crossed-molecular-beam chemistry, including the "early alkali age." The reactions between alkali atoms and alkyl halides have remained one of the favorite subjects for "crossed-beam chemists" for the last thirty years; see, for example, P. S. Weiss, J. M. Mestdagh, H. Schmidt, M. H. Covinsky, and Y. T. Lee, *J. Phys. Chem.* **95**, 3005 (1991) and references therein.

   (b) M. Polanyi, *Atomic Reactions*, Williams and Norgate, London (1932).

   (c) J. L. Magee, *J. Chem. Phys.* **8**, 687 (1940).

9. R. S. Berry, in *Alkali Halide Vapors*, P. Davidovits and D. L. McFadden, eds.

Chapter 3, and references therein, Academic Press, New York (1979).

10. (a) S. H. Schaefer, D. Bender and E. Tiemann, *Chem. Phys. Letters* **92**, 273 (1982);

(b) S. H. Schaefer, D. Bender and E. Tiemann, *Chem. Phys.* **89**, 65 (1984);

(c) H. Bluhm, J. Lindner and E. Tiemann, *J. Chem. Phys.* **93**, 4556 (1982).

11. N. J. A. van Veen, M. S. de Vries, J. D. Sokol, T. Baller and A. E. de Vries, *Chem. Phys.* **56**, 81 (1981).

12. R. D. Bower, P. Chevrier, P. Das, H. J. Foth, J. C. Polanyi, M. G. Prisant and J. P. Visticot, *J. Chem. Phys.* **89**, 4478 (1988).

13. (a) T. S. Rose, M. J. Rosker, and A. H. Zewail, J. Chem. Phys. **88**, 6672 (1988);

(b) M. J. Rosker, T. S. Rose, and A. H. Zewail, Chem. Phys. Letters **146**, 175 (1988);

(c) T. S. Rose, M. J. Rosker, and A. H. Zewail, J. Chem. Phys. **91**, 6672 (1989).

14. L. Landau, *Physik Z. Sowjetunion* **2**, 46 (1932).

15. C. Zener, *Proc. Roy. Soc. London* **A137**, 696 (1933); *ibid.* **A140**, 660 (1933).

16. L. D. Landau and E. M. Lifshitz, *Quantum Mechanics*, §90, Pergamon Press, Oxford (1977).

17. J. N. Murrell and S. D. Bosanac, *Introduction to the Theory of Atomic and Molecular Collisions*, Chapter 6, John Wiley & Sons, New York (1989);

(b) E. E. Nikitin and S. Ya. Umanskii, *Theory of Slow Atomic Collisions*, Chapter 8, Springer-Verlag, Berlin (1984).

18. (a) M. S. Child, in: *Semiclassical Methods in Molecular Scattering and Spectroscopy*, ed. M. S. Child, page 127, and references therein, Reidel, Dordrecht (1980).

(b) M. S. Child, *Molecular Collision Theory*, Chapter 10, Academic Press, New York (1974).

19. R. Grice and D. R. Herschbach, *Mol. Phys.* **27**, 159 (1974); S. A. Adelman and D. R. Herschbach, *Mol. Phys.* **33**, 793 (1977).

20. K. Yamashita and K. Morokuma, *Faraday Discuss. Chem. Soc.* **91**, in press (1991).

21. (a) G. A. L. Delvigne and J. Los, *Physica* **67**, 166 (1973).

22. (a) K. J. Kaufmann, J. R. Lawter, and J. L. Kinsey, *J. Chem. Phys.* **60**, 4016 (1973);

(b) K. J. Kaufmann, J. L. Kinsey, H. B. Palmer, and A. Tewarson, *J. Chem. Phys.* **60,** 4023 (1973).

23. K. R. Wilson, in *Chemistry of the Excited State*, ed. J. N. Pitts, Gordon and Breach (1970), and references therein.

24. R. Bersohn, *Isr. J. Chem.* **14**, 111 (1975), and references therein.

25. W. R. Anderson, B. M. Wilson, and T. L. Rose, *Chem. Phys. Lett.* **48**, 284 (1977);

R. C. Ormerod, W. R. Anderson, and T. L. Rose, *J. Chem. Phys.* **60**, 5109 (1974).

26. T.-M. R. Su and S. J. Riley, *J. Chem. Phys.* **71**, 3194 (1979); **72**, 1614 (1980).

27. A. S. Ragone, D. H. Levy, and R. S. Berry, *J. Chem. Phys.* **77**, 3784 (1982).

28. (a) S. H. Schaefer, D. Bender, and E. Tiemann, *J. Chem. Phys.* **78**, 6341 (1983);

(b) R. S. Berry and D. H. Levy, *J. Chem. Phys.* **78**, 6342 (1983).

29. E. S. Rittner, *J. Chem. Phys.* **19**, 1030 (1951). Another convenient source where one can find a discussion about the Rittner potential is M. Karplus and R. N. Porter, *Atoms and Molecules*, page 250, W. A. Benjamin, Menlo Park (1970).

30. P. Brumer and M. Karplus, *J. Chem. Phys.* **58**, 3903 (1973).

31. M. B. Faist and R. D. Levine, *J. Chem. Phys.* **64**, 2953 (1976).

32. J. Wang, A. J. Blake, D. G. McCoy, and L. Torop, *Chem. Phys. Letters* **175**, 225 (1990).

VII. Tables

Table 2.1:

Q = IP(M) - EA(X), the differences between alkali ionization potentials and halogen electron affinities. (adapted from Reference 9.)

	F	Cl	Br	I
Li	1.991 eV	1.775	2.026	2.329
Na	1.740	1.524	1.775	2.078
K	0.9420	0.7260	0.977	1.280
Rb	0.7770	0.5610	0.812	1.115
Cs	0.4940	0.2780	0.5290	0.832

Table 2.2:

Points R_X of the alkali halides $R_X = e^2/Q$, based on Coulomb curves for ionic states and horizontal lines for atomic states to M $^2S_{1/2}$ and X $^2P_{3/2}$: (adopted from Reference 9)

	F	Cl	Br	I
Li	7.2324 Å	8.1125	7.1075	6.1828
Na	8.2757	9.4486	8.1125	6.9296
K	15.2864	19.8344	14.7387	11.2498
Rb	18.5325	25.6680	17.7337	12.9146
Cs	29.1493	51.7977	27.2207	17.3074

Table 2.3

Potential parameters for NaI

A. Brumer and Karplus (Reference 30)

$$V_1(r) = A_{MX} \exp(-\frac{r}{\rho_{MX}}) - \frac{e^2}{r} - \frac{e^2(\alpha_{M+} + \alpha_{X-})}{2r^4} - \frac{C_{MX}}{r^6}$$

Coefficients	Value	Unit
A_{MX}	2.5563	10^{-9} ergs
ρ_{MX}	0.3816	Å
α_{M+}	0.181	Å3
α_{X-}	7.16	Å3
C_{MX}	8.959	10^{-60} erg cm6

B. Faist and Levine (Reference 31)

$$V_1(r) = \{A_{ion} + (\frac{B_{ion}}{r})^8\}\exp(-\frac{r}{\rho_{ion}}) - \frac{e^2}{r} - \frac{e2(\alpha_{M+} + \alpha_{X-})}{2r^4}$$

$$- \frac{C_{ion}}{r^6} - \frac{2e^2\alpha_{M+}\alpha_{X-}}{r^7} + E_{th}$$

$$V_2(r) = \{A_{cov} + (\frac{B_{ion}}{r})^{12}\}\exp(-\frac{r}{\rho_{cov}}) + \frac{C_{cov}}{(r)^6}$$

$$V_{12}(r) = A_{12}\exp(-r/\rho)$$

Coefficients	Value	Unit
A_{cov}	3150	eV
B_{cov}	2.647	$eV^{1/12}$ Å
C_{cov}	1000.0	eV Å
ρ_{cov}	0.435	Å
A_{ion}	2760	eV
B_{ion}	2.398	$eV^{1/8}$ Å
C_{ion}	11.3	eV $Å^6$
ρ_{ion}	0.3489	Å
α_{M+}	0.408	$Å^3$
α_{X-}	6.431	$Å^3$
E_{th}	2.075	eV
A_1	0.813	eV
B_1	4.088	$Å^{-1}$
r_1	2.7	Å
A_{12}	17.08	eV
ρ	1.239	$Å^{-1}$

C. Rose, Rosker, and Zewail (Reference 13c)

$$V_1(r) = \{A_{ion} + (\frac{B_{ion}}{r})^8\}exp(-\frac{r}{\rho_{ion}}) - \frac{e^2}{r} - \frac{e2(\alpha_{M+} + \alpha_{X-})}{2r^4}$$

$$- \frac{C_{ion}}{r^6} - \frac{2e^2\alpha_{M+}\alpha_{X-}}{r^7} + E_{th}$$

$$V_2(r) = A_1 exp(-B_1(r - r_1))$$

$$V_{12}(r) = A_{12} exp(-\beta(r - r_x)^2)$$

Coefficients	Value	Unit
A_{ion}	2760	eV
B_{ion}	2.398	$eV^{1/8}$ Å
C_{ion}	11.3	eV $Å^6$
ρ_{ion}	0.3489	Å
α_{M+}	0.408	$Å^3$
α_{X-}	6.431	$Å^3$
E_{th}	2.075	eV
A_1	0.813	eV
B_1	4.088	$Å^{-1}$
r_1	2.7	Å

A_{12}	0.055	eV
β	0.6931	Å^{-2}
r_x	6.93	Å

D. Wang, Blake, McCoy, and Torop (Reference 32)

$$V_1(r) = \{A_{ion} + (\frac{B_{ion}}{r})^8\}exp(-\frac{r}{\rho_{ion}}) - \frac{e^2 D_{ion}}{r} - \frac{e^2(\alpha_{M+} + \alpha_{X-})}{2r^4}$$

$$- \frac{C_{ion}}{r^6} - \frac{2e^2\alpha_{M+}\alpha_{X-}}{r^7} + E_{ion}$$

$$V_2(r) = \{A_{cov} + (\frac{B_{ion}}{r + r_0})^{12}\}exp(-\frac{r + r_0}{\rho_{cov}}) + \frac{C_{cov}}{(r + r_0)^6} + E_{cov}$$

$$V_{12}(r) = A_{12}exp(-\beta(r - r_x)^2)$$

Coefficients	Value	Unit
A_{cov}	3150	eV
B_{cov}	2.710	eV$^{1/12}$ Å
C_{cov}	1000.0	eV Å
ρ_{cov}	0.4277	Å
E_{cov}	3.18	eV
r_0	0.61	Å

A_{ion}	2758	eV
B_{ion}	1.742	$eV^{1/8}$ Å
C_{ion}	12.72	eV $Å^6$
ρ_{ion}	0.3603	Å
α_{M+}	1.375	$Å^3$
α_{X-}	5.446	$Å^3$
E_{ion}	5.312	eV
A_1	0.813	eV
B_1	4.088	$Å^{-1}$
r_1	2.7	Å
A_{12}	0.055	eV
β	0.6858	$Å^{-2}$
r_x	7.293	Å

VIII. Figures

Captions:

Figure 2.1.

A typical potential diagram of an alkali halide MX: the crossing of the ground state and the lowest covalent state.

Figure 2.2.

Curve crossing, the "linearized" Landau-Zener model.

Figure 2.3.

Child's semiclassical theory of curve-crossing.[18] V_+ and V_- represent the adiabatic upper and lower potentials, respectively, while V_1 and V_2 are the diabatic ones. A_- , A_+ and B_+ are the amplitudes of the semiclassical wavefunctions at the classical inner and outer turning points.

Figure 2.4.

Comparison of different ground-state potentials for NaI. Please note that the "Truncated Rittner" potential (Brumer and Karplus) is the ionic diabatic potential; thus, its asymptotic value, corresponding to the separated ion pair of Na^+ and I^-, is different from other potentials.

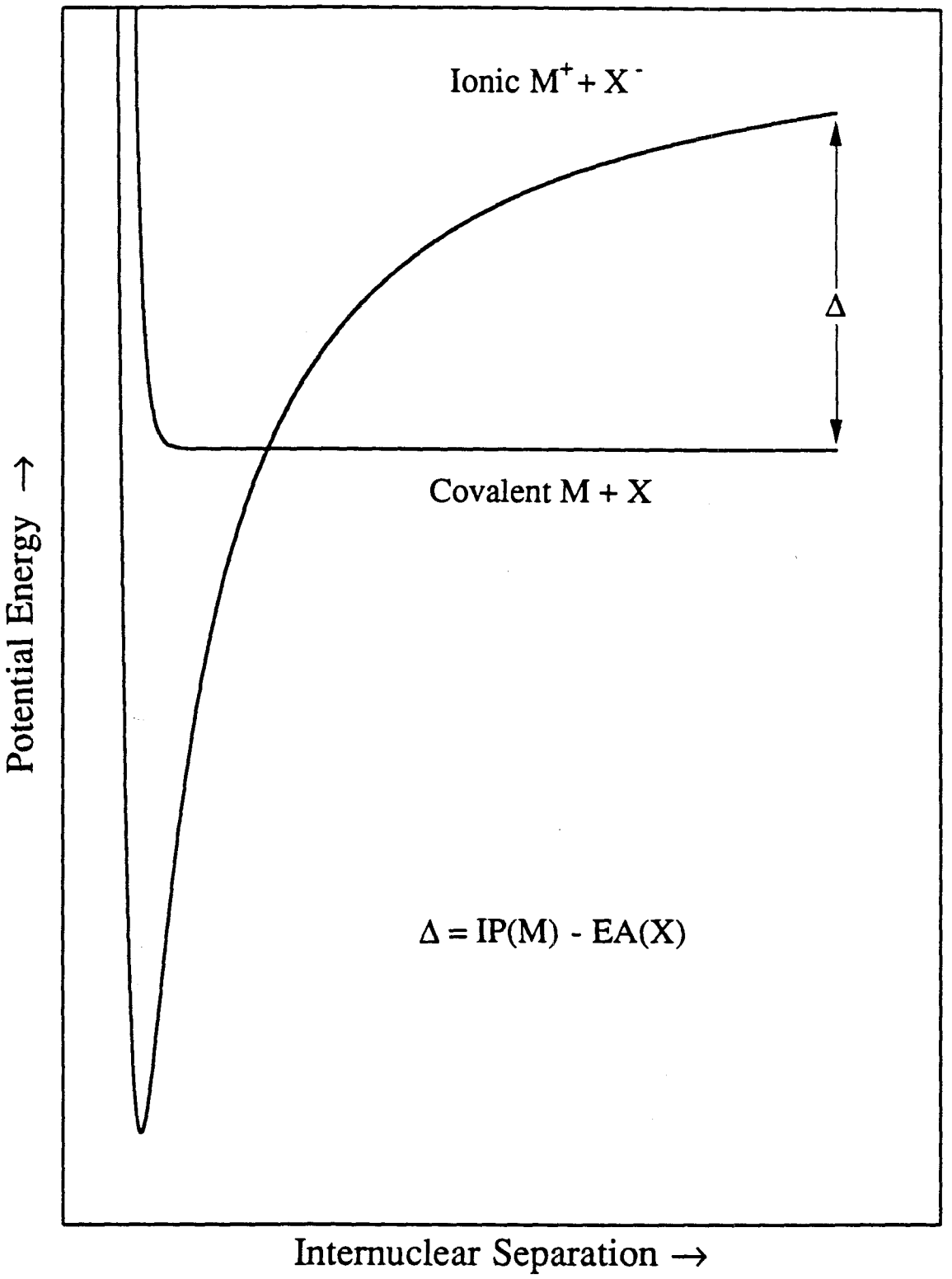
Ionic $M^+ + X^-$
Δ
Covalent M + X
Potential Energy →
Δ = IP(M) - EA(X)
Internuclear Separation →

Figure 2.1

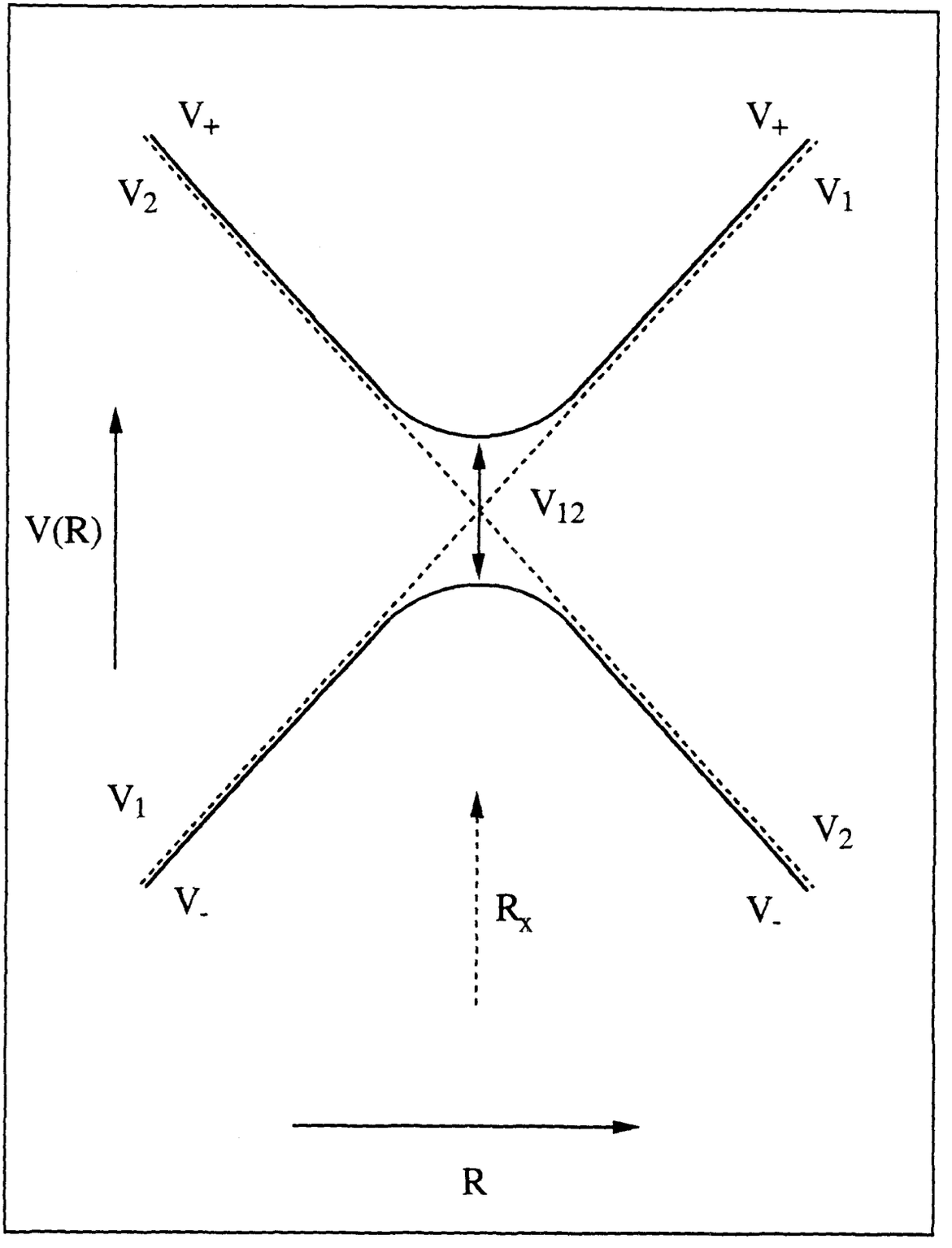

Figure 2.2

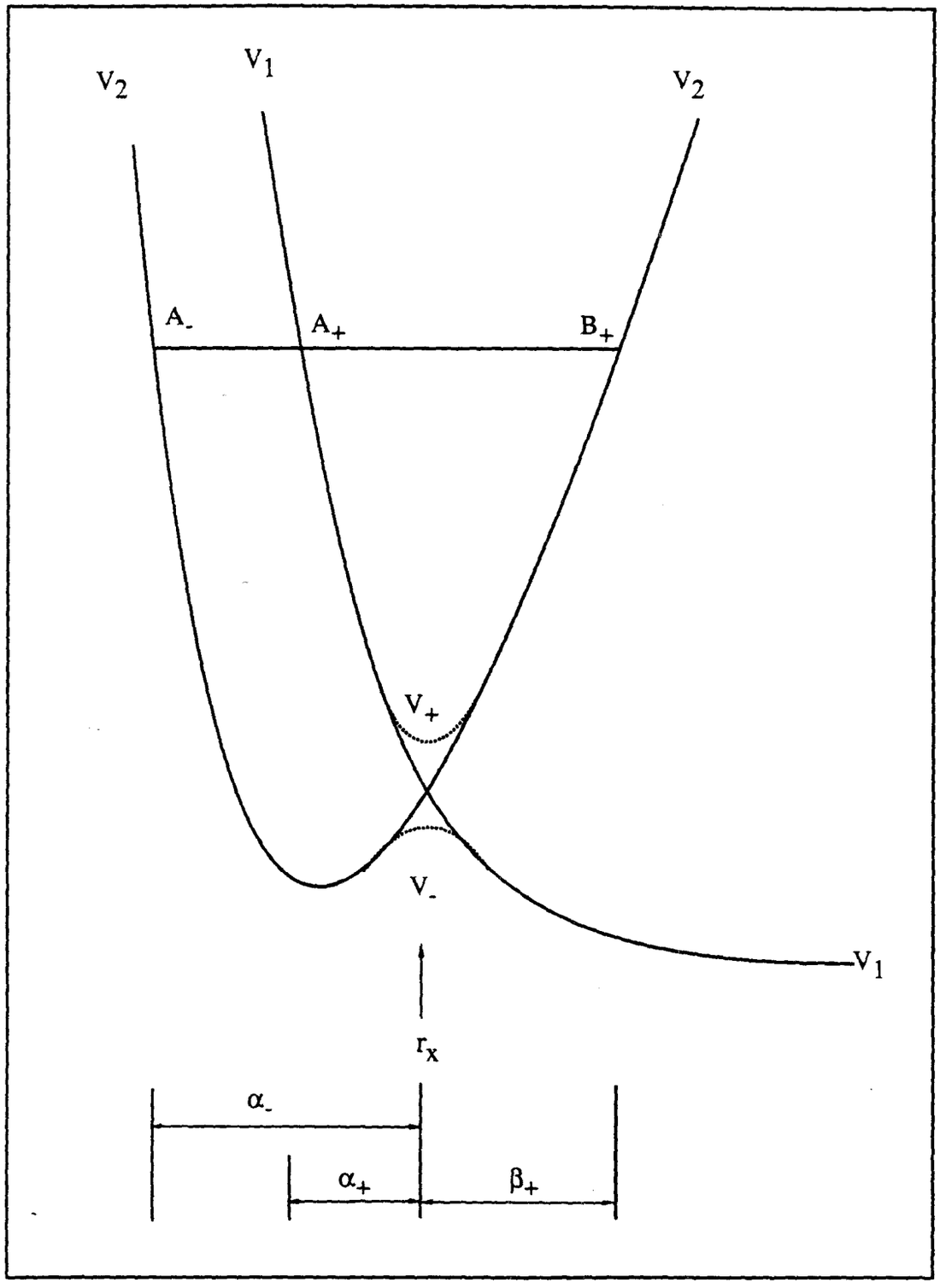

Figure 2.3

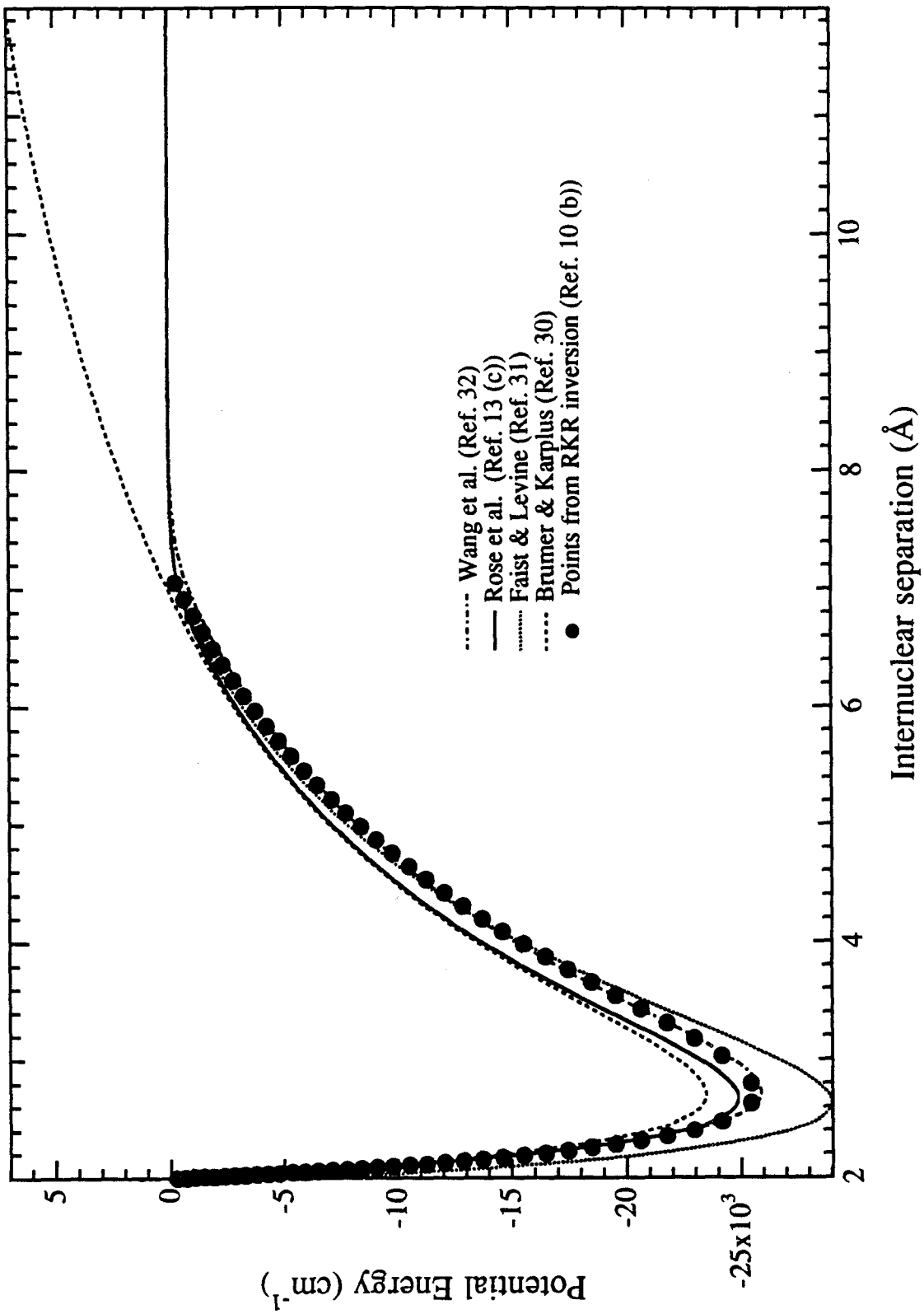
Potential Energy (cm^{-1})
5
0
-5
-10
-15
-20
-25x10^3
2
4
6
8
10
Internuclear separation (Å)
Wang et al. (Ref. 32)
Rose et al. (Ref. 13 (c))
Faist & Levine (Ref. 31)
Brumer & Karplus (Ref. 30)
Points from RKR inversion (Ref. 10 (b))

Figure 2.4

Chapter 3

Femtosecond Transition-state Spectroscopy of Alkali Halides: Experimental Methodology and Some New Developments

I. Introduction

As has been discussed in Chapter one, understanding the transition state in a chemical reaction is one of the most fundamental aspects of chemical dynamics. Among the many approaches developed so far, this research group has been most interested in observing the real-time dynamics of the transition state.[1] This goal was recently accomplished with the availability of femtosecond laser pulses of very high peak power and wide tunability.[2]

The first FTS experiment carried out in this research group was the direct photodissociation of ICN by Scherer *et al.*[3], with compressed picosecond pulses (~ 300 fs) and later by Dantus *et al.*[4], with a CPM-based system (~ 60 fs). Following this success, the second set of experiments performed with this newly established technique focused on the predissociation of alkali halides, and preliminary results were reported by Rose, Rosker, and Zewail.[5] A comprehensive account of this work was published by the same authors, in which experimental details were given along with an in-depth analysis of the experimental findings and a classical simulation of wave-packet dynamics.[6] (This paper will be referenced as FTS IV hereafter.)

Chapter 3 is mainly a continuation and further development of FTS IV; a thorough re-examination of the experimental findings reported in FTS IV is presented. Namely, a quantitative treatment is given to separate wave-packet dephasing dynamics from pure-population decay; a rigorous inversion procedure is established to obtain the Landau-Zener coupling-matrix element from the time-resolved data; and a physical model is developed that explains the power dependence of the on-resonance transients. The remainder of the chapter is organized as follows: A brief description of the experimental setup and procedure is given first, followed by detailed discussions of each of the above topics. The final section summarizes the chapter.

II. Experimental Setup

A colliding-pulse mode-locked dye laser (CPM)-based system was employed in the femtosecond transition-state spectroscopy (FTS) experiments of alkali halides (see Figure 3.1 for a schematic description). Femtosecond pulses with a wavelength around around 620 nm were generated from the CPM pumped by a continuous Ar^+ laser (Coherent, Innova 100) and further amplified by a four-stage pulsed dye amplifier (PDA) pumped by a Q-switched Nd:YAG laser (Quanta-Ray, DCR-3). The output pulses from this system had ~300 μJ energy, and a 20 Hz repetition rate. The temporal pulse width was measured and found to be as short as 60 fs (assuming a hyperbolic-secant squared pulse shape).

The experiments required broadly tunable radiation at both the pump (UV) and probe (visible) wavelengths. Tunable probe pulses (550 nm to 730 nm) were obtained by focusing part of the PDA output into a D_2O cell to generate a white-light continuum that was frequency-selected by an interference filter with a bandwidth of 10 nm. Tunable pump pulses (280 nm to 365 nm) were generated by amplifying a portion of another continuum by the residual 532 nm light from the same Nd:YAG laser before frequency-upconverted by second-harmonic generation in a Type-I KD*P crystal. Pump pulses at 391 nm were obtained by sum-frequency generation through mixing the amplified CPM radiation (623 nm) and the residual fundamental beam of the Nd:YAG laser at 1064 nm.

The sodium-iodide sample (Aldrich, purity better than 99.999%) was contained in an 8 cm-long, vacuum-sealed quartz cell with a side arm. Prior to sealing, care was taken to remove excess moisture that was absorbed by the sample via heating the salt in the quartz cell at 200 °C under vacuum (< 10^{-6} Torr) for more than 6 hours . For all experiments, the main body of the cell was heated to ~ 650 °C in an oven, while the side arm was maintained ~ 50 °C lower than the oven temperature to avoid salt deposition on the cell windows. The

vapor pressure of the sample was estimated to be about 100 mTorr at 650 °C, corresponding to a number density of $5x10^{17}$ molecules/cm^3.[7]

The pump-and-probe beams were delayed in time relative to one another by a high-resolution Michelson interferometer arrangement. These beams were near-collinearly recombined and focused into the NaI sample cell by a 20-cm focal-length lens. The laser-induced fluorescence (LIF) was collected in a direction perpendicular to the pump/probe beams by f/3 collection optics. In order to minimize the scattered laser light and other unwanted background light, the collected LIF was sent through a 1/3-meter monochromator that was tuned to the free, unresolved Na D lines (589 nm). A layout of the experimental setup is given in Figure 3.2. The fluorescence was detected with a photomultiplier tube and the voltage signal was integrated by a digital boxcar integrator (Stanford Research, Model SR 250) without further amplification. The gating of the voltage signal was achieved by selecting an appropriate time window to contain the 16 ns decay transient, which is characteristic of Na D lines. Both the optical delay line of the Michelson interferometer and the boxcar were controlled by a personal computer (Apple, Macintosh II). The data acquisition routines were developed by this group and extensively documented in two previous Ph.D. dissertations.[8,9] High signal-to-noise ratio was achieved by numerically averaging up to 200 separate data sets, while 40 to 50 scans were averaged for a typical transient.

A great deal of effort was focused on maintaining consistent experimental conditions, *i.e.*, proper attenuation and polarization of the pump/probe beams, adequate equilibration of the oven and side-arm temperatures, and optimized configuration for the collection optics. Emphasis was also placed on fully characterizing the pump-and-probe pulses. For each data set, the spectrum of the pump and the probe was taken separately. The temporal profile of the pump and the probe was recorded with the measurement of the cross-correlation signal in a Type-I KD*P crystal whenever possible. Occasionally, the

cross-correlation signal could not be obtained either because of the lack of a suitable detector in the infra-red or to the low power of the pump-and-probe beams when both were generated via the white-light continuum. As dual white light continua also produce a poor signal-to-noise ratio in the alkali halide transients, this type of experimental arrangement was avoided.

III. Results and Discussions

A pictorial description of the wave-packet dynamics in the alkali halide reaction is shown in Figure 3.3, which illustrates the evolution of the wave packet during photon-induced predissociation. At time zero, a wave packet is promoted from the ground ionic state X $^1\Sigma_0^+(v'' = 0)$ to the repulsive limb of the A 0^+ state by the pump pulse; the wave packet then proceeds to propagate towards the lower potential energy regions of larger internuclear separation. When the crossing region is encountered, the wave packet will bifuracate into two components; one is trapped inside the adiabatic well, while the other escapes diabatically to the outside and gives the final products of the reaction, free Na and I atoms. The relative weight of these two components is determined by the Landau-Zener curve-crossing probability. The trapped portion of the wave packet executes a periodic motion inside the adiabatic well; whenever the crossing region is met, a fraction is lost because of non-adiabatic crossing until the reaction is complete, *i.e.*, until there are no molecules left in the transition region. The purpose of the probe photon is to follow in real time the wave-packet motion by opening a "window" along a certain internuclear separation.

Experimentally, the dynamics of the alkali halide dissociation reaction can be elucidated by varying a number of parameters. In the following subsections, the results from such experiments: probe-tuning, pump-tuning, and power dependence, are presented

and discussed, with emphasis on the basic physics that underlines such simple predisssociation processes.

III.1 Probe Tuning and Population Decay vs. Wave-Packet Dephasing

Varying the probe wavelength is equivalent to changing the position of the observation "window" along the reaction coordinate. For example, when the probe is tuned to 589 nm, it is in resonance with the free Na D line transitions that occur at very large values of the internuclear separation. The fluorescence transients obtained under such conditions reflect the appearance of the free Na atoms; this is called λ_2^{∞} probing, where the "2" refers to the probe pulse and the "∞" indicates the large internuclear separation characteristic of resonance. If the probe is tuned away from 589 nm, to either the red or the blue side, the resulting fluorescence transients can no longer correspond to the free Na (one of the final products); therefore, they must originate from a species in the transition state. Thus, this experiment invokes λ_2^{*} probing, where the asterisk mark indicates the transition state.

A comparison of the results from λ_2^{∞} and λ_2^{*} probing is shown in Figure 3.4. The λ_2^{∞}-probe transient shows an initial sharp rise, followed by a series of stair-caselike plateaus, while the λ_2^{*}-probe signal displays a damped oscillation whose frequency matches that observed in the λ_2^{∞}-probe case. This observation clearly establishes the qualitative nature of the on-resonance (λ_2^{∞}) and off-resonance (λ_2^{*}) transients: the off-resonance signal reflects the population inside the adiabatic well; the on-resonance signal follows the free Na build-up. The oscillation period of the off-resonant transient is determined by the local vibrational frequency, as can be measured by high-resolution,

frequency-domain spectroscopy,[10] while the overall decay is caused by the Landau-Zener crossing. In fact, the relation between these two kinds of transients can be further illustrated by the resemblance between the on-resonance transient and the dotted curve, which was obtained by integrating the off-resonance transient over time.

Another important aspect of the wave-packet evolution is revealed by a more careful comparison of these two kinds of transients.[11] The single exponential rise time of the on-resonance transient is about 6 ps, while the amplitude of the off-resonance signal decays with a much faster time constant of 3 ps. This apparent discrepancy can be reconciled by noting that even though the wave packet prepared by a femtosecond laser pulse might be approaching a Gausssian wave packet, it is not moving on a perfect quadratic potential. Because of the anharmonicity of the adiabatic potential, the quasi-Gaussian wave packet will disperse while oscillating back and forth on the adiabatic potential. This dispersion causes the broadening of the wave packet and rapid decrease of the peak amplitudes, which are directly related to the peak height of the wave packet. Another cause of broadening in the off-resonance peaks stems from the many rotational levels populated under the experimental conditions. Each rotational state supports its own coherent vibrational wave packet; the average oscillation period is slightly different for different rotational states. With these factors in mind, if the decay of the peak *areas* is examined, the time constant is also 6 ps, identical with the exponential rise-time of the on-resonance transient (see Figure 3.5). Thus, the faster decay of the off-resonance signal is a result of both the population loss that is due to curve crossing and the wave-packet dephasing. Since the collision frequency in the sample cell at ~100 mTorr is much less than one collision per nanosecond, the observed dephasing effect is purely due to the anharmonic nature of the potential. As can be seen from the relevant time constants, the pure dephasing time (~ 6 ps) is comparable to the population-decay constant (also about 6 ps).

III.2 Pump Tuning and the Landau-Zener Coupling Constant

Figure 3.6 shows the effect of tuning the pump wavelength from 300 nm to 365 nm on the off-resonance transients. When the pump wavelength is varied, the total energy of the wave packet is changed; as a result, the initial starting position of the wave packet on the repulsive branch is also changed. As can be seen from this figure, the oscillation period decreases when the wavelength is tuned to the red, *i.e.*, when the available energy to the wave packet is decreased. Following the same trend, the corresponding decay rate also decreases. As mentioned in the previous subsection, there are three aspects of the information imbedded in these off-resonance transients. In addition to the vibrational dephasing, they also contain information about the local vibrational frequency and the curve-crossing probability as manifested by the oscillation period and the damping rate, respectively. While the oscillation period data are directly connected to the potential and are therefore vital for inverting the FTS results to PES, this subsection will focus only on obtaining the Landau-Zener coupling constant. Potential inversion is deferred to a later chapter.

As has been discussed in Chapter 2, the population decay of the off-resonance transient can be described reasonably well by the Landau-Zener formula:

$$P_{LZ} = exp\left\{ - \frac{4\pi^2}{hv(E,J)} \frac{V_{12}^2}{|F_1 - F_2|} \right\}, \tag{3.1}$$

where V_{12} is the coupling matrix element, $v(E,J)$ is the relative velocity of the atoms at the crossing point at a given excess energy E and rotational quantum number J, and the F_1 and F_2 are the slopes of the diabatic potentials at the crossing point. Since the covalent potential at the crossing point R_x is essentially flat, and the ionic potential is dominated by the $1/R_x$ Coulombic attraction term:

$$|F_1 - F_2| = \left| \frac{dV_1(r)}{dr}\Big|_{R_x} - \frac{dV_2(r)}{dr}\Big|_{R_x} \right| \approx \frac{1}{R_x^2}, \qquad (3.2)$$

P_{LZ} can be deduced from the off-resonance transients, and the excess energy is determined by the pump wavelength and the average rotational quantum number, leaving the coupling-matrix element as the *only* unknown quantity in Equation (3.1).

P_{LZ} is obtained in the following way. First, the oscillation period T must be determined. For a given transient, T can be measured directly by fitting the curve to a decaying cosine function until all the peak positions are matched. Secondly, the population-decay constant t must be extracted from the experimental data. This procedure is complicated by the fact that the off-resonance transient is not in a simple exponential decay form; instead, it is deeply modulated. As has been discussed earlier in this chapter, important information about the wave-packet dephasing is imbedded in the broadening of the off-resonance peaks and can be extracted and separated from the population-decay dynamics. However, that procedure requires very high signal-to-noise ratio and a sufficient number of data points to cover each individual peak and is realistic for only one particular pump-probe combination (310 nm pump, 620 nm probe), in which the signal-to-noise ratio is adequate. To derive the population-decay-time constant without the interference from the dephasing dynamics over a wide wavelength range, each experimental decay curve is integrated over time, and the integrated curve is then fitted to a single exponential rise function by a non-linear least-squares fitting routine (a typical fit is shown in Figure 3.7). Using this technique, the dephasing dynamics as reflected in the broadening of the peaks is eliminated, while the overall population decay characteristics are preserved. Finally, combining the period and decay-constant data, P_{LZ} is computed by the following equation:

$$P_{LZ} = (1 - exp(-T/t))^{1/2}. \qquad (3.3)$$

The 1/2 exponent is due to the fact that P_{LZ} is defined as the escaping probablity for one crossing, while $1- exp(-T/t)$ measures the decay probability over one whole period, *i.e.*, one round trip, or two crossings. The relevant data are listed in Table 3.1.

Re-arranging Eq. (3.1) and taking logarithms on both sides, one obtains the following form of the Laudau-Zener expression:

$$ln(P_{LZ}) = -\frac{4\pi^2 V_{12}^2}{h\,|F_1 - F_2|}\left(\frac{2\mu}{E_{ex}}\right)^{1/2}, \qquad (3.4)$$

where μ is the reduced mass and the E_{ex} is the excess energy (*i.e.*, recoil energy), including both the vibrational energy and the rotational energy released due to the increase of the internuclear separation at the crossing point. Following this modified version of the Landau-Zener formula and using wavenumber as the energy unit, Equation (3.4) can be written in the following form:

$$ln(P_{LZ}) = -1.3958 \times 10^{-3} \times V_{12}^2 \frac{1}{E_{ex}^{1/2}} \qquad (3.4')$$

If one plots $ln(P_{LZ})$ vs. $E_{ex}^{-1/2}$, the result should be a straight line that goes through the origin; the slope of the line is proportional to the square of the coupling-matrix element V_{12}. Such a plot is shown in Figure 3.8; the Landau-Zener coupling constant derived from this figure is 415 ± 15 (one standard deviation) cm^{-1}, in close agreement with previous theoretical and experimental values.[10, 12-14]

III.3 Power Dependence

A power-dependence study of the FTS transients of NaI demonstrates a number of interesting features. The off-resonant transient wave form is remarkably insensitive to the pump and probe powers even when they are varied over a factor of 100. The shape of the on-resonance transient also remains unchanged when the probe power is varied. However, when the pump power is increased, the on-resonance transient shape changes drastically, as shown in Figure 3.9. Initially, at very low pump power the on-resonance signal displays a sharp rise, followed by a series of ascending plateaus that are in turn washed out to become a slow rise. As discussed in subsection A, the waveform can be understood as reflecting the build-up of free sodium atoms. When the pump power is increased gradually, the rise part of the transient is flattened out and a plateau level is reached quickly; when the power is increased further, the transient even starts to descend and resembles the appearance of the off-resonance transients. This trend was reported in FTS IV, even though it was not very well understood at the time and remained puzzling for quite some time. The following paragraphs will highlight a recently developed hypothesis that can explain all the experimental observations made so far.

Since the shape of the on-resonance transient does not depend on the power level of the probe beam, its change of shape as a function of the pump power must be due to the transition state as prepared by the pump pulse, not some final state effect as may be introduced by the probe pulse. Furthermore, a close examination of the high-power transient shows that it has the same oscillation structure as an off-resonance transient; even the period matches that of the off-resonance signal, which is a signature of the A 0^+ state. This unequivocally establishes that the on-resonance transients still originate from the same intermediate state, no matter in what form (the low-power form or the high-power form) it appears. As a result, it can be ruled out that this power dependence is caused by multiphoton processes.

With these clues in hand, the following hypothesis is given. The on-resonance transient, as probed by a 590-nm pulse with a bandwidth of 10 nm, is comprised of two components: the "true" on-resonance part that is due to the absorption of a very narrow portion of the probe light centered around 589 nm by free sodium atoms outside the potential well, and the off-resonance part that is caused by the absorption over the whole probe pulse spectrum by the NaI molecules inside the trapping well, i.e., the transition state. At low pump powers, the on-resonance component dominates, while when the pump power is increased, so does the relative weight of the off-resonance contribution.

First of all, this hypothesis is plausible because off-resonance transients have been observed both to the red and blue of 590 nm. There is no reason to doubt that transient species trapped in the potential well will not absorb the 590 nm light, even though the absorption cross sections of the transient species and the free sodium atoms at 590 nm might be rather different. Secondly, not only does the beating frequency of the high-power transient match the off-resonance pattern, but also the overall decay time is on the same order as the off-resonance signal. This further supports the assumption that there is an off-resonance contribution to the on-resonance transient. Finally, Na is known to have a very large absorption cross section at 590 nm, and it can absorb only a very small portion of the 10 nm bandwidth probe light because of the sharpness of the atomic transition. Thus, it is not hard to imagine that when a large number of free sodium atoms are produced by the high-powered pump pulse, these Na atoms will deplete the part of the probe pulse that matches their absorption profile. Consequently, the on-resonance signal level will not rise farther when all the available photons are consumed, even when the pump power is further increased to produce more and more free Na atoms; on the other hand, the molecules in the transition state, possessing much smaller absorption cross sections and being able to absorb the whole spectrum of the probe pulse, will continue to increase the off-resonance signal level when the pump power is increased without experiencing the "level-off" as the

on-resonance component. The net result is that the transient is dominated by the on-resonance part at low pump powers and by the off-resonance component at high pump powers because of the large absorption cross section and narrow absorption linewidth of free sodium, and the small absorption cross section and wide absorption profile of the transient species of NaI.

To test this hypothesis quantitively, we employ the following simplified kinetic model to describe the pump-probe process with a pump pulse at 310 nm and a probe pulse centered around 590 nm with a 10 nm bandwidth (see Figure 3.10):

Step 1:

$$\begin{aligned} d[NaI](t)/dt &= -I(t)\sigma_{ab}(\lambda/hc)\cdot[NaI](t) + I(t)\sigma_{ab}(\lambda/hc)\cdot[NaI]^{\ddagger *}(t) \\ &= -I(t)\sigma_{ab}(\lambda/hc)([NaI](t) - [NaI]^{\ddagger *}(t)) \\ &= -n_{pump}(t)\sigma_{ab}([NaI](t) - [NaI]^{\ddagger *}(t)), \end{aligned} \qquad (3.5)$$

where $I(t)$ is the laser intensity, σ_{ab} is the absorption cross section of NaI at 310 nm, and $n_{pump}(t)$ is the photon flux and has a unit of number of photons/s·cm^2. In order to know the concentration of NaI molecules excited by a pump pulse with given pulse energy and spot size S, Eq. (3.4) is integrated over the whole pulse width to give the following expression:

$$[NaI]^{\ddagger *}(t_0) = \frac{1}{2}[NaI]_0(1 - e^{-2\sigma_{ab}Npump/S}), \qquad (3.6)$$

where $[NaI]^{\ddagger *}(t_0)$ represents the number density of NaI$^{\ddagger *}$ right after the pump pulse is over, $[NaI]_0$ is the initial NaI concentration, and N_{pump} is the total number of photons in the pump pulse. The fact that the total concentration of NaI in the ground and excited states is conserved quantity is used to derive Eq. (3.6).

After the pump pulse, the NaI molecules in the excited states will undergo a predissociating process to produce Na and I, both in the ground states. Omitting the fine details of the wave-packet oscillations that result in ripples on the experimental transients, the dissociation process can be described by the following equations with a Landau-Zener leaking-rate constant k:

$$[NaI]^{\ddagger *}(t) = [NaI]^{\ddagger *}(t_0)\, e^{-kt}, \tag{3.7a}$$

$$[Na](t) = [NaI]^{\ddagger *}(t_0)\,(1 - e^{-kt}). \tag{3.7b}$$

The next step is for the probe pulse to monitor this process by exciting $NaI^{\ddagger *}$ or Na into an excited state, which in turn emits light around 590 nm (Na D lines). Ideally, one would like to separate the dynamics of $NaI^{\ddagger *}$ (decay) from that of Na (build-up), by tuning the probe wavelength in resonance with either $NaI^{\ddagger *}$ or Na; however, this is not possible in this particular case because of the finite spectral width associated with the probe beam. Thus, we have to consider both probe channels.

Following the same procedures as in deriving Eq. (3.5) and (3.6), we have

$$d[Na^*](t)/dt = \sigma_{Na} \cdot n_{probe}(t)([Na](t) - [Na^*](t)), \tag{3.8}$$

where σ_{Na} is the total absorption cross section of Na D lines, $n_{probe}(t)$ is the photon flux of the probe beam, and its useful spectral width is determined by the absorption profile of the free Na atoms. If we multiply both sides of Eq. (3.8) by the interaction volume of the probe-and-pump beams, the number density terms (marked by square brackets) become numbers of molecules:

$$dN_{Na^*}(t)/dt = \sigma_{Na} \cdot n_{probe}(t)(N_{Na}(t) - N_{Na^*}(t)). \tag{3.9}$$

Integrating over the probe-pulse duration, we have:

$$N_{Na^*}(t_1) = N_{Na}(t_1) \cdot \frac{1 - exp(-\sigma_{Na}N_{Na} - 2N_{probe}(Na)/S)}{2 - N_{Na}/N_{probe}(Na)exp(-\sigma_{Na}N_{Na} - 2N_{probe}(Na)/S)}, \qquad (3.10)$$

where $N_{probe}(Na)$ means the total number of probe photons that fall into the absorption profile of free Na lines, t_1 is the time at which the probe-pulse is just over. This equation is obtained under the assumption that the probe pulse duration is much shorter than the inverse of the Landau-Zener decay rate, which is a very good approximation since the probe pulse is typically 150 fs long and the lifetime of the predissociating molecules is about 10 ps. Similarly, for the off-resonance contributions, the expression is identical to the last equation, when all the Na's are replaced by $NaI^{\ddagger *}$'s.

It is rather instructive to examine the asymptotic behaviors of Eq. (3.10). If $N_{probe}(Na)(t_{probe}) >> N_{Na}(t_{probe})$, then $N_{Na^*}(t_{probe}) \approx N_{Na}(t_{probe})/2$, which means that 50% of the free sodium atoms will be promoted to the excited state, and we are in a saturation regime. In this case, the time dependence of the FTS signal that is due to the on-resonance absorption will still follow the build-up of free Na atoms faithfully. On the other hand, if we are in the other extreme case where $N_{Na}(t_{probe}) >> N_{probe}(Na)$, then $N_{Na^*}(t_{probe}) \approx N_{probe}(Na)$ and we are in a depletion regime. In this case, the on-resonance signal will quickly reach a plateau level, as limited by the number of photons available, and will remian unchanged as long as the migration of Na atoms out of the interaction volume that is due to thermal diffusion is not significant. Thus, if we look at the time dependence of the on-resonance signal alone, it no longer follows the build-up of free Na atoms; the nominal build-up time for this transient will be much faster than 1/k.

In principle, the same arguments should be valid for the off-resonance components. However, since the absorption cross section is relatively small and the number of probe photons available is much larger, the depletion regime is essentially not reachable. As has been demonstrated experimentally, the off-resonance signal has a very weak power dependence, as no observable change in the waveform of the transients is detected over two order-of-magnitude changes in both pump and probe powers.

With these results in mind, a set of experimentally realistic parameters are applied to simulate the experimentally observed transients. The results are displayed in Figure 3.11. From this figure, it can be clearly seen that when pump power is gradually increased from 5 nJ to 100 μJ, the simulated transient goes from a simple exponential rise function to an almost exponential decay function, closely resembling the trend in the power dependence of experimental transients. In Figure 3.12, the experimental transients are fitted to a sum of a single exponential rise and a single exponential decay. While the time constant for the decay part remains basically unchanged (from 8 ps to 10 ps), the exponential rise constant becomes shorter and shorter when the pump power is increased, from ~ 5 ps to 0.3 ps. This trend is exactly what is predicted by the aforementioned model. These excellent agreements between experiments and the kinetic model strongly support the proposed theoretical model. A further experimental test will be reducing the spectral bandwidth of the probe pulse, therefore changing the relative weight of on-resonance and off-resonannce components.

IV. Summary

In this chapter, a number of new developments of the femtosecond transition-state spectroscopy of NaI were discussed. These included the separation of wave-packet dephasing dynamics from that of predissociation, the inversion of time-resolved data to

obtain the Landau-Zener coupling-matrix element, and the development of a realistic physical model that explains the power dependence of the "on-resonance" transients. In the next chapter, new experimental results are presented and new procedures are developed to invert the FTS data to potential-energy curves.

V. References

1. For reviews of the research activities of this group, see:
   (a) M. Gruebele and A. H. Zewail, *Phys. Today* **43**, No. 5, 24 (1990);
   (b) L. R. Khundkar and A. H. Zewail, *Ann. Rev. Phys. Chem.* **41**, 15 (1990);
   (c) A. H. Zewail, *Science* **242**, 1645 (1988);
   (d) A. H. Zewail and R. B. Bernstein, *Chem. Eng. News* **66**, 24 (1988).

2. (a) R. L. Fork, B. I. Greene, and C. V. Shank, *Appl. Phys. Letters,* **38**, 671 (1981);

   (b) For a comprehensive review of the techniques of the generation and amplification of ultrashort laser pulses, see: J. D. Simon, *Rev. Sci. Instrum.* **60,** 3597 (1989).

3. N. F. Scherer, J. L. Knee, D. D. Smith, and A. H. Zewail, *J. Phys. Chem.* **89,** 5141 (1985).

4. M. D. Dantus, M. J. Rosker, and A. H. Zewail, *J. Chem. Phys.* **87**, 2395 (1987).

5. (a) T. S. Rose, M. J. Rosker, and A. H. Zewail, *J. Chem. Phys.* **88**, 6672 (1988);

   (b) M. J. Rosker, T. S. Rose, and A. H. Zewail, *Chem. Phys. Lett,* **146**, 175 (1988).

6. T. S. Rose, M. J. Rosker, and A. H. Zewail, *J. Chem. Phys.* **91**, 7415 (1989).

7. J. C. White, *Appl. Phys. Lett.* **33**, 335 (1979).

8. L. W. Peng, Ph.D. Thesis, Caltech, Pasadena (1991).

9. M. Dantus, Ph.D. Thesis, Caltech, Pasadena (1991).

10. S. H. Schaefer, D. Bender, and E. Tiemann, *Chem. Phys.* **89**, 65 (1984).

11. P. Cong, A. Mokhtari, and A. H. Zewail, *Chem. Phys. Lett.* **171**, 12 (1990).

12. R. Grice and D. R. Herschbach, *Mol. Phys.* **27**, 159 (1974).

13. K. Yamashita and K. Morokuma, *Faraday Discuss. Chem. Soc.* **91**, in press (1991).

14. G. A. L. Delvigne and J. Los, *Physica* **67**, 166 (1973).

15. P. Davidovits and D. C. Brodhead, *J. Chem. Phys.* **46**, 2968 (1967).

16. S. Chu, L. Hollberg, J. E. Bjorkholm, A. Cable, and A. Ashkin, *Phys. Rev. Lett.* **55**, 48 (1985).

VI. Tables

Table 3.1 Data for obtaining the Landau-Zener coupling-matrix element

Pump wavelengh (nm)	Recoil energy (cm^{-1})	Decay time constant (ps)	Oscillation period (ps)	$\ln(P_{lz})$	Matrix element (cm^{-1})
299.8	8009	9.45	1.620	-2.499	399.0
301.5	7714	12.69	1.536	-2.835	421.6
304.0	7430	17.59	1.383	-3.256	447.7
306.9	7068	13.39	1.292	-3.055	428.3
310.8	6639	13.91	1.198	-3.166	425.8
312.0	6480	12.93	1.193	-3.099	422.1
313.9	6310	12.15	1.156	-3.069	417.2
317.4	5960	14.46	1.100	-3.288	425.8
319.9	5700	10.90	1.088	-3.022	403.6
320.5	5650	12.17	1.087	-3.131	410.0
324.4	5360	11.59	1.042	-3.124	404.1
330.3	4915	12.59	1.014	-3.232	402.3
332.4	4750	12.42	1.002	-3.230	398.7
337.8	4670	13.40	0.985	-3.322	402.6
<Average>					414.9
<Standard deviation>					14.4

VII. Figures

Captions:

Figure 3.1

Schematic of the femtosecond laser system: left panel, the Colliding Pulse Mode-locked (CPM) dye laser; right panel: the Pulsed Dye laser Amplifier (PDA). Key: SAJ = saturable absorber dye jet; GJ = gain dye jet; OC = output coupler; C1 - C4 = dye amplifier cells; CL1 - CL3 = cylindrical lenses; PH = pinhole. Adapted from M. J. Rosker, M. Dantus, and A. H. Zewail, *J. Chem. Phys.* **89**, 6113 (1988).

Figure 3.2

Schematic of a typical pump/probe generation scheme for the FTS experiments of alkali halides. Key: CG = continuum generation cell (D2O); IF = interference filter; SHG = second harmonic-generation crystal; CF = color filter; AMP = amplification stage. Adapted from the same reference as in Figure 3.1.

Figure 3.3

Schematic representation of the pump/probe process and the relevant low-lying potential-energy curves for the FTS experiments of alkali halides. A pump pulse at wavelength λ_1 prepares a coherent wave packet in the covalent A 0^+ state. A probe pulse at wavelength λ_2^* detects the dynamics of the wave packet evolution inside the potential well, while a probe pulse at wavelength λ_2^∞ monitors the build-up of the final products.

Figure 3.4

Comparison of the "on-resonance" and "off-resonance" transients. The upper curve is obtained by exciting NaI at 310 nm and probing at 590 nm (with a 10 nm bandwidth). The ascending staircase reflects the gradual build-up of free Na atoms

with a period of ~ 1 ps. The lower open-circle curve is the result of changing the probe wavelength to 620 nm.The ~ 1 ps oscillation period matches that of the "on-resonance" curve.The dotted curve is the integrated form of the 620 nm probing transient; it closely resembles the 590 nm probing "on-resonance" curve.

Figure 3.5

Population decay vs. dephasing dynamics. The first seven oscillations of an "off-resonance" transient (310 nm pump, 620 nm probe) were fitted by a sum of Gaussian functions; each of them was matched to one oscillation. The area covered by each Gaussian and the peak amplitude were plotted against time in the insert. As can be seen from the graph, the peak amplitude decays faster than the area. Adapted from Reference 10.

Figure 3.6

The effect of tuning the pump wavelength from 300 nm to 364 nm. The probe wavelength was fixed at 620 nm. See text for further explanations.

Figure 3.7

Fitting of the integrated form of "off-resonance" transients. The integrated curve (3108 Å pump, 6200 Å probe) was fitted to a single-exponential rise function by a non-linear least-squares fitting routine. In this case, the rise time, which measures the population decay, is 10 ps.

Figure 3.8

Inversion of the Landau-Zener coupling-matrix element from FTS. $Ln(P_{LZ})$ is plotted against $1/E^{1/2}$ (E in units of cm^{-1}); the data points are then fitted to a straight line that goes through the origin. From the slope of the straight line, the Landau-Zener coupling-matrix element is derived and found to be 415 $cm^{-1} \pm 30$ cm^{-1} (2σ).

Figure 3.9

Power dependence of the "on-resonance" transients (310 nm pump, 590 nm probe). The relative power levels of the four transients shown here are: (a) 1.0, (b) 2.0, (c) 5.6, (d) 49.2.

Figure 3.10

Schematic of a kinetic model that describes the pump/probe process with a pump wavelength at 310 nm and probe wavelength centered at 590 nm with a 10 nm bandwidth.

Figure 3.11

Simulations of the power dependence of the "on-resonance" transients. Parameters used in the simulation: NaI number density: 1.5x1015/cm^3, laser spot size: 50 μm (diameter), interaction length: 2.5 mm, number of probe photons from 585 nm to 595 nm: $3x10^{10}$ (or about 10 nJ), number of photons that could be absorped by free Na atoms: $1.5x10^8$ (or 0.5% of the overall probe photons), energy of the pump pulses: from bottom up: 20 nJ, 40 nJ, 100 nJ, 1μJ. The absorption cross section for NaI at 310 nm was $2x10^{-17}$ cm^2 (Reference 15), that for Na at 590 nm (combined D lines) was $1x10^{-12}$ cm^2 (Reference 16), and that of [NaI]* was estimated to be $2x10^{-16}$ cm^2 at 590 nm.

Figure 3.12

Fitting of the "on-resonance" transients shown in Figure 3.9 by the sum of single-exponential rise and single-exponential decay functions. The time constant for the decay part remains essentially constant, 8 - 10 ps. However, the rise time decreases with increased power, from 5.6 ps for curve (a) (relative power 1.0) to 0.9 ps for curve (d) (relative power 49.2).

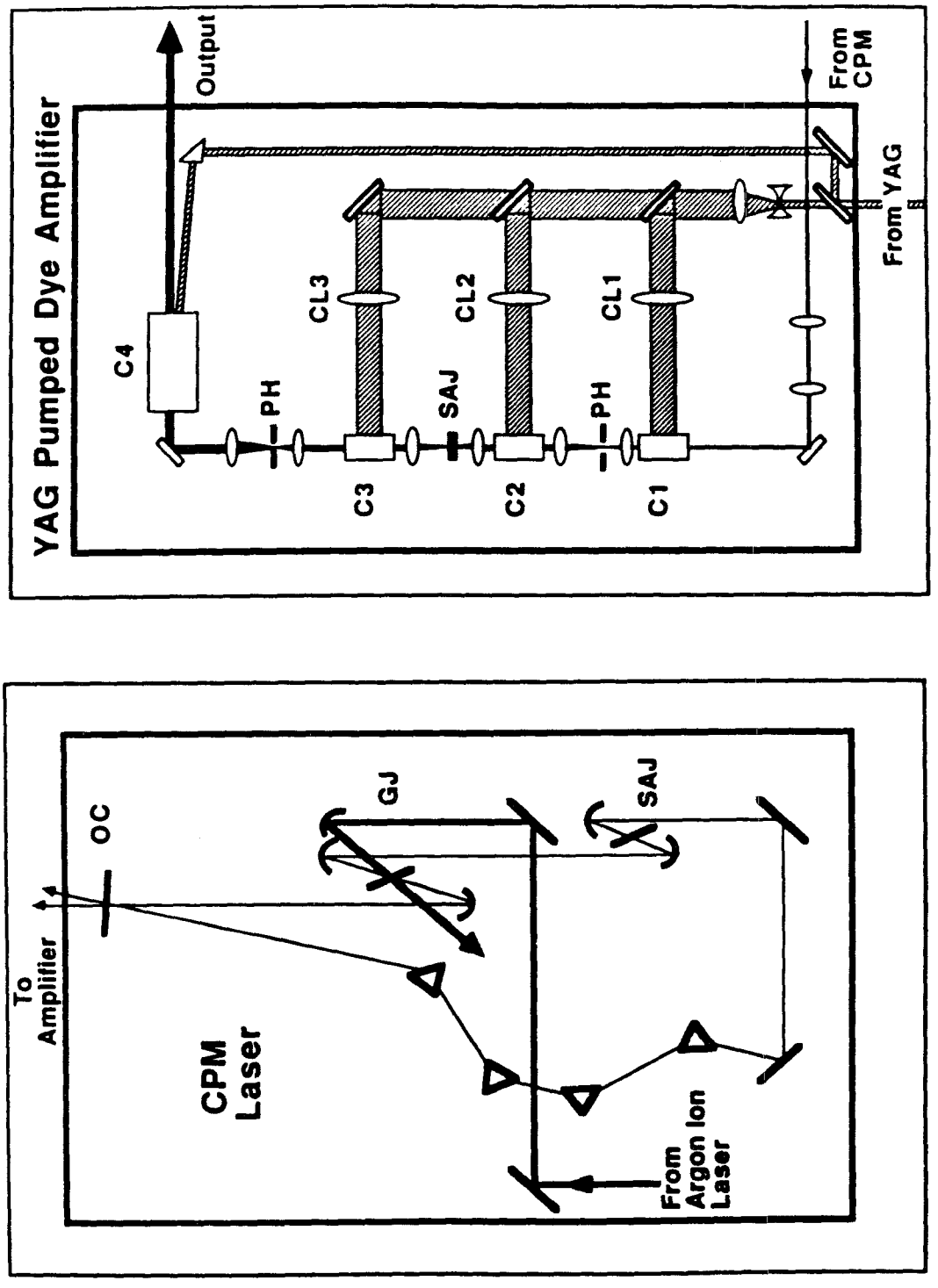
YAG Pumped Dye Amplifier
Output
From CPM
From YAG
C4
CL3
CL2
CL1
PH
SAJ
PH
C3
C2
C1
OC
GJ
SAJ
To Amplifier
CPM Laser
From Argon Ion Laser

Figure 3.1

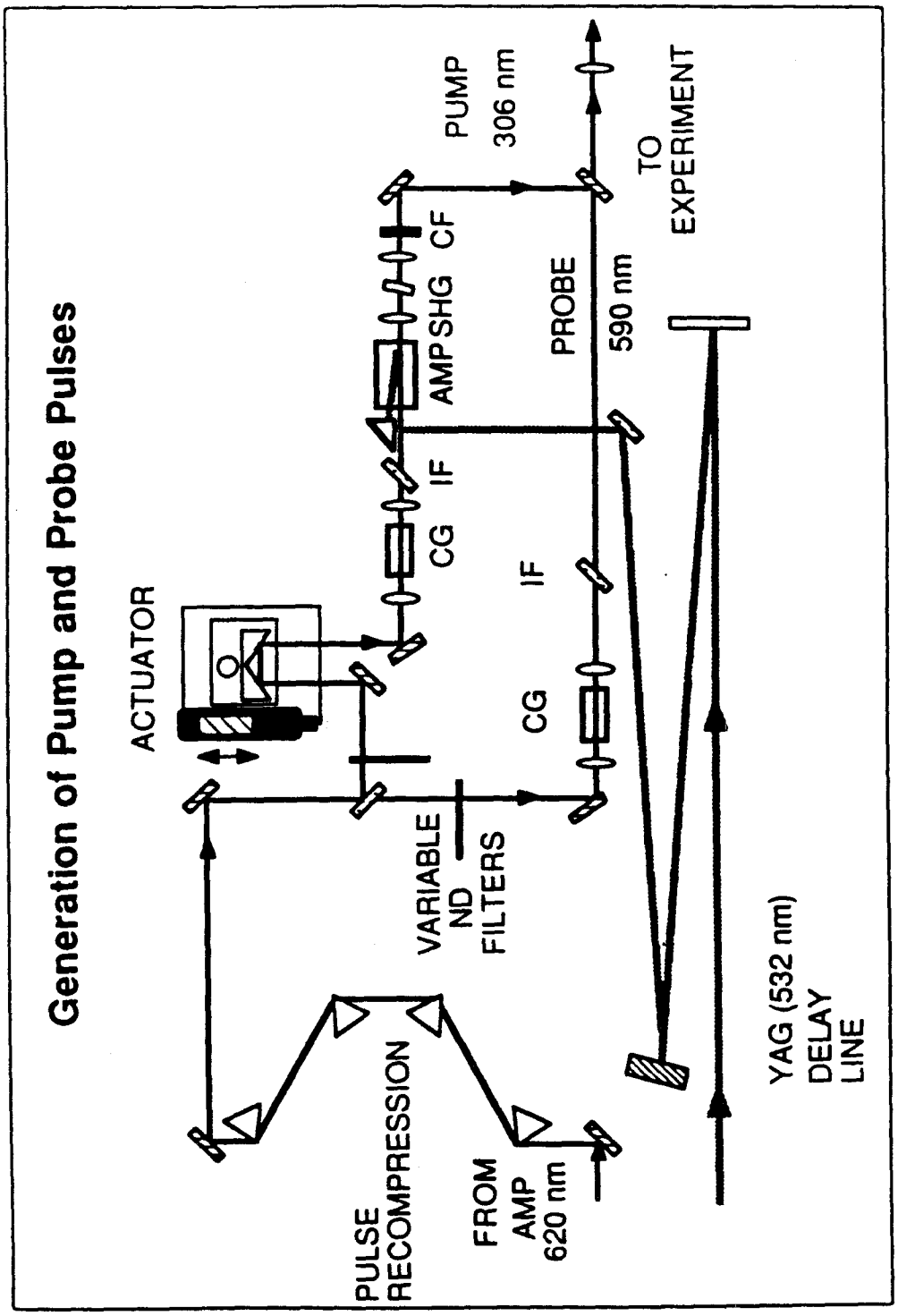
Generation of Pump and Probe Pulses
ACTUATOR
CG
IF
CG
IF
AMP SHG CF
PUMP
306 nm
PROBE
590 nm
TO
EXPERIMENT
VARIABLE
ND
FILTERS
PULSE
RECOMPRESSION
FROM
AMP
620 nm
YAG (532 nm)
DELAY
LINE

Figure 3.2

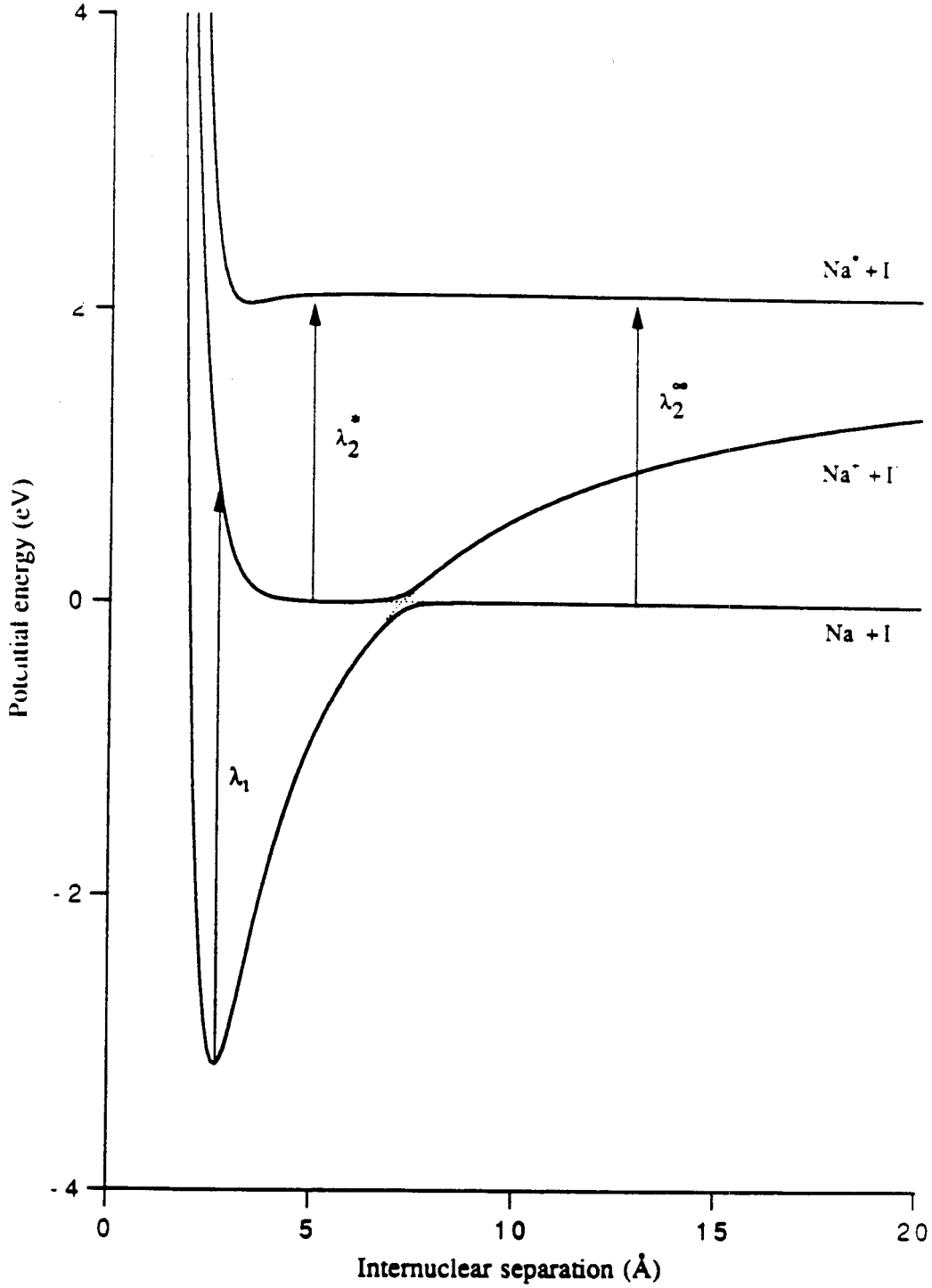
4
2
0
-2
-4
Potential energy (eV)
0
5
10
15
20
Internuclear separation (Å)
Na* + I
Na⁻ + I
Na + I
λ1
λ2*
λ2∞

Figure 3.3

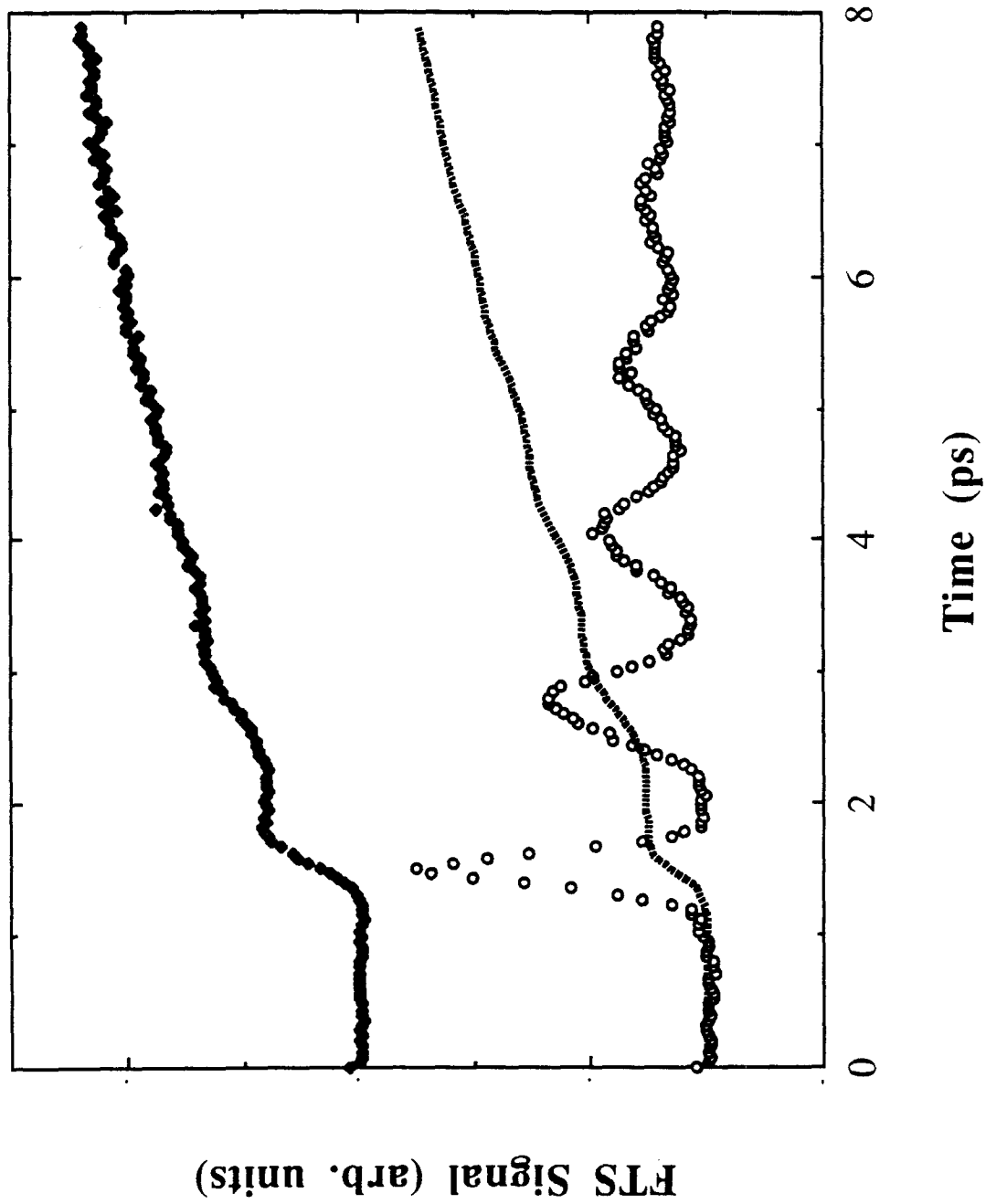

Figure 3.4

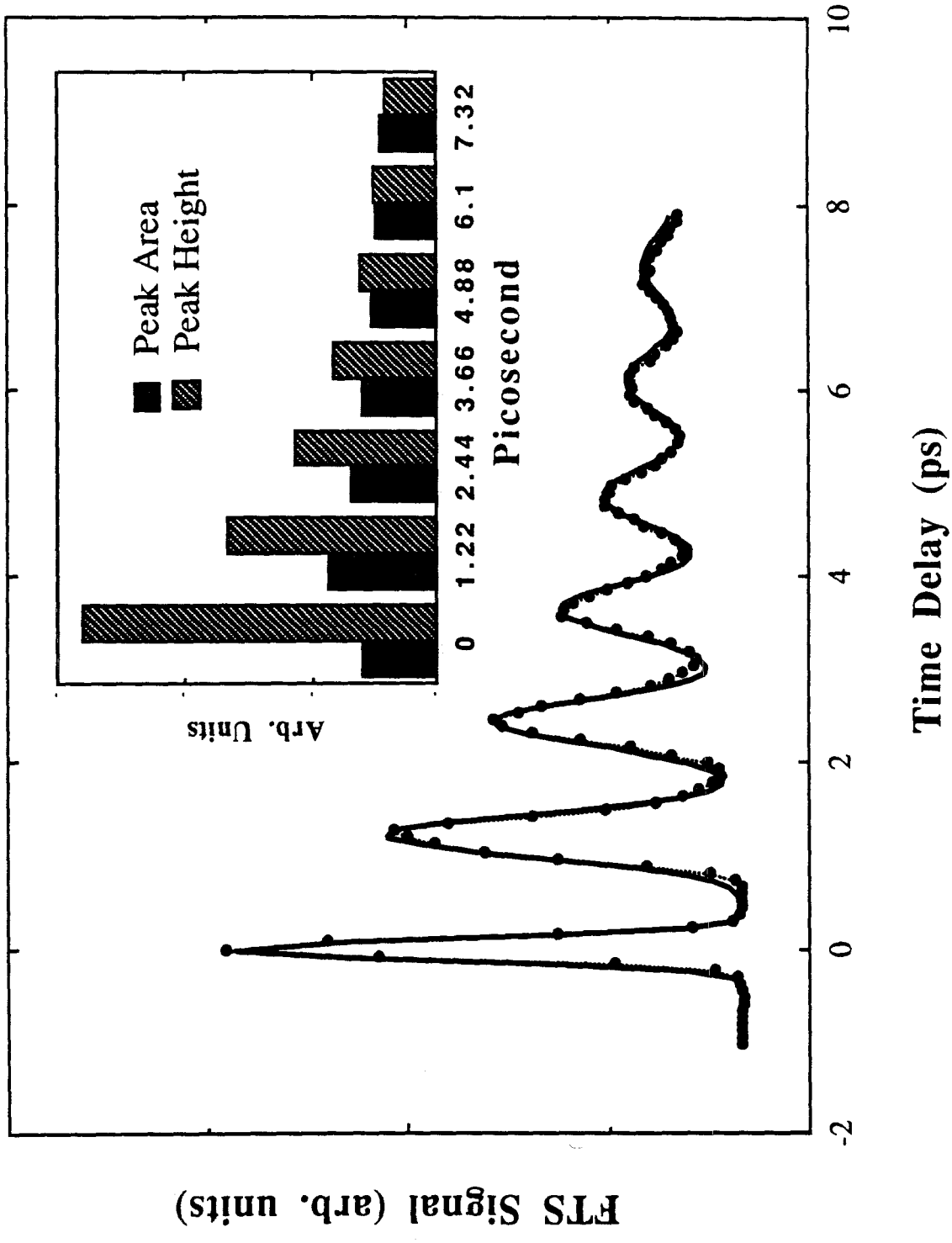
FTS Signal (arb. units)
-2
0
2
4
6
8
10
Time Delay (ps)
Arb. Units
Peak Area
Peak Height
0
1.22
2.44
3.66
4.88
6.1
7.32
Picosecond

Figure 3.5

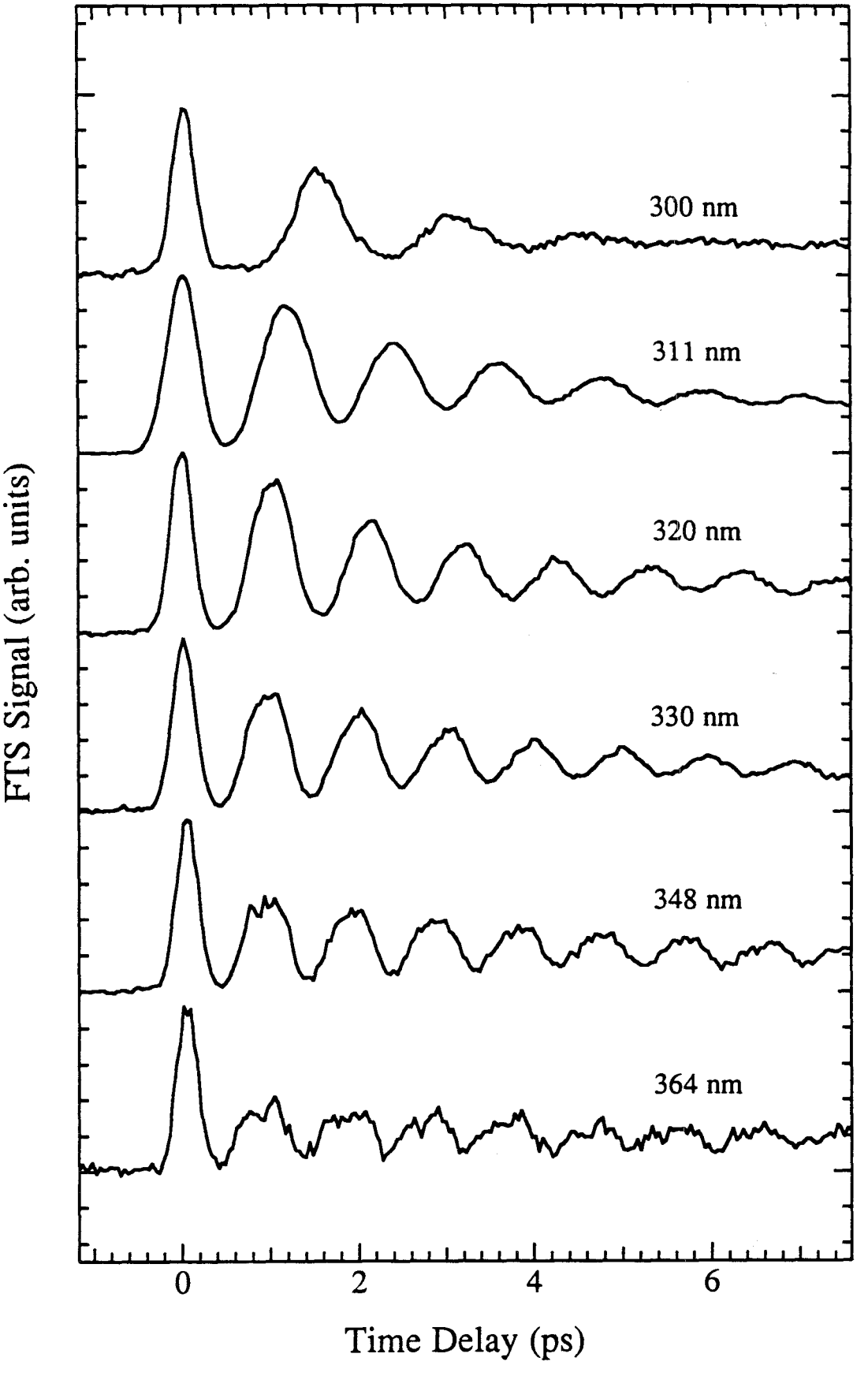
300 nm
311 nm
320 nm
330 nm
348 nm
364 nm
FTS Signal (arb. units)
0
2
4
6
Time Delay (ps)

Figure 3.6

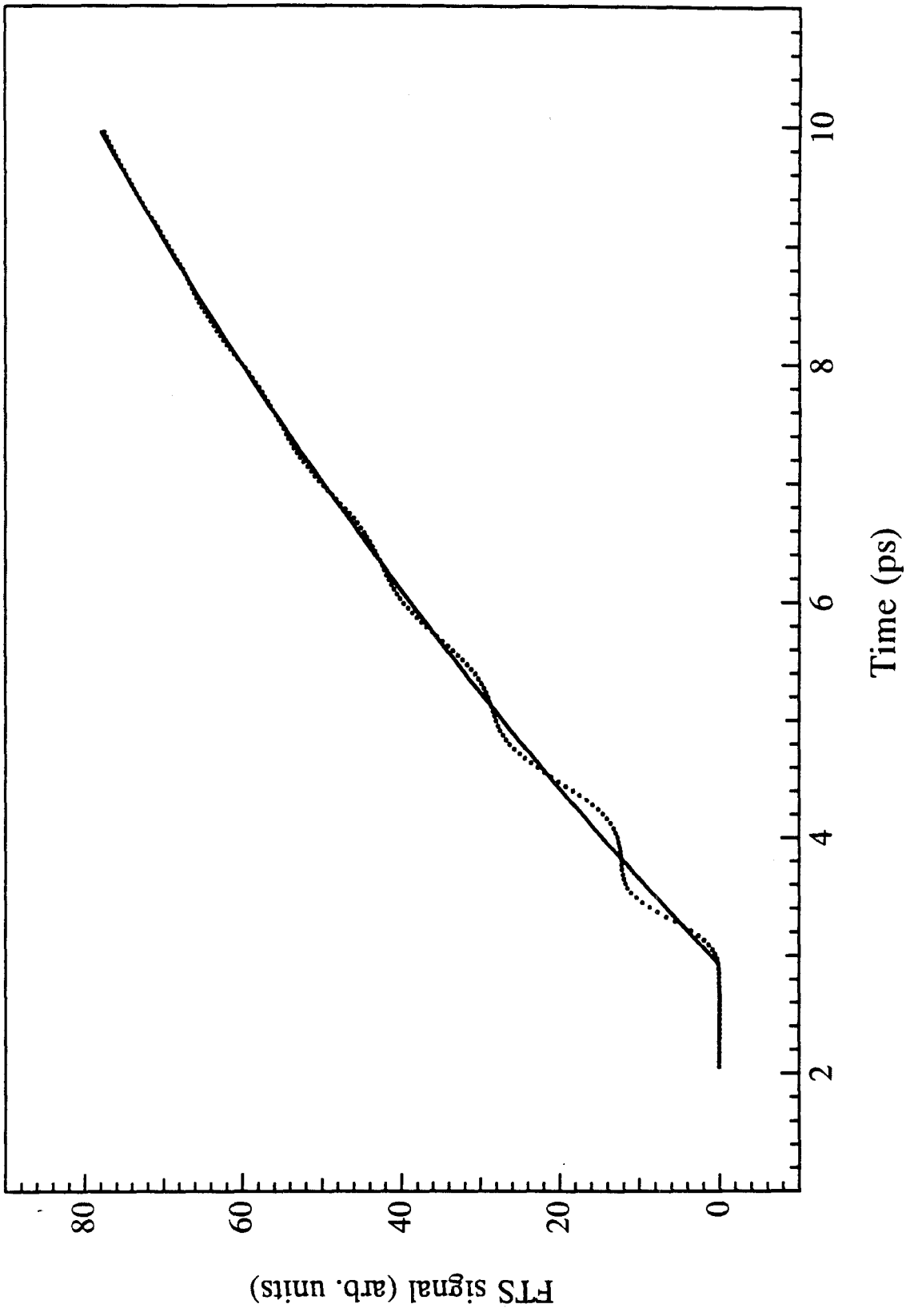

Figure 3.7

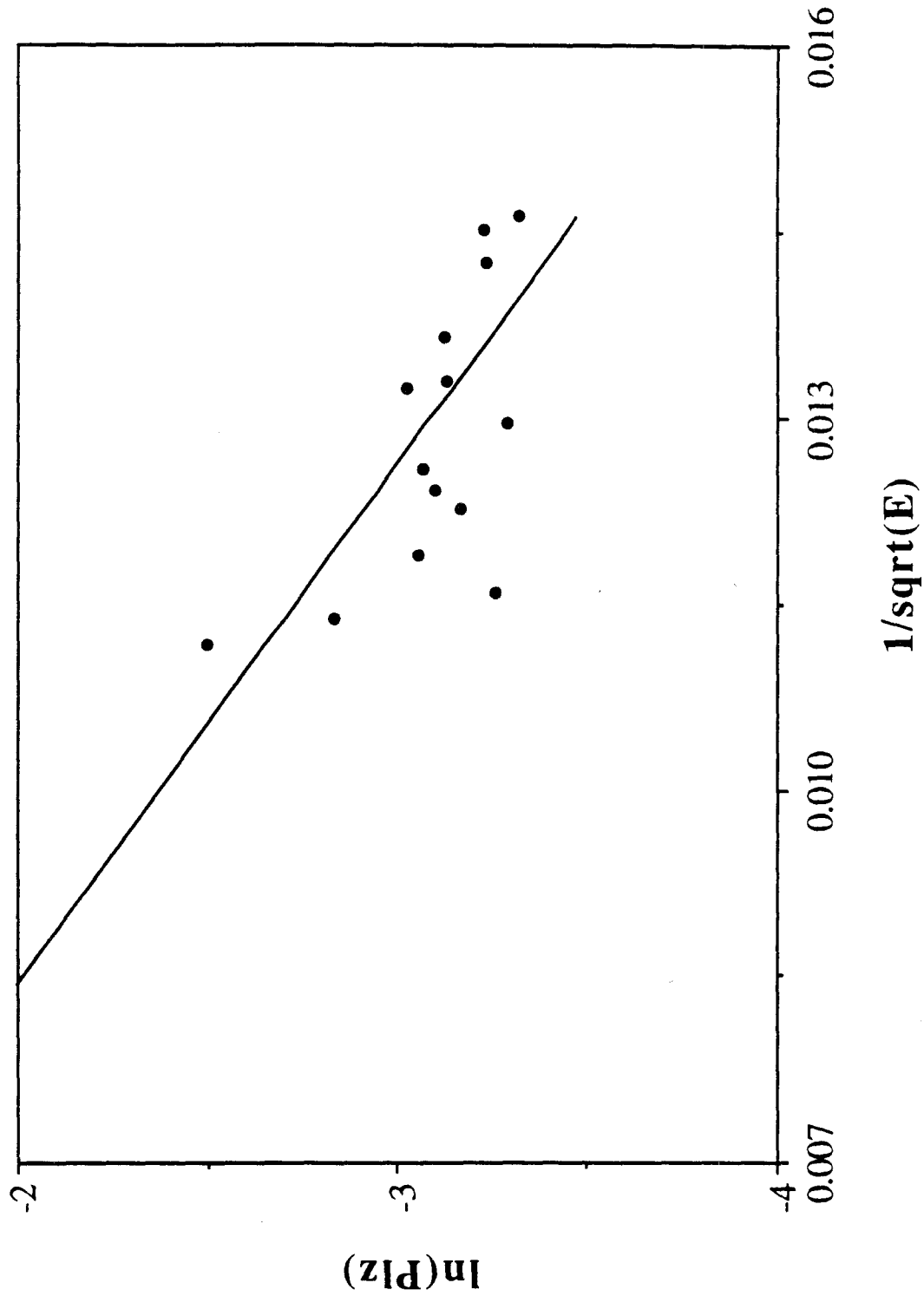

Figure 3.8

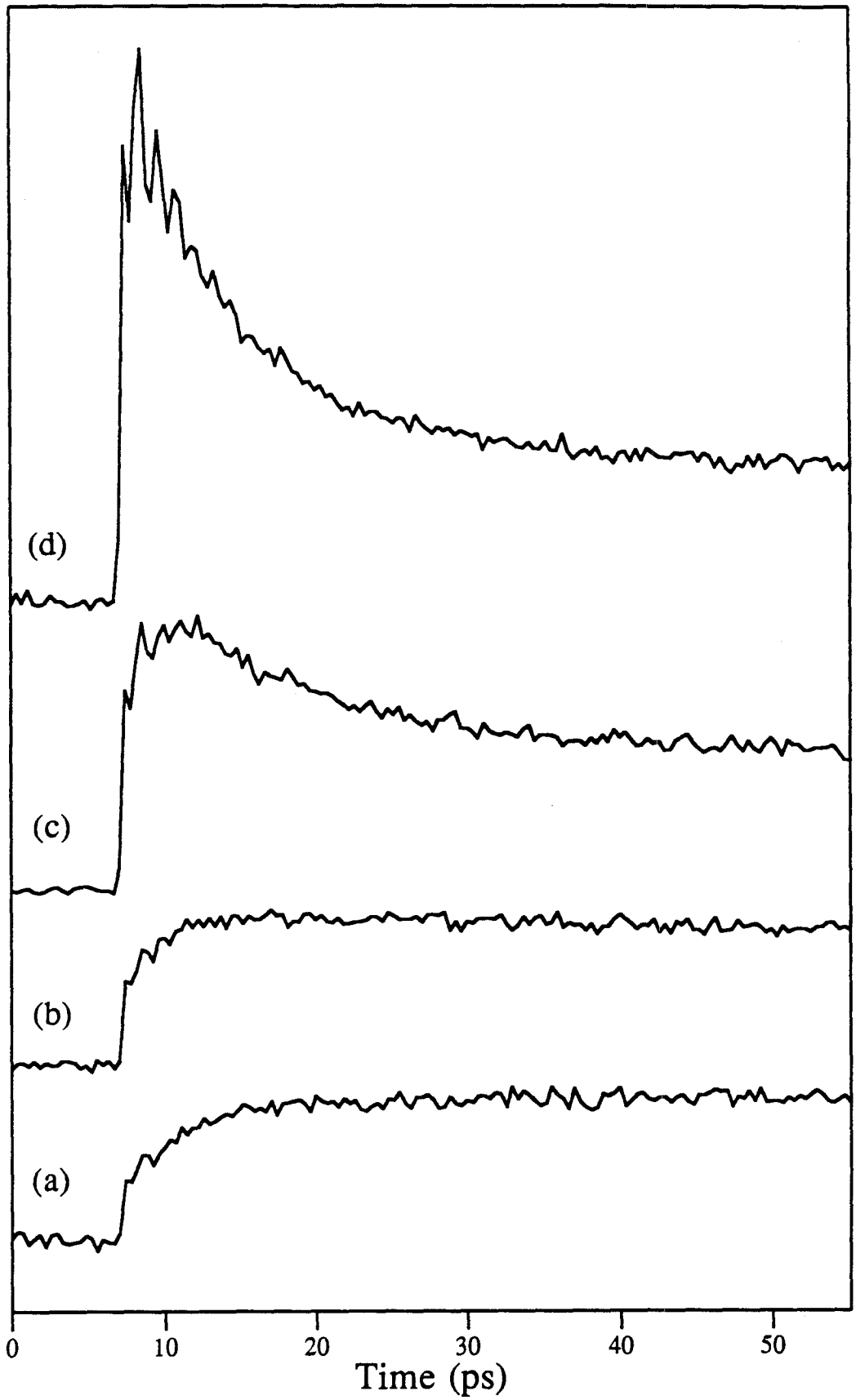

Figure 3.9

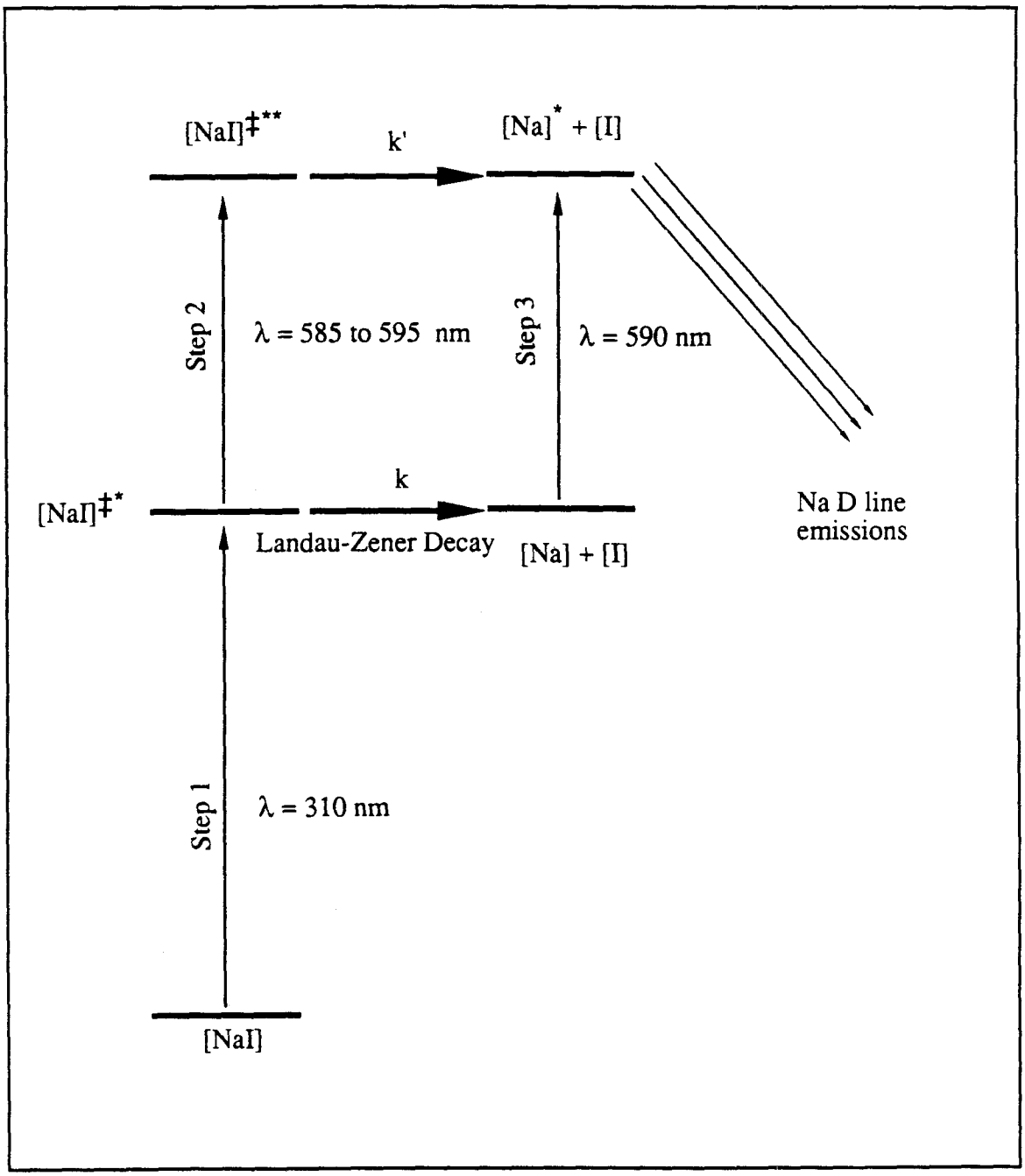
[NaI]‡**
k'
[Na]* + [I]
Step 2
λ = 585 to 595 nm
Step 3
λ = 590 nm
[NaI]‡*
k
Landau-Zener Decay
[Na] + [I]
Na D line
emissions
Step 1
λ = 310 nm
[NaI]

Figure 3.10

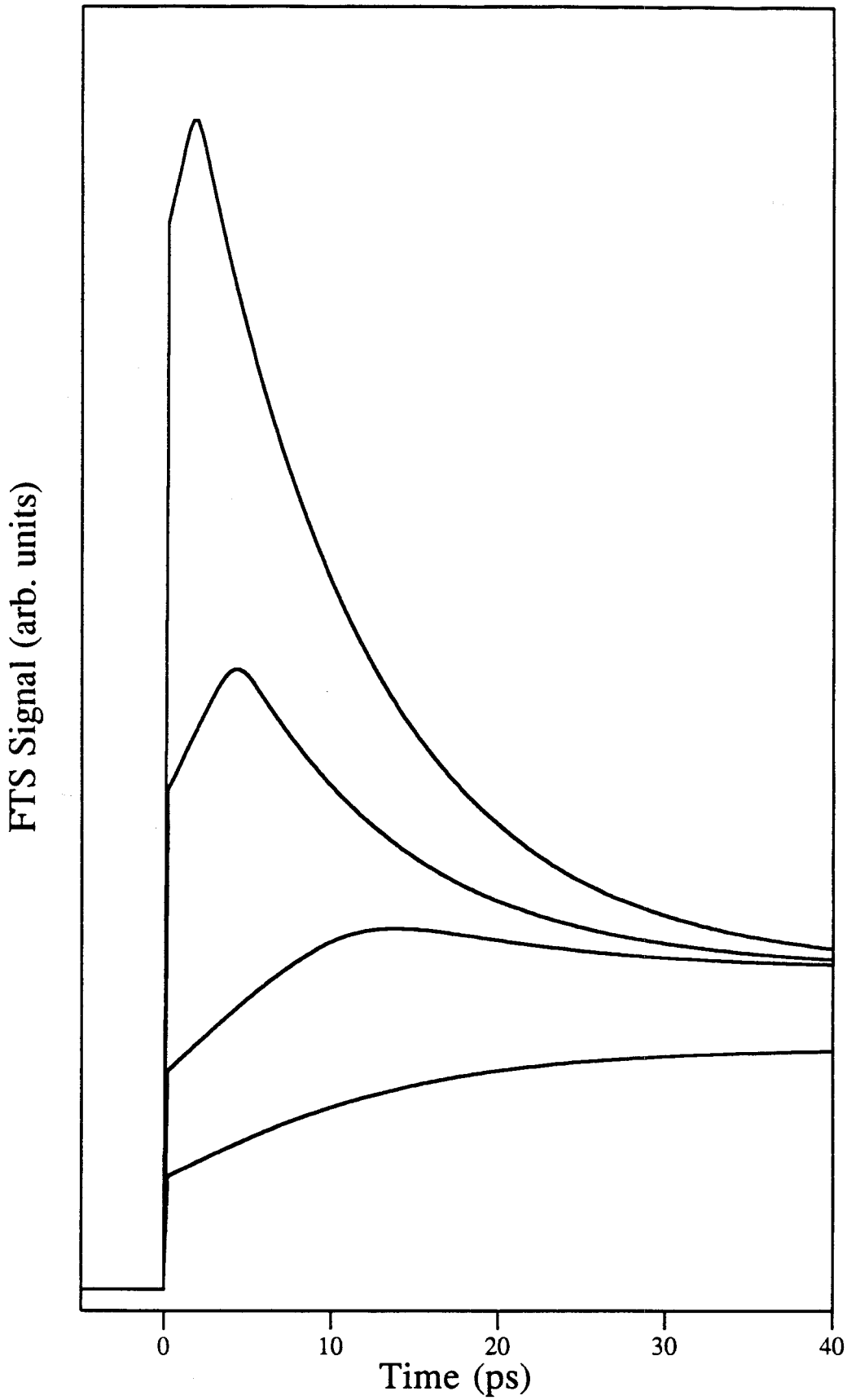

Figure 3.11

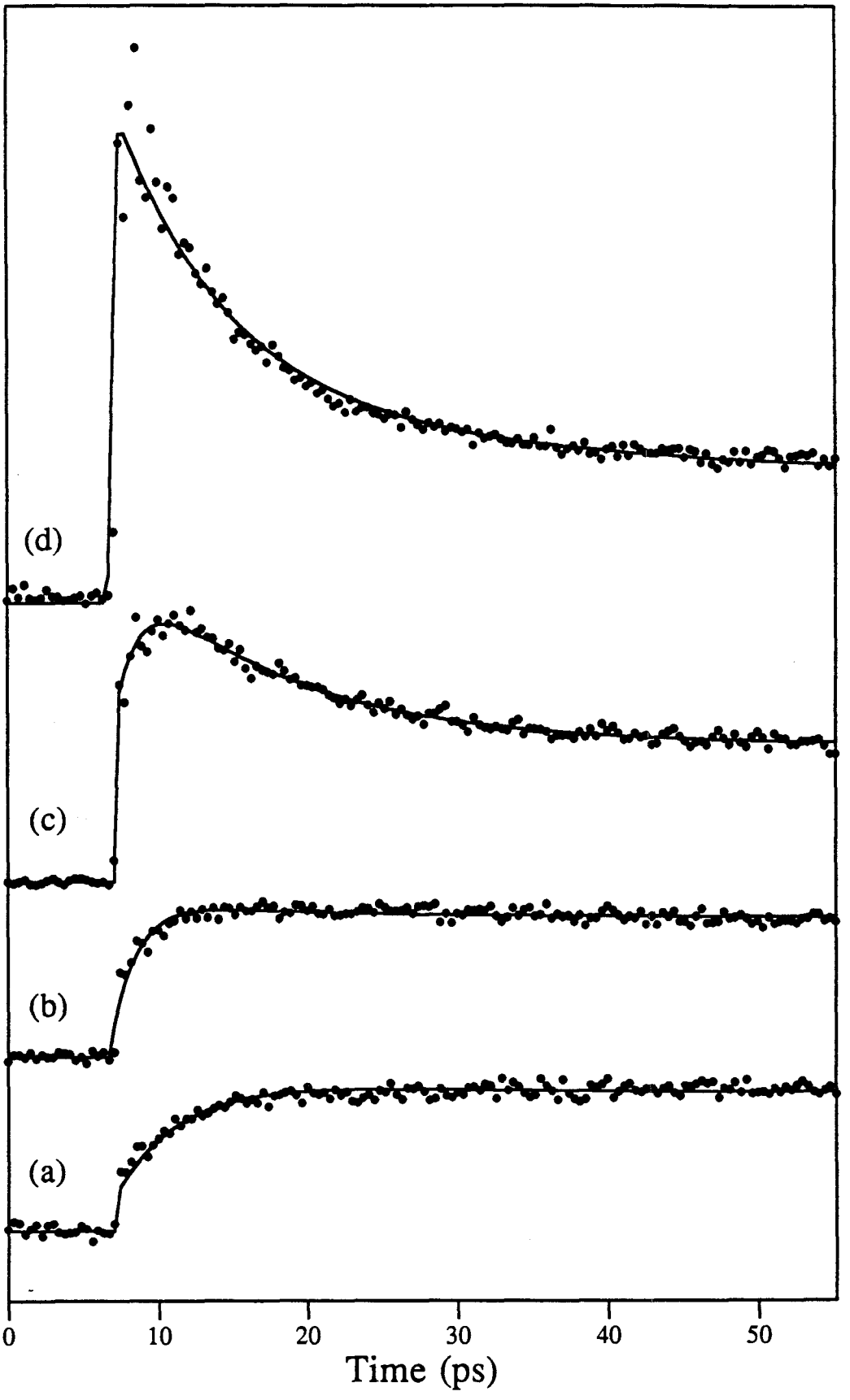

Figure 3.12

Chapter 4

Femtosecond Trajectory Mapping of NaI Predissociation and Direct Inversion to the Potentials

I. Introduction

The fate of a chemical reaction is determined by the potential-energy surfaces (PES's) involved. Given a set of PES's, the dynamical features of a chemical reaction can be computed by either quantum mechanics or classical trajectory methods; the outcome of such calculations is normally dictated by the accuracy of the PES's available, not the computational technique itself. Therefore, obtaining reliable information about the potential-energy surfaces in prototype molecular systems has been the focus for many research activities in chemical dynamics.

In this chapter, a set of experiments is described in which the trajectories of the nuclear motion in the predissociation of NaI are directly mapped out. An inversion procedure is then developed to derive the potential-energy surfaces involved in the photodissociation from these trajectory mapping results. These low-lying potential energy surfaces of sodium iodide have been the object of considerable investigation in the frequency domain.[1-3] The fragmentary band structure of the ultraviolet spectrum of NaI arising from transitions between the ionic ground state $X\ ^1\Sigma_0^+$ and lowest-lying covalent states is attributed to the non-zero interaction-matrix elements that couple $X\ ^1\Sigma_0^+$ and the predissociating $\Omega = 0$ ($A\ 0^+$) state. In the diabatic representation, both $\Omega = 0$ and 1 covalent states correlate asymptotically with neutral $Na(^2S_{1/2}) + I(^2P_{3/2})$ atoms. As a result of non-adiabatic coupling with the ground state, however, the adiabatic PES for the $A\ 0^+$ state is strongly bound relative to separated $Na^+(^1S_0) + I^-(^1S_0)$ ions. The PES of the $\Omega = 1$ covalent state is essentially dissociative at all internuclear separations, with only weak non-adiabatic coupling to the ground-state surface.

van Veen *et al.* have differentiated between absorption from the ground state to each

of the two covalent states by photofragment spectroscopy.[2] Using the Franck-Condon reflection method to determine the fraction of parallel and perpendicular transitions contributing to the total absorption cross section, these workers utilized their data to derive expressions for the inner repulsive limbs of the $\Omega = 0$ and 1 covalent potentials. In a high-resolution laser spectroscopic study, Schaefer, Bender and Tiemann[3] assigned ultraviolet absorption bands of the NaI spectrum across the wavelength range 301 - 372 nm with the aid of (an early version of) Child's semiclassical curve-crossing theory;[4] from their assignments, molecular parameters and RKR turning points for both diabatic $X\ ^1\Sigma_0^+$ and adiabatic A 0^+ bound states were determined.[3] These spectroscopic data[3] have been subject to re-analysis by Wang *et al.*,[5] who cast potential functions for the same states in analytical form using a numerical optimization procedure, and by Chapman and Child,[6] who have derived adiabatic RKR potentials from a semiclassical calculation of predissociating vibration-rotation levels. The potential energy curve for the A 0^+ state has been recently re-examined by Bluhm and Tiemann using optical-optical double resonance (OODR) spectroscopy.[7] Parameterized expressions for the diabatic potential curves of the $X\ ^1\Sigma_0^+$ and A 0^+ states have been given by several authors.[8-10]

Of the large number of higher-lying molecular states that correlate with $I(^2P_{3/2})$ and the electronically excited $Na(^2P_J, J = 1/2, 3/2)$ atom, Polanyi and coworkers[11] were the first to identify the existence of a bound covalent state from an analysis of the far-wing emission of predissociating NaI in the frequency domain. Subsequently, Bluhm *et al.* established the potential minimum of the C 0^+ state to lie some 1423 cm^{-1} below the dissociation limit from laser-excitation spectra.[12]

Femtosecond transition-state spectroscopy (FTS) has been applied to study the predissociation dynamics of NaI in the first manifold of excited states in the time-resolved

mode[13-16]:

$$NaI(X^1\Sigma_0^+) \rightarrow [Na\cdots I]^{\ddagger *}(\Omega = 0, 1) \rightarrow Na(^2S_{1/2}) + I(^2P_{3/2}), \qquad (4.1)$$

Resonant wave-packet trapping that is due to the conical intersection between the A 0^+ and $X^1\Sigma_0^+$ states was observed in the time domain. In that work, the frequency ν_{osc} of wave-packet oscillations within the A 0^+ adiabatic well was carefully measured as a function of the available energy E_{av} above the dissociation limit,[13,14] and was found to be in general agreement with frequency-domain work.[3] However, to perform an inversion of the time-domain data to the form of the reactive potential-energy curve more information is required, since measurements of ν_{osc} as a function of the excess energy E_{av} coupled with application of an RKR (or similar) procedure permit only the separation $\Delta r(E_{av})$ between outer and inner turning points of the potential curve to be obtained. In order to determine the location of the potential in configuration space, it is of course necessary to know the average interfragment separation r as a function of E_{av}, which is usually accomplished by measurement of the rotational constant $B(E_{av})$ of the molecule. Because of the short lifetime of $[Na\cdots I]^{\ddagger *}$ transition states within the A 0^+ adiabatic well (~ 10 ps, see Chapter 3), however, it is not feasible in this case to determine $B(E_{av})$ from measurements of rotational coherence in the time domain, such as have been carried out for I_2 ($B\ ^3\Pi_{0+u}$)[17] and large aromatic species,[18] for example. Instead, the energy-dependence of r is ascertained from measurements of the vibrational period $\tau_{osc} = 1/\nu_{osc}$ together with clocking of the wave-packet motion as it propagates with time to longer r from the inner repulsive wall of the A 0^+ state. To undertake such measurements on NaI predissociation, a set of timing experiments were performed, analogous in principle to those carried out for the direct dissociation of ICN over a repulsive PES.[19] In addition, a simpler method of clocking the reaction emerged during the course of these experiments, which takes advantage of the

ability of FTS to probe the direction of motion of the $[Na\cdots I]^{\ddagger *}$ wave packet prepared on the bound A 0^+ state.[16]

Figure 4.1 shows adiabatic potential-energy curves relevant to the study of predissociation of NaI via the A 0^+ state by FTS. Potentials for the ground electronic state $E_1(r)$ ($X\ ^1\Sigma_0^+$) and bound excited state $E_2(r)$ (A 0^+), formed by mixing of the diabatic potentials $V_2(r)$ and $V_1(r)$ were obtained from the standard expression[20]:

$$E_{1,2}(r) = 1/2\{V_2(r) + V_1(r) \pm [(V_1(r) - V_2(r))^2 + 4V_{12}(r)^2]^{1/2}\}. \qquad (4.2)$$

For the diabatic ionic curve $V_2(r)$ and coupling matrix element $V_{12}(r)$, the parameterized forms put forward by Faist and Levine[9] are employed. The repulsive covalent state $V_1(r)$ was taken to be an exponential function of r, characterized by the parameters derived in this work from an analysis of the experimental clocking data. Similarly, the anharmonic form of $E_3(r)$ determined herein was used to describe the highest-lying electronic state populated by the probe laser. Represented by vertical transitions are the laser excitation processes that constitute the essence of the FTS technique. An ultrashort pump pulse at wavelength λ_1 promotes an ensemble of ground-state molecules to the predissociative potential $E_2(r)$, where a wave packet comprising a coherent superposition of eigenstates is prepared that is initially localized close to the inner turning point. A second ultrashort laser pulse at wavelength λ_2 probes the time evolution of the wave packet as it samples different spatial coordinates on $E_2(r)$ by further exciting the system to the potential $E_3(r)$. The final wave packet formed on $E_3(r)$ is monitored as function of pump-probe time delay τ by emission of atomic resonance fluorescence via the unresolved Na ($^2P_J \rightarrow {}^2S_{1/2}$, J =1/2, 3/2) D-line transitions. Laser pulses with temporal durations of the order of $\leq$ 100 fs ensure adequate time resolution of the nuclear dynamics, yet are longer than the timescale for electronic

dephasing (given by the inverse of the absorption linewidth).

In Section II of this chapter the experimental results are presented, while the method of inverting the time-resolved data to obtain the excited-state potential functions involved in probing the photodissociation process by FTS is outlined and applied in Section III. Potential-energy curves derived from the new inversion procedure are compared with those obtained from previously published investigations of the low-lying NaI states. Finally, complementary quantum dynamical calculations of the behavior of $[Na\cdots I]^{\ddagger *}$ transition states at short times following initial excitation to the A 0^+ state are reported in Section IV, which serve to confirm the general validity of the potential-inversion procedure. Section V comprises brief concluding remarks.

II. Experimental Results

The experimental methodology of FTS, as applied to the study of alkali halide dissociation reactions, has been presented in detail elsewhere[14] (see also the previous chapter). Therefore, only a brief outline of the procedure adopted here is given, with most attention focused on specific details pertinent to the current experiments.

Femtosecond laser pulses (FWHM ≈ 100 fs) were generated in a colliding-pulse mode-locked ring dye laser (CPM) at a wavelength of about λ = 620 nm and were further amplified by a four-stage pulsed dye-laser amplifier pumped by a 20 Hz Q-switched frequency-doubled Nd:YAG laser. Tunable probe pulses (λ_2 = 590 - 700 nm) were obtained by focusing part of the amplified CPM output into a D_2O cell to generate a white-light continuum, which was frequency-selected by an interference filter. Tunable pump pulses (λ_1 = 320 - 365 nm) were obtained by further amplifying a portion of the continuum by the residual 532 nm light from the same Nd:YAG laser and frequency-upconverted by second-harmonic generation in a KD*P crystal; pump pulses at λ_1 = 391 nm were

obtained by sum-frequency generation through mixing the amplified CPM radiation (λ = 623 nm) and the fundamental beam of the Nd:YAG laser at λ = 1064 nm.

Pump and probe pulses were delayed in time relative to one another by means of a high-precision Michelson interferometer. The two beams were then collinearly recombined by a dichroic beam splitter and focused into a sealed quartz cell of length 8 cm containing ≈100 mTorr of NaI when heated to about 650 °C.[14] As a function of pump-probe delay time, laser-induced fluorescence (LIF) was collected perpendicular to the incident pump and probe light. The LIF was dispersed through a 0.34 m monochromator tuned to the unresolved D-line emission of atomic Na at λ = 589 nm, and detected with a photomultiplier tube.

A set of timing experiments were carried out to determine the time duration τ_0 between initial preparation of the wave packet on the covalent A 0^+ potential and its subsequent detection by the probing laser pulse, as revealed by a maximum in intensity of the FTS signal. τ_0 was systematically measured in this way for a fixed-pump wavelength of λ_1 = 310 nm and probe wavelengths in the range λ_2 = 600 - 700 nm. Figure 4.2 presents a schematic illustration of the experimental arrangement adopted to obtain such data, while results are listed in Table 4.1. For these measurements an exact zero-of-time, *i.e.*, the delay time at which the pump and probe pulses were temporally synchronous, was required. This was obtained by taking the temporal difference between the first peak of the transient signal (obtained at off-resonance probe wavelengths) and the cross-correlation signal between the pump and probe beams, minus the dispersion between pump and probe pulses introduced by the quartz window of the vapor cell. The uncertainty associated with measurements of time zero was estimated to be ± 20 fs.

A direct and rather simple method of measuring the same time difference τ_0 makes use of the splitting of the observed intensity maxima at low pump frequencies. For these

experiments, "high-resolution" data were obtained by numerically averaging 20 to 100 data scans so as to facilitate a thorough examination of the transient lineshapes. As shown in Figure 4.3, for a fixed-probe wavelength of $\lambda_2 = 605$ nm, the second and subsequent peaks of the FTS transients become increasingly broad as the energy E_{av} available to the oscillating wave packet is decreased, splitting into two distinct peaks for pump wavelengths $\lambda_1 \geq 330$ nm. Similar behavior is depicted in Figure 4.4, which shows the effect of tuning the probe wavelength from red to blue wavelengths approaching $\lambda_2 = 589$ nm at a constant photolysis wavelength of $\lambda_1 = 391$ nm.

In order to analyze quantitatively the splitting data, the observed transients were fitted to a sum of Gaussians by a non-linear least-squares fitting routine (see, for example, Figure 4.5). First, an intuitive physical picture is presented by which these general trends can be readily understood. Figure 4.5 defines the splitting time τ_s as the difference between the two doublets of the second (and subsequent) maxima of the FTS signal. (Also shown is the oscillation period τ_{osc}, which can be inferred from fitting of the experimental splitting data.) The wave packet is initially promoted from the ground electronic state $X\ ^1\Sigma_0^+$ to the inner repulsive branch of the adiabatic potential $E_2(r)$, where it proceeds to propagate towards larger r. A time τ_0 later, the wave packet reaches the center of the optically-coupled region (or detection "window") projected onto the reactive potential by the probe pulse at a distance r_2. At this position, λ_2 is in resonance with the energy separation between the A 0^+ and higher-lying fluorescent states, resulting in the appearance of the first peak in each of the FTS transients. As time proceeds, the wave packet continues to propagate towards longer r until it reaches the outer turning point r_{out} of the attractive branch of $E_2(r)$; at the distance r_x (where $r_2 < r_x < r_{out}$) a fraction of the original population is lost via the partial avoided crossing to the exit channel leading to $Na(^2S_{1/2}) + I(^2P_{3/2})$ atoms. At r_{out} the wave packet is reflected to shorter r, re-entering the optically coupled region once again, and giving rise to the leading (earlier) maximum of the doublet structure that follows the initial

peak in the FTS signal. The later-time maximum of the doublet arises from passage of the wavefunction towards longer r as the $[Na\cdots I]^{\ddagger *}$ transition-state undertakes its second round trip within the A 0^+ adiabatic well. If the excess energy E_{av} is large, then the group velocity of the wave packet is sufficiently great so as to render the spacing between the two maxima of the doublet unresolvable with probe-pulse widths of the order of 100 fs. However, at lower excess energies, where the group velocity of the wave packet is slower, the peak-to-peak spacing is large enough to result in splitting of the second-intensity maximum into a doublet structure as illustrated in Figure 4.3. By the same reasoning, tuning the probe laser to shorter wavelengths is equivalent to shifting the detection window to larger internuclear separations, therefore creating sufficient temporal spacing to resolve the bidirectionality of the wave packet motion.

The splitting time τ_s of the transient peaks therefore constitutes a direct measurement of the round-trip time for the wave packet trapped within the A 0^+ adiabatic well to propagate from the probe window to the inner turning point of the potential and return to the probe window again, *i.e.*, $2\tau_0$. Values of τ_s determined from the splitting measurements are presented in Table 4.2, while the oscillation periods τ_{osc} are given in Table 4.3.

III. Inversion to the Potential Energy Curves

In this section, the experimental data presented in Section II are employed to obtain the potential-energy curves relevant to measurements of NaI photodissociation by FTS, namely, those for the intermediate A 0^+ state ($E_2(r)$) and fluorescing state ($E_3(r)$) displayed in Figure 4.1. The method of the potential inversion is based on classical trajectory calculations and makes use of the phenomenological description of photodissociation processes in real time put forward by Bersohn and Zewail.[21]

Before the classical inversion procedure itself is described, however, the validity of the classical description in representing the motion of $[Na\cdots I]^{\ddagger *}$ wave packets within the A 0^+ adiabatic well is established. Generally, the classical approximation is good if the following two conditions are satisfied[22]: The mean values of physical quantities such as average position and velocity follow closely the law of classical mechanics; and the dimensions of the wave packet are small compared to the characteristic dimensions of the problem and remain so during the concerned course of time. In the case of NaI excited by a coherent laser pulse 100 fs in duration, the second condition is satisfied within the first few periods of vibrational oscillation, when the spread of the wave packet is not significant.[15] In order to verify the first condition, both quantum and classical trajectories have been calculated and compared at an excitation wavelength of λ_1 = 350 nm. Using the potential functions cited by Rose *et al.*,[14] the agreement between quantum and classical values of the mean position of the promoted wave packet in the A 0^+ state is found to be excellent except in the region close to the inner turning point on the repulsive wall, where the classical trajectory penetrates to shorter distances by some 0.2 Å (see figure 4.6). It may be concluded therefore that the classical approximation provides an adequate description of the transition-state dynamics within the first 3 ps following initial excitation of the wave packet to the excited A 0^+ state.

In Sub-Sections III.1 - III.3 following, the repulsive limb of the A 0^+ potential is first determined, followed by inversion to the complete adiabatic potential-energy curve. From the A 0^+ potential so derived and the values of τ_s listed in Table 4.1, the potential function for the high-lying state that correlates with $Na(^2P_J) + I(^2P_{3/2})$ atoms is then obtained.

III.1 The Repulsive Branch of $E_2(r)$

The repulsive branch of the A 0^+ potential has been studied by several research groups employing different techniques.[2,8,9] An exponential form for the repulsive diabatic component $V_2(r)$ of the adiabatic potential $E_2(r)$ given by:

$$V_2(r) = A \cdot exp[-\alpha(r-r_0)] \qquad (4.3)$$

has been proposed by van Veen *et al.*, with parameters A, α and r_0 deduced from the results of the photofragmentation spectroscopic study carried out by these authors.[2] Although it fails to include a term for long-range van der Waals attraction, the main features of the absorption spectrum of NaI can be adequately accounted for by Equation (4.3). For this reason, an exponential representation of the diabatic $V_2(r)$ potential has been widely adopted in the literature, including recent time-dependent quantum-dynamical[23] and classical[4,16,24] simulations of reaction (4.1).

In this chapter, Equation (4.3) for the repulsive branch of the A 0^+ potential is employed with A, α and r_0 to be determined from the inversion procedure. In order to minimize the number of variable parameters, however, values of A and r_0 are fixed at 0.813 eV and 2.7 Å, respectively,[2,3,14] leaving only the inverse-length parameter α to float. The dissociation energy D_e of this repulsive curve is chosen to be 3.15 eV, an average of recent literature values.[2,3,25] The justification for fixing A, r_0 and D_e is that these quantities have been determined fairly accurately from existing spectroscopic techniques.[2,3] For example, A and r_0 are determined largely by the location of the absorption maximum. α, on the other hand, which reflects the steepness of the repulsive wall, is determined by the width of the absorption peak profile; owing to hot-band contributions to the absorption spectrum, it is a much less accurately known parameter. The effect of including a $-C_6/r^6$ term in Equation (4.3) has also been investigated, and it is found (as expected) that a shallow van der Waals well of depth 323 cm^{-1} located at r = 4.17

Å does not affect the timing of wave-packet motion on the A 0^+ potential within experimental uncertainty.

For the ionic ground state X $^1\Sigma_0^+$, the diabatic Rittner-type potential first suggested by Faist and Levine[9] is employed, since it has a simple analytical form and has been widely adopted in the literature by other authors. It is noted, however, that this form deviates slightly from the RKR turning point data for the X $^1\Sigma_0^+$ state given by Tiemann and coworkers.[3] In order to test the robustness of the $E_2(r)$ potential derived from FTS experiments to the choice of ground-state potential, the inversion procedure outlined below has also been applied using the potential function determined from spectroscopic measurements in the frequency domain.[3] In this case, the value of α so derived is slightly smaller than that obtained, assuming a Rittner-type potential for the $X^1\Sigma_0^+$ state (see later).

To determine the time evolution of a single classical trajectory over an exponentially repulsive potential, the approach put forward by Bersohn and Zewail[21] is invoked. For a particle whose initial coordinate is r_1 (determined by the pump-laser pulse) at time $t = 0$, the time taken to reach the position r_2 (*i.e.*, the center of the probe window), is given by the equation:

$$t = \frac{1}{\alpha v} \cdot ln \left\{ \frac{1 + \sqrt{1 - exp(-\alpha \Delta r)}}{1 - \sqrt{1 - exp(-\alpha \Delta r)}} \right\}, \qquad (4.4)$$

where $\Delta r = r_2 - r_1$ and $v = (2E_{av}/\mu)^{1/2}$ is the terminal recoil velocity of a particle of reduced mass μ in the center-of-mass frame. In the limit that $\alpha\Delta r >> 1$, this expression can be further simplified to:

$$t = \frac{\Delta r}{v} + \frac{1}{\alpha v} \cdot ln4, \qquad (4.4')$$

so that after a time τ the system will arrive at the position r_2 given by:

$$r_2 = r_1 + vt - [ln(4)/\alpha]. \qquad (4.5)$$

In the femtosecond pump-probe experiment on NaI, a coherent wave packet is prepared by the pump pulse at $r_1(\lambda_1)$ on the repulsive wall, which then oscillates within the A 0^+-state potential well. The time taken for the wave packet to reach the optically coupled region centered about the internuclear separation $r_2(\lambda_2)$ depends on $r_1(\lambda_1)$, $r_2(\lambda_2)$ and the shape of the potential $E_2(r)$ between these two points. If $r_2(\lambda_2)$ is kept constant and $r_1(\lambda_1)$ is varied over a range of values, then it is possible to sample different points on the repulsive branch and gain specific information about its shape by measuring the time required to reach the probe window as a function of the pump wavelength λ_1.

We now focus attention on one set of splitting data, namely, that obtained at a fixed probe laser wavelength of λ_2 = 605 nm. The pump wavelength was varied from λ_1 = 310 - 391 nm, and the splitting time τ_s deduced at each wavelength. As pointed out in Section II, half of the splitting time corresponds to the propagation time of the wave packet between $r_1(\lambda_1)$ and $r_2(\lambda_2)$. For any given pump wavelength, $r_1(\lambda_1)$ can be determined for a given a value, as can the available energy E_{av}. If a classical trajectory is propagated from an initial coordinate $r_1(\lambda_1)$ and allowed to evolve for half of the splitting time, it will reach a certain position, which is designated as $r'_2(\lambda_1;\alpha)$. The procedure is then repeated for all the other pump wavelengths λ_1, thereby generating a set of $r'_2(\lambda_1;\alpha)$ values. If the value of α is properly chosen, the deviation of each $r'_2(\lambda_1;\alpha)$ should be very small for different values of $r_1(\lambda_1)$, because all the $r'_2(\lambda_1;\alpha)$ values so derived correspond to the same central

position $r_2(\lambda_2)$ of the detection window defined by the spectral bandwidth of the probe laser at λ_2 = 605 nm. In this way, the optimal value of α is determined to be 2.5 $Å^{-1}$, using the analytical form of the ground-state potential presented by Faist and Levine,[9] smaller than the result α = 4.088 $Å^{-1}$ derived from photofragmentation spectroscopy[2] but consistent with other literature values[8,9] (see Table 4.4 for a listing of the results from this inversion and Figure 4.7 for a comparison of the trajectories from different α's).

The result α = 2.5 $Å^{-1}$ obtained for λ_2 = 605 nm also gives good overall agreement with two other sets of splitting data obtained at probe wavelengths λ_2 = 620 and 640 nm. Using Equation (6) together with the value of a determined above and the τ_s data listed in Table 4.1, it is then possible to deduce r_2(605 nm) ≈ 6.5 Å, r_2(620 nm) ≈ 5.6 Å and r_2(640 nm) ≈ 5.0 Å for $r_2(\lambda_2)$ at each of these three probe laser wavelengths. These data will prove to be crucial in determining the shape of the C 0^+ potential-energy curve (see later).

As has been noted at the beginning of this subsection, the Rittner-type ground ionic-state potential surface for NaI as first suggested by Faist and Levine[9] deviates slightly from the potential obtained by spectroscopic data via an RKR inversion procedure.[3] A "close-up" look of these two ground state PES's is shown in Figure 4.8; also shown in this figure is an analytical form of the PES obtained by a numerical optimization procedure, based on the RKR points provided by Schaefer *et al.*[3] Even though the differences among all the potentials are rather minor on a global scale (see figure 2.4), there is significant disagreement near the minimum of the potential. For example, the minimum of the Faist-Levine potential is located at 2.67 Å, while the experimental value is at 2.71 Å; the fundamental vibrational frequency is predicted by the Faist-Levine potential to be 280 cm^{-1}, *vs.* 260 cm^{-1}, the experimental value. The numerically optimized potential deviates from the RKR points significantly too, especially on the inner limb of the potential.

To explore the effects of the different ground-state potentials on the inverted potential and thereby to test the robustness of the inversion procedure, the RKR points are fitted to a Morse potential for the first 5000 cm^{-1} with a non-linear least-squares fitting routine, then this Morse potential is used as the ground-state potential, the starting point for the inversion. The dissociation energy of 25556 cm^{-1} is adapted from Schaefer *et al.*[3] to determine the excess energy, in conjuction with the Morse potential. The results from such inversions are summarized in Table 4.5. As can be seen from this table, the results are identical with those obtained from the Faist-Levine ground-state potential within our experimental uncertaintities.

The central point in the inversion procedures is the determination of excess energy at a given pump wavelength. For the inversions carried out so far, the excess energy is calculated by finding an internuclear separation where the difference between the ground-state potential (either the Rittner-type or the Morse-type) and a trial upper potential is matched to the pump wavelength, and then the excess energy is determined by the amount of energy the trial upper curve has above the dissociation limit at this particular internuclear distance. This is equivalent to finding the location for the maximum Franck-Condon factor for the selected pump wavelength. The differences in the vibrational populations of the ground state that are due to Boltzmannn distributions are therefore totally ignored. To remedy this oversimplification, the contribution of Boltzmann and Franck-Condon factors is combined in the following way to determine the excess energy for a given pump wavelength:

$$<E_{excess}(\lambda_{pump})> = \sum_i f(v_i'', \lambda_{pump})B(v_i'')E(v_i'') \Big/ \sum_i f(v_i'', \lambda_{pump})B(v_i''), \qquad (4.6)$$

where $f(v_i'', \lambda_{pump})$ is the Franck-Condon factor for a pump wavelength of λ_{pump} from a ground vibrational state v_i'', while $B(v_i'')$ is the corresponding Boltzmann factor from v_i''

($B(v_i'') = \exp(-E(v_i'')/kT)$). The summation is carried out from i = 0 to i = 19. The Franck-Condon factors are determined by reflecting the ground-state vibrational eigenfunction to the upper trial potential function, *i.e.*, the Condon reflection method; the ground-state vibrational wavefunctions and energies are obtained by solving the one-dimensional Schroedinger equation of the Morse oscillator. The temperature used in the calculations is 650 °C. The results from this semiclassical procedure for a number of trial α values are listed in Table 4.6, which are very close to those shown in Tables 4.4 and 4.5, despite the more realistic and elaborate procedure employed to determine the recoil energy.

One last factor that is considered in the inversion procedure is the effect of rotational energy. At the initial position of the wave packet prepared by the pump pulse, which is close to the equilibrium bond length of ground-state NaI, the rotational energy contained in the wave packet can be expressed as $J(J+1)h^2/8\pi^2\mu r^2$. When the wave packet reaches the optically coupled region, much of the rotational energy has been converted to translational energy, since r has been stretched out quite far. However, the amount of rotational energy released is relatively small compared with the vibrational excess energy. For example, considering a pump wavelength of 360 nm and a median rotational quantum number 50, the maximum amount of rotational energy that can be released is 300 cm^{-1}; it is less than 8% of 3777 cm^{-1}, the vibrational excess energy (Table 4.6, $\alpha = 2.0$). The final velocity with and without this rotational energy will differ by less than 3%, well within the uncertainties of the experimental measurements. Thus, rotational energy is not expected to have much effect on the velocity of the wave packet, where vibrational excess energy is the dominant driving force. However, the thermal distribution of rotational states will induce a distribution of arrival times for wave packets with the same vibrational energy but with different rotational energies to reach the common probe window, therefore broadening peaks in the FTS transients. This effect may be seen by comparing the quantum

dynamically simulated (see Section IV) and experimentally observed transients.

III.2 The Complete $E_2(r)$ (A 0^+) Potential

Having obtained the repulsive branch, the oscillation periods of the $[Na\cdots I]^{\ddagger *}$ vibrations can be used to determine the separation $\Delta r(E_2)$ between inner and outer turning points of the adiabatic well as a function of energy E_{av} above the potential minimum. To this end, the classical inversion method recently presented by Bernstein and Zewail, for inversion of data obtained by Femtosecond Temporal Spectroscopy to a functional form for the controlling potential,[27] is employed.

For a known ground-state potential $V_2(r)$ and the repulsive branch of the A 0^+ state derived in subsection III.1, the excess vibrational energy above the minimum of the A 0^+ potential may be readily determined for a given pump wavelength: The available energy, pump wavelength and corresponding oscillation periods are listed in Table 4.3. Using these eight pairs of values of E_{av} and t_{osc}, the data points were fitted to a third-order polynomial of the form:

$$\Delta r(E_2) = 11.154 \times 10^{-5} \cdot a_0 V^{1/2} [1 + a_0^{-1}(a_1 b_1 V + a_2 b_2 V^2 + a_3 b_3 V^3)], \qquad (4.7)$$

where $a_0 = 909$, $a_1 = -1.1225 \times 10^{-3}$, $a_2 = -2.2019 \times 10^{-6}$, $a_3 = 1.2802 \times 10^{-9}$, $b_1 = 0.6667$, $b_2 = 0.5333$, and $b_3 = 0.4571$. a_0 is expressed in units of femtoseconds and V in cm^{-1}.

From the exponential form for the repulsive branch of the A 0^+ state given by Equation (4.3), it is easy to obtain the equations:

$$r_1(E_2) = r_0 - (1/\alpha) \cdot ln[V_2(r_1)/A], \qquad (4.8)$$

and

$$r_2(E_2) = \Delta r(E_2) + r_1(E_2), \qquad (4.9)$$

which enable a complete adiabatic potential curve $E_2(r)$ to be constructed. Tiemann and coworkers have derived RKR potentials for the A 0^+ state from data obtained by high-resolution absorption spectroscopy[3] and OODR spectroscopy.[7] An analytical form for the same potential has also been provided.[5] A comparison of $E_2(r)$ derived by FTS with the shapes determined by other workers[2,3,5,7] is displayed in Figure 4.9. As can be seen from this figure, the overall degree of agreement between the various potential functions is quite good, except that the repulsive wall of the potential recently constructed from OODR spectroscopic measurements on the A 0^+ state[7] is less steep and shifted to longer internuclear separations (giving rise to a sharper minimum) than those determined by FTS, photofragmentation spectroscopy[2] and a re-analysis[5] of earlier absorption data.[3] At large interfragment distances, agreement is much closer. It is quite remarkable that the 1/r dependence of the outer branch of the $E_2(r)$ potential that is due to Coulomb attraction is recovered by such a simple classical inversion procedure.[27]

III.3 The $E_3(r)$ potential

In subsections III.1 and III.2, the potential-energy curve for the A 0^+ state has been obtained from measurements of the doublet splitting τ_s and oscillation periods τ_{osc}. Given this result, values of τ_s and τ_0 may be further employed to derive the form of the potential function $E_3(r)$ for the fluorescing state accessed by the probe laser.

From the splitting data alone, we know that at 6.5 Å, the potential difference between

the potentials $E_2(r)$ and $E_3(r)$ is 16529 cm^{-1}, corresponding to λ_2 = 605 nm; similarly, at 5.6 and 5.0 Å the potential difference is 16000 cm^{-1} (λ_2 = 625 nm) and 15625 cm^{-1} (λ_2 = 640 nm), respectively. Since the A 0^+ state is known and the asymptotic potential difference (long-r limit) is 16969 cm^{-1} (λ_2 = 589 nm), this gives four points on the higher-lying potential curve that are located on the outer (attractive) branch. From values of τ_0 listed in Table 4.1 for λ_1 = 310 nm, an additional seven points on the upper potential may be determined as follows. The timing data obtained at this pump wavelength are effectively a direct measurement of the difference potential $\Delta E(t)$ (= $E_3(t)$ - $E_2(t)$) expressed as a function of time, conversion of which to $\Delta E(r)$ is readily facilitated by means of the trajectory r(t) resulting from excitation at λ_1 = 310 nm; r(t) itself is computed by the numerical integration method described in subsection III.2. Since $E_2(r)$ is known, $\Delta E(r)$ therefore yields $E_3(r)$ at coordinate positions corresponding to the seven values of τ_0. The total eleven points can then be curve-fitted to the function form of a Morse potential curve:

$$E_3(r) = D_e[1-exp(-(r-r_e)/\rho]^2 - D_e, \qquad (4.10)$$

yielding the results D_e = 1863 ± 210 cm^{-1}, r_e = 3.99 ± 0.08 Å and ρ = 1.18 ± 0.10 Å, where the uncertainties represent 1σ standard errors obtained from the non-linear least-squares fitting routine. Repeating the above procedure for an intermediate $E_2(r)$ potential that includes a long-range van der Waals well some 323 cm^{-1} deep results in a Morse curve for $E_3(r)$ that possesses a minimum some 600 cm^{-1} deeper but with values of r_e and ρ that are the same as those given above within the statistical uncertainty limits.

Polanyi and coworkers[11] have employed an LIF technique to study the emission spectrum of NaI during dissociation when excited to a high-lying state, believed to be C 0^+, with a broadband excitation source.[12] These workers derived parameters for a Morse potential with a dissociation energy D_e = 530 cm^{-1} based on an analysis of the portion of

the emission spectrum originating from bound states on the upper potential. A laser-excitation investigation of the C 0^+ potential in the frequency domain has recently been reported by Tiemann and co-workers.[12] On the basis of RKR inversion of their spectroscopic data, these workers reported a potential minimum of $D_e = 1422.6 \pm 8.6$ cm^{-1} for the C 0^+ state relative to the $Na(^2P_J) + I(^2P_{3/2})$ asymptote and an eqilibrium bond distance of $r_e = 3.30673 \pm 0.00054$ Å. Although the value of $D_e = 1863$ cm^{-1} reported here is somewhat larger than that obtained by high-resolution spectroscopy, a well depth of only ≈ 530 cm^{-1} would certainly not explain the splitting data obtained as a function of probe wavelength at different photolysis energies as determined in this study (see Section IV). Figure 4.10 offers a diagrammatic comparison of the potential energy curve for the fluorescing state determined by FTS with those for the C 0^+ state derived from frequency-resolved measurements.[11,12]

IV. Quantum Dynamics

In this section the experimental clocking and splitting data in terms of the wave packet dynamics representing $[Na\cdots I]^{\ddagger *}$ transition states on the electronically excited A 0^+ potential are discussed. In an attempt to simulate the FTS experiment and to provide a justification of the potential inversion procedure presented in Section III, second-order, time-dependent perturbation theory is invoked to calculate the transient behavior arising from motion of $[Na\cdots I]^{\ddagger *}$ wave packets within the adiabatic potential well $E_2(r)$ (see Figure 4.1).

IV.1 Theoretical Approach

For weak transform-limited pump and probe laser pulses, the wavefunction $|\psi_3(t)\rangle$ created on the final (fluorescent) potential $E_3(r)$ is given by the well-known perturbation-

theory expression[28]:

$$|\psi_3(t)\rangle = (-i/h)^2 \int_{-\infty}^{t} dt_2 \int_{-\infty}^{t2} dt_1 T_3(t-t_2) U_{32}(t_2) T_2(t_2-t_1) U_{21}(t_1) \exp(-i\omega_v t_1) |\varphi_v\rangle , \qquad (4.11)$$

where the electric-dipole approximation is assumed for interaction of the molecule with the two laser pulses. The operators $T_i(t) = \exp(-iH_i t)$ propagate the three wavefunctions $|\psi_i(t)\rangle$ (i = 1, 2, 3) on the ground-state $E_1(r)$, intermediate $E_2(r)$ and final $V_3(r)$ potential-energy curves as a function of time. The H_i are Hamiltonian operators appropriate to the three potential functions. The time-dependent perturbations caused by the pump and probe laser pulses are represented by the operators:

$$U_{ij}(t_k) = \boldsymbol{\mu}_{ij}(r) \cdot \boldsymbol{E}_k(t_k) g_k(t_k) \qquad (4.12)$$

where k labels the laser pulse that couples electronic states |i> and |j> optically . It is assumed that the Condon approximation is valid for variation of the transition-dipole moment operators $\boldsymbol{\mu}_{ij}(r)$ with Na···I separation coordinate r. $E_k(t_k)$ is the electric field strength of the radiation field that is due to the kth laser, the temporal lineshape $g_k(t_k)$ of which is taken to be Gaussian with a FWHM = 100 fs for both pump (k = 1) and probe (k = 2) pulses.

The wavefunction $|\psi_2(t)\rangle$ prepared on the adiabatic potential $E_2(r)$ at a time t_1 by the pump-pulse perturbation $U_{21}(t_1)$ consists of a superposition of vibrational eigenstates whose relative contributions are determined by the frequency and temporal duration of the pump laser and appropriate Franck-Condon factors. At λ_1 = 320 nm, the photolysis wavelength employed in these calculations, absorption of a pump photon by the ground-state wavefunction $|\psi_1(t)\rangle$ results in preparation of an initial wave packet $|\psi_2(t)\rangle$ on $E_2(r)$

with available energy E_{av} above the covalent dissociation limit leading to $Na(^2S_{1/2})$ + $I(^2P_{3/2})$ atoms. At this excitation energy, the pump pulse prepares $|\psi_2(t)>$ essentially at the classical turning point of $E_2(r)$ with no tunneling through classically forbidden regions of configuration space. The higher-lying potential $E_3(r)$ is populated by the probe-pulse perturbation $U_{32}(t_2)$ at time t_2. Since it is not time-resolved, intensity modulations in the fluorescence excited by the probe laser depend only upon the pump-probe delay time τ rather than on any coherence effects on $E_3(r)$, which are averaged out. The oscillation frequencies observed in the time-resolved LIF spectra arise solely from the dynamics of the wave packet $|\psi_2(t)>$ on $E_2(r)$; the signal intensity as a function of τ, of course, depends upon the topologies and relative locations of the three PES's in configuration space (reflected by different Franck-Condon factors); the (electronic) transition-dipole moments between these surfaces, the probability for undergoing an avoided crossing from $E_2(r)$ to $E_1(r)$, and the laser lineshapes.

Ideally, the single ground-state eigenfunction of Equation (4.11) should be replaced by the appropriate density matrix representing the thermal population distribution on $E_1(r)$ at T = 650 ^{0}C. Franck-Condon overlap arguments, however, together with a Boltzmann distribution of vibrational-state population, indicate that the lowest vibrational level of $E_1(r)$ carries most intensity for absorption of a pump photon at λ_1 = 320 nm. Therefore, the initial wavefunction $|\psi_1(t)> = \exp(-i\omega_v t_1)|\varphi_v>$ is taken to be the Gaussian form of the v" = 0 level of the ground electronic state comprising a nuclear eigenfunction $|\varphi_v>$ with a phase factor $\exp(-i\omega_v t_1)$.

IV.2 Wave-Packet Motion in the Time Domain

The simulation of the FTS experiment proceeds as follows. The v" = 0 eigenfunction of NaI in its X $^1\Sigma_0^+$ electronic state is excited to the reactive $E_2(r)$ potential by

interaction with a pump-pulse photon at λ_1 = 320 nm. This is followed (or preceded) at a delay time τ by promotion of $|\psi_2(t)\rangle$ to the fluorescing state by means of a vertical transition induced by a probe photon: Two probe-laser wavelengths of λ_2 = 600 and 640 nm in this work are employed. As discussed in subsection III.1, the longer of these wavelengths corresponds to probing the dynamics over a range of distances (determined by the spectral bandwidth) centered about r = 5.0 Å on the broad potential minimum of $E_2(r)$, while the shorter wavelength monitors passage of the wave packet at r ≈ 6.5 Å, closer to the outer turning point.

The calculation carried out in here is close in spirit to those previously reported by Engel, Metiu *et al.* for NaI predissociation.[23] The split-operator method devised by Feit and coworkers[29] was employed to propagate wavefunctions using a discretized version of Equation (1) (time-slice approximation) during the two laser pulses. $|\psi_2(t)\rangle$ was allowed to evolve over $E_2(r)$ for delay times up to τ = 3000 fs. The adiabatic potentials $E_1(r)$ and $E_2(r)$ formed by mixing of the diabatic potentials $V_1(r)$ and $V_2(r)$ are given by Equation (4.2). For $E_3(r)$, the Morse potential of equation (4.10) is invoked with parameters given in subsection III.3.

Since we are concerned only with the short-time behavior of the wave packet dynamics (in particular the bidirectionality of the wave packet motion and the oscillation frequency), leakage of the wave packet to form Na + I atomic products on $E_2(r)$ by means of an avoided crossing between adiabatic curves at r_x = 6.93 Å is not treated explicitly, though it could be included to mimic more accurately the observed decrease in LIF intensity with increasing time delay τ as the population of species remaining within the adiabatic well $E_2(r)$ is depleted. In FTS, the time evolution of $|\psi_2(t)\rangle$ is monitored by detection of time-integrated fluorescence from the wave packet $|\psi_3(t)\rangle$ excited by the probe laser. This emission is proportional to the probability density $\langle\psi_3(t)|\psi_3(t)\rangle$ for finding the system in state $|3\rangle$ at a time t immediately following the probe pulse. Our simulated FTS data

therefore consist of plots of $\langle\psi_3(t)|\psi_3(t)\rangle$ versus τ.

Figure 4.11 displays FTS transients for the two probe wavelengths employed in our calculations for pump-probe delay times τ across the range -100 to 3000 fs. Both spectra show vibrational oscillation of the wave packet with a period of τ_{osc} = 1096 fs, identical to the experimentally measured value. Only at λ_2 = 600 nm, however, is the splitting of the second and third peaks into a doublet structure resolvable: The time between the two doublets centered at τ = 1096 and 2192 fs in Figure 4.11(a) is τ_s = 308 fs in both cases, in reasonable overall agreement with the experimental result listed in Table 4.1. As pointed out in Section II, the splitting time τ_s represents the time taken for the wave packet to travel from its initial position at the classical turning point of $E_2(r)$ to the center of the detection window defined by the spectral bandwidth of the probe pulse. Although no doublet structure is resolvable for the longer probe wavelength (and likewise in the experiment), it may be noted that the maximum of the first peak shown in Figure 4.11(b) occurs after some 77 fs. According to the analysis presented in Section II, this time should be half the splitting time t_s; hence, the underlying splitting time in Figure 4.7(b) is τ_s = 154 fs, in accord with the experimental value listed in Table 4.1.

Calculations have also been carried out using the Morse curve for $E_3(r)$ postulated by Bower *et al.*[11] In this case, the experimental splitting data were not reproduced satisfactorily to quantitative accuracy: Values of τ_s = 202 and 96 fs were determined for λ_2 = 600 and 640 nm, respectively. The period τ_{osc} remains unchanged at 1096 fs, however, since the oscillation frequency depends only upon the shape of $E_2(r)$.

Application of Equation (4.11) to solve for the nuclear motion of $[Na\cdots I]^{\ddagger *}$ transition states within a bound potential well has resulted in quantitative confirmation from quantum dynamics of the validity of the potential inversion method outlined in Section III, at least for a single pump wavelength. By extending the theoretical investigations to include

computation of FTS transients at other photolysis energies, a more rigorous test of the potential-inversion procedure may be undertaken, which would further allow the shapes of the potential energy curves so derived to be verified, or of course otherwise, within the limitations of the calculation.

V. Conclusions

In this chapter, a classical mechanical inversion procedure has been developed for elucidation of potential-energy curves from measurements of transition-state dynamics in the time domain for systems in which it is not possible to use conventional RKR techniques. Application has been made to the predissociation reaction of NaI, enabling potential functions for two electronically excited states (A 0^+ and possibly C 0^+) of NaI to be determined from FTS clocking experiments.

Overall, the adiabatic potential for the A 0^+ state derived in this way is in close accord at long internuclear separations with the results of spectroscopic measurements carried out in the frequency domain;[2,3,5,7] agreement is less satisfactory, however, at short distances in the region of the inner turning point. For the highest-lying state accessed in FTS experiments, the potential-energy curve so derived possesses a deeper minimum at a larger equilibrium Na···I bond distance than those for the C 0^+ state determined by laser-excitation spectroscopy[12] and the high-lying state analyzed by broadband excitation of predissociating NaI.[11] Time-dependent quantum dynamical calculations of the behavior of $[Na\cdots I]^{\ddagger *}$ transition states within the A 0^+ adiabatic well generate simulated transients that offer quantitative support to the form of the potential-energy curves derived from FTS experiments.

VI. References

1. R. S. Berry, in: *Alkali Halide Vapors*, eds. P. Davidovits and D. L. McFadden (Academic Press, New York, 1979) p. 77, and references therein.
2. N. J. A. van Veen, M. S. de Vries, J. D. Sokol, T. Baller and A. E. de Vries, *Chem.Phys.* **56**, 81 (1981).
3. S. H. Schaefer, D. Bender and E. Tiemann, *Chem. Phys. Letters* **92**, 273 (1982); *Chem. Phys.* **89**, 65 (1984).
4. M. S. Child, in: *Specialist Periodical Reports. Molecular Spectroscopy,* Vol. 2 (Chem. Soc., London, 1974) Ch. 7, p. 466; *J. Mol. Spectry* **53**, 280 (1974).
5. J. Wang, A. J. Blake, D. G. McCoy and L. Torop, *Chem. Phys. Letters* **175**, 225 (1990).
6. S. Chapman and M. S. Child, *J. Phys. Chem.* **95**, 578 (1991).
7. H. Bluhm and E. Tiemann, private communication.
8. A. M. Moutinho, J. A. Aten and J. Los, *Physica* **53**, 471 (1971); G. A. L. Delvigne and J. Los, *Physica* **67**, 166 (1973).
9. M. B. Faist and R. D. Levine, *J. Chem. Phys.* **64**, 2953 (1976).
10. S. E. Choi and J. C. Light, *J. Chem. Phys.* **90**, 2593 (1989).
11. R. D. Bower, P. Chevrier, P. Das, H. J. Foth, J. C. Polanyi, M. G. Prisant and J.Visticot, *J. Chem. Phys.* **89**, 4478 (1988).
12. H. Bluhm, J. Lindner and E. Tiemann, *J. Chem. Phys.* **93**, 4556 (1990).
13. T. S. Rose, M. J. Rosker and A. H. Zewail, *J. Chem. Phys.* **88**, 6672 (1988); M. J. Rosker, T. S. Rose and A. H. Zewail, *Chem. Phys. Letters* **146**, 175 (1988).
14. T. S. Rose, M.J. Rosker and A. H. Zewail, *J. Chem. Phys.* **91**, 7415 (1989).
15. P. Cong, A. Mokhtari and A. H. Zewail, *Chem. Phys. Letters* **172**, 109 (1990).

16. A. Mokhtari, P. Cong, J. L. Herek and A. H. Zewail, *Nature* (London) **348**, 225 (1990).

17. M. Gruebele, G. Roberts, M. Dantus, R. M. Bowman and A.H. Zewail, *Chem. Phys.Letters* **166**, 459 (1990).

18. J. S. Baskin, P. M. Felker and A. H. Zewail, *J. Chem. Phys.* **84**, 4708 (1986) ; P. M. Felker, J. S. Baskin and A.H. Zewail, *J. Phys. Chem.* **90**, 724 (1986); P. M. Felker and A. H. Zewail, *J. Chem. Phys.* **86**, 2460 (1987); J. S. Baskin and A. H. Zewail, J. Phys. Chem. **93**, 5701 (1989).

19. M. . Rosker, M. Dantus and A.H. Zewail, *Science* **241**, 1200 (1988); M. Dantus, M. J. Rosker and A.H. Zewail, *J. Chem. Phys.* **89**, 6128 (1988) .

20. R. B. Bernstein, *Chemical Dynamics via Molecular Beam and Laser Techniques* (Clarendon Press, Oxford, 1982), Ch. 8, p. 169.

21. R. Bersohn and A. H. Zewail, *Ber. Bunsenges. Phys. Chem.* **92**, 373 (1988).

22. A. Messiah, *Quantum Mechanics*, Vol. 1 (North-Holland, Amsterdam, 1966), Ch. VI, pp. 214-222.

23. V. Engel, H. Metiu, R. Almeida, R. A. Marcus and A. H. Zewail, *Chem. Phys. Letters* **152**, 1 (1988); V. Engel and H. Metiu, *J. Chem. Phys.* **90**, 6116 (1989); *J. Chem.Phys.* **91**, 1596 (1989); H. Metiu and V. Engel, *J. Opt. Soc. Amer.* **B7**, 1709 (1990).

24. S-Y. Lee, W. T. Pollard and R. A. Mathies, *J. Chem. Phys.* **90**, 6146 (1989).

25. T-M. R. Su and S. J. Riley, *J. Chem. Phys.* **71**, 3194 (1979).

26. A. H. Zewail and coworkers, to be published.

27. R. B. Bernstein and A. H. Zewail, *Chem. Phys. Letters* **170**, 321 (1990).

28. R. Loudon, *The Quantum Theory of Light* (Clarendon Press, Oxford, 1973), Ch. 11, p. 279.

29. M. D. Feit, J. A. Fleck, Jr. and A. Steiger, *J. Comput. Phys.* **47**, 412 (1982); M. D. Feit and J. A. Fleck Jr., *J. Chem. Phys.* **78**, 301 (1983); C. Leforestier, R. H.

Bisseling, C. Cerjan, M. D. Feit, R. Friesner, A. Guldberg, A. Hammerich, G. Jolicard, W. Karrlein, H-D. Meyer, N. Lipkin, O. Roncero and R. Kosloff, *J. Comput. Phys.* **94**, 59 (1991).

VII. Tables

Table 4.1

Time τ_0 for a wave packet on the adiabatic potential $E_2(r)$ to reach the center of the optically-coupled region projected on $E_2(r)$ by a probe laser of wavelength λ_2 (pump wavelength λ_1 = 310 nm).

λ_2/nm	τ_0/fs
600	118
623	96
642	66
652	28
662	22
676	35
698	43

Table 4.2

Splitting time τ_s between the doublet intensity maxima of the second and subsequent peaks of FTS transients at different pump and probe wavelengths.

λ_1/nm	λ_2/nm			
	600	623	642	662
310	305			
320	326	233	150	
330	343	262	180	
340	351	241	229	173
350	367	278	242	189
355	373	289		
360	373	314	260	
365	374	313		
390	431	355	269	

Table 4.3

Vibrational periods τ_{osc} of $[Na\cdots I]^{\ddagger *}$ transition states trapped with the adiabatic well $E_2(r)$ as a function of pump wavelength λ_1. E_{av} is the excess energy available to $[Na\cdots I]^{\ddagger *}$ vibration calculated as the difference between the photolysis energy and NaI dissociation energy.

λ_1/nm	E_{av}/cm^{-1}	τ_{osc}/fs
310	6852	1281
320	5844	1095
330	4897	1009
340	4005	991
350	3165	959
360	2371	936
390	235	915

Table 4.4

Results of potential inversion based on the Rittner-type potential

A. Recoil energies in cm^{-1} for different α values:

λ_{pump} (nm)	α=1.0	α=2.0	α=2.5	α=3.0	α=4.088
320	6053	5950	5933	5904	5800
330	5588	5262	5171	5158	5131
340	5158	4667	4563	4440	4357
350	4858	4223	4027	3879	3700
355	4714	3977	3805	3653	3409
360	4575	3821	3599	3415	3142
365	4460	3671	3381	3192	2895
391	3918	2888	2550	2294	1924

B. The internuclear distances (Å) reached after $\tau_s/2$ at 605 nm probing:

λ_{pump} (nm)	α=1.0	α=2.0	α=2.5	α=3.0	a=4.088
320	5.84	6.46	6.58	6.66	6.77
330	5.98	6.48	6.58	6.65	6.74
340	5.98	6.38	6.46	6.48	6.53
350	6.11	6.41	6.43	6.43	6.42
355	6.12	6.38	6.39	6.37	6.33
360	6.06	6.32	6.30	6.26	6.19
365	6.08	6.25	6.22	6.18	6.09
391	6.57	6.48	6.35	6.21	5.96
Average	6.09	6.40	6.41	6.40	6.38
Stan. dev. (1σ)	0.21	0.08	0.13	0.19	0.29

Table 4.5

Results of potential inversion based on the Morse-fitted RKR potential

A. Recoil energies in cm^{-1} for different α values:

λ_{pump} (nm)	α=1.0	α=1.5	α=2.0	α=2.5	α=3.5
320	5874	5772	5758	5715	5700
330	5342	5120	5006	4919	4870
340	4956	4609	4400	4287	4088
350	4621	4212	3938	3736	3492
355	4462	4027	3708	3510	3200
360	4330	3850	3527	3275	2920
365	4202	3681	3337	3075	2733
391	3644	3015	2600	2238	1780

B. The internuclear distances (Å) reached after $\tau_s/2$ at 605 nm probing:

λ_{pump} (nm)	α=1.0	α=1.5	α=2.0	α=2.5	α=3.5
320	5.80	6.20	6.41	6.52	6.70
330	5.92	6.25	6.41	6.49	6.60
340	5.94	6.20	6.30	6.35	6.38
350	6.05	6.26	6.31	6.31	6.29
355	6.05	6.24	6.26	6.26	6.20
360	6.02	6.18	6.19	6.15	6.05
365	6.01	6.14	6.13	6.08	5.98
391	6.47	6.45	6.33	6.16	5.87
Average	6.03	6.24	6.29	6.29	6.26
Stan. dev. (1σ)	0.20	0.09	0.10	0.16	0.29

Table 4.6

Results of the inversion procedure based on the Morse-fitted potential and the combination of Boltzmann and Franck-Condon factors.

A. Recoil energies (cm^{-1}) for different α values:

λ_{pump} (nm)	α=1.0	α=2.0	α=2.5	α=3.0	α=4.088
320	6305	6069	6060	6050	6040
330	5688	5330	5262	5209	5149
340	5219	4769	4608	4506	4380
350	4882	4301	4069	3917	3716
355	4735	4040	3810	3659	3421
360	4601	3777	3614	3423	3151
365	4482	3723	3393	3199	2904
391	3920	2979	2636	2322	1911

B. The internuclear distances (Å) reached after $\tau_s/2$ at 605 nm probing:

λ_{pump} (nm)	α=1.0	α=2.0	α=2.5	α=3.0	α=4.08
320	5.89	6.50	6.62	6.71	6.82
330	6.00	6.51	6.61	6.67	6.74
340	6.00	6.42	6.47	6.50	6.54
350	6.11	6.45	6.45	6.44	6.43
355	6.12	6.39	6.39	6.38	6.33
360	6.09	6.29	6.30	6.27	6.20
365	6.08	6.29	6.23	6.18	6.09
391	6.57	6.53	6.40	6.23	5.97
Average	6.11	6.42	6.43	6.42	6.39
Stan. dev. (1σ)	0.20	0.09	0.14	0.20	0.30

VIII. Figures

Captions:

Figure 4.1

Low-lying potential energy curves relevant to FTS investigations of NaI predissociation. A thermal distribution of molecules is promoted by a pump pulse at wavelength λ_1 from the ground-state potential $E_1(r)$ to the predissociative potential $E_2(r)$, which correlates adiabatically with $Na^+(^1S_0) + I^-(^1S_0)$ ions. The wave packet formed on $E_2(r)$, comprising a distribution of eigenstates determined by the spectral profile of the pump laser, oscillates within the adiabatic well with diminishing amplitude as a fraction proceeds to neutral $Na(^2S_{1/2}) + I(^2P_{3/2})$ products via an avoided crossing to the $E_1(r)$ continuum. A probe pulse at wavelength l_2 monitors the dynamics of the wave packet on $E_2(r)$ every time it enters the resonant absorption region by excitation to the higher-lying potential $E_3(r)$, from which time-integrated $Na(^2P_J \rightarrow {}^2S_{1/2})$ fluorescence is detected. In this diagram, λ_1 = 320 nm and λ_2 = 640 nm are shown for illustration.

Figure 4.2

Schematic representation of the experimental configuration adopted for clocking experiments of NaI predissociation. The probe pulse is delayed in time relative to the pump pulse before the two are focused into the reaction cell containing NaI. The cross-correlation of the pump and probe pulses was measured at point **A** by deflecting the beams through a KD*P crystal and detecting the frequency difference signal as function of pump-probe time delay. By translating the vapour cell out of the optical path and recording the cross correlation at point **B**, the dispersion between the pulses that is due to the quartz window could be measured, corresponding to one half the difference between the two cross-correlation signals. A similar correction for dispersion from the KD*P crystal was also made. When these

corrections were subtracted from the cross-correlation signal, time zero was obtained to within ± 20 fs.

Figure 4.3

Experimental transients obtained at different pump-laser wavelengths. Graphs of LIF signal intensity (arbitrary units) versus pump-probe time delay τ (ps) recorded at a probe wavelength of λ_2 = 605 nm and pump wavelengths ranging from from 310 nm to 390 nm.

Figure 4.4

Experimental transients obtained at different probe-laser wavelengths. Graphs of LIF signal intensity (arbitrary units) versus pump-probe time delay τ (ps) recorded at a pump wavelength of λ_1 = 391 nm and various probe wavelengths as labeled.

Figure 4.5

Typical FTS data with non-linear least-squares fit shown as a solid curve. Graph of LIF signal intensity (arbitrary units) versus pump-probe time delay τ (ps) showing the splitting time τ_s between observed intensity maxima (other than the initial peak) and the average oscillation period t_{osc} of the wave packet trapped within the adiabatic well $E_2(r)$.

Figure 4.6

Comparison of quantum and classical trajectories of NaI internuclear separation as a function of time. The pump wavelength is at 350 nm. See text for details.

Figure 4.7

The effects of different choices of the repulsive range parameter α on the classical

trajectories R(t) at various pump wavelengths. The solid dots represent the internuclear separations reached after $\tau_s/2$ at a probe wavelength of 605 nm. For an α parameter that is consistent with the experimental results from the splitting time τ_s measurements, the solid dots should be on a horizontal line (see text for detailed explanations). When an α value is too small, the line tilts up, implying that the recoil energies for long pump wavelengths are overestimated. A too large α value shows the opposite trend.

Figure 4.8

Comparison of different ground-state potentials for NaI. The potentials are shown for only the first 5000 cm^{-1} above the minimum in order to focus the attention on the region around the equilibrium bond length. For a global comparison, see Figure 2.4.

Figure 4.9

Comparison of potential-energy curves for the A 0^+ electronic state of NaI. Plots of potential energy E_2 (10^3 cm^{-1}) versus Na···I bond distance (Å):

———: FTS (this work);

·····: photofragment spectroscopy (Ref. 2);

–·–·–·–: absorption spectroscopy (Ref. 3);

– – – – : numerical optimization (Ref. 5);

– - – -: OODR spectroscopy (Ref. 7).

Figure 4.10

Comparison of potential-energy curves for the C 0^+ electronic state of NaI. Plots of potential energy E_3 (10^3 cm^{-1}) versus Na···I bond distance (Å):

———: FTS (this work);

–·–·–·–: far-wing emission (Ref. 11);

xxxxxx: laser excitation spectroscopy (Ref. 12).

Figure 4.11

Transient behavior calculated by quantum dynamics. Graphs of the norm of the wavefunction $|\psi_3(t)\rangle$ created on $E_3(r)$ by action of the probe laser versus pump-probe time delay τ for a pump wavelength of λ_1 = 320 nm and two probe wavelengths: (a) λ_2 = 600 nm; (b) λ_2 = 640 nm. Both transform-limited laser pulses have Gaussian temporal profiles of FWHM = 100 fs, and values of $\langle\psi_3(t)|\psi_3(t)\rangle$ are normalized with respect to the maximum intensity of the earliest peak shown in (a).

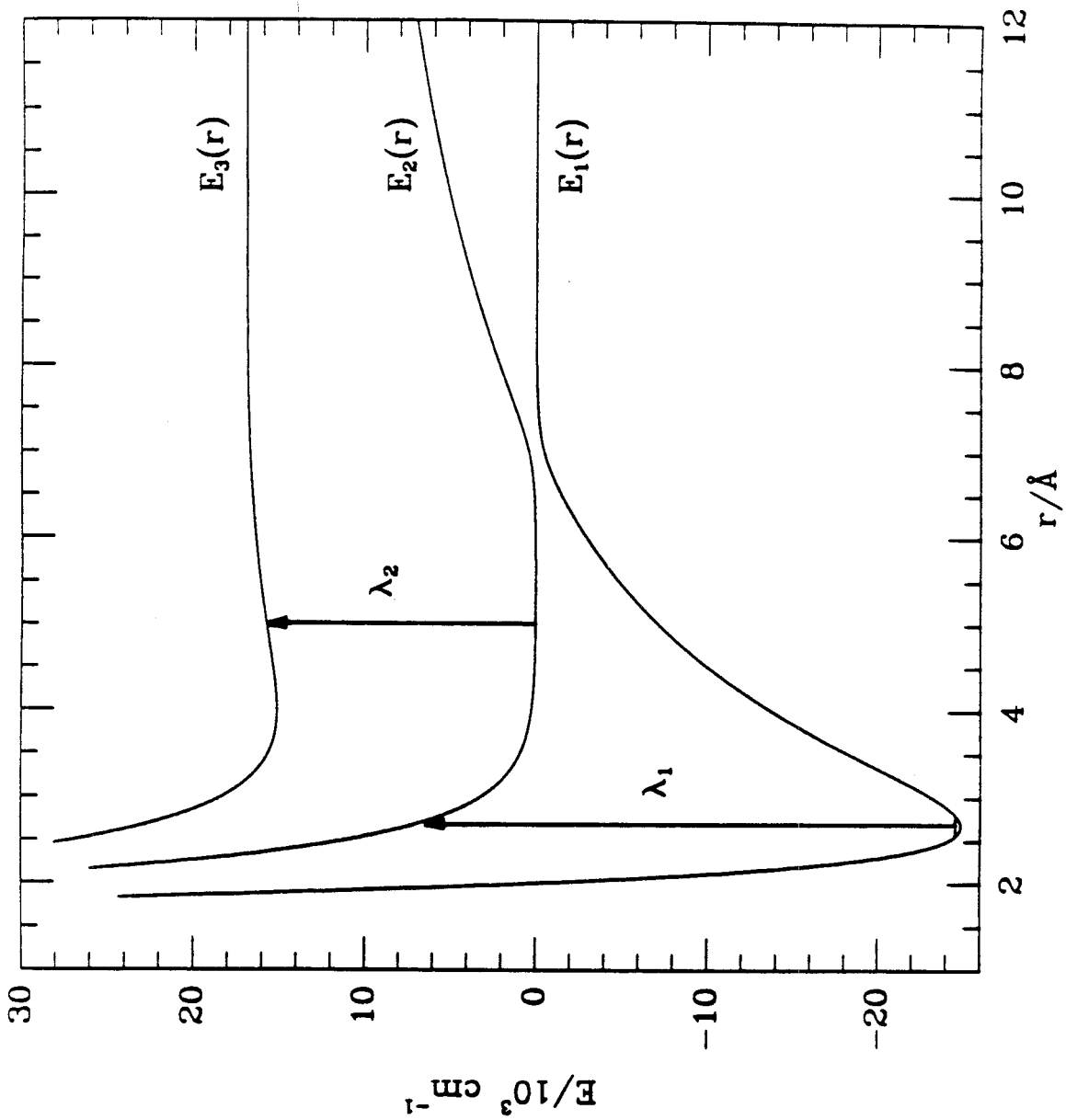

Figure 4.1

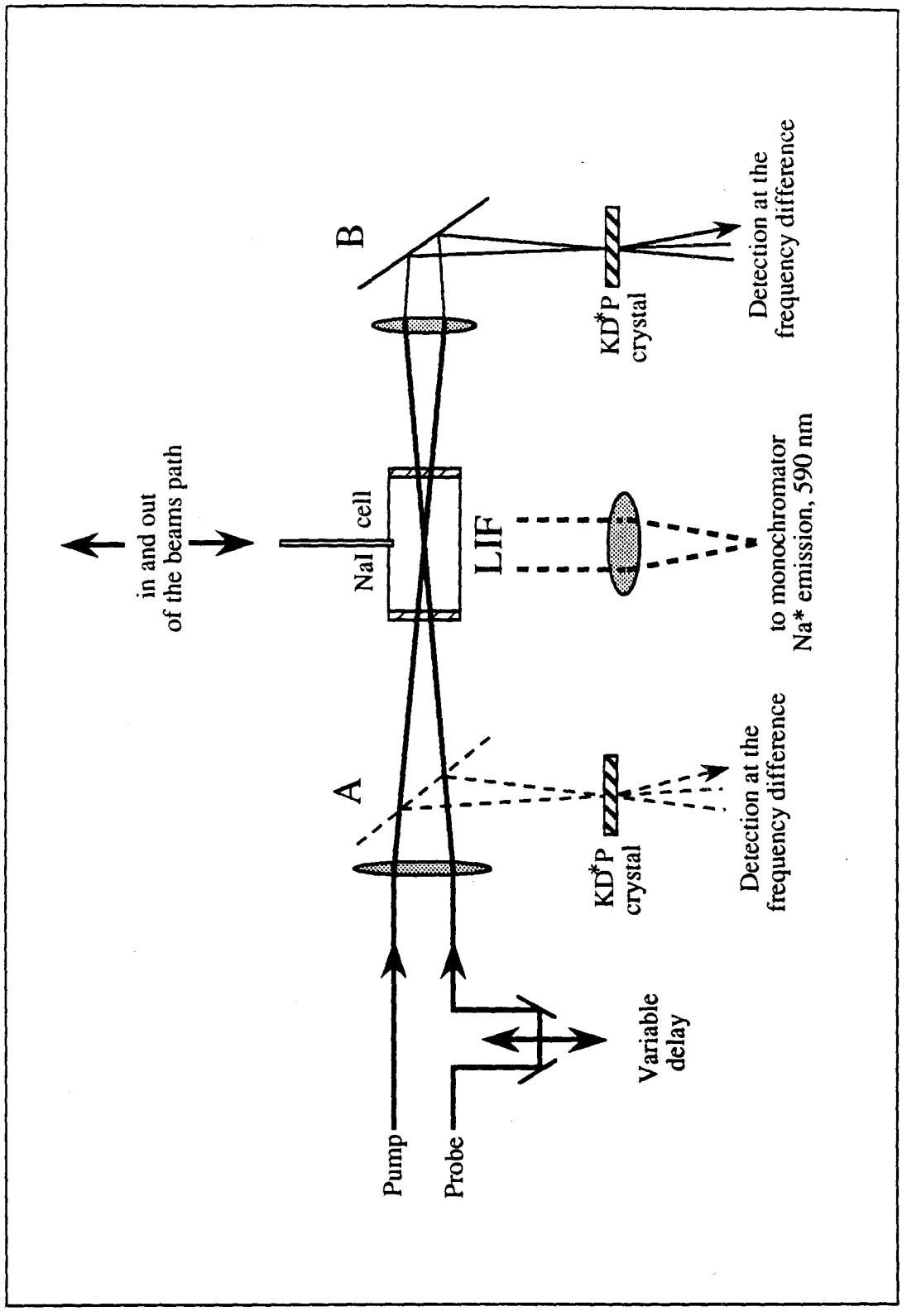
B
A
LIF
NaI cell
in and out
of the beams path
KD*P
crystal
Detection at the
frequency difference
to monochromator
Na* emission, 590 nm
KD*P
crystal
Detection at the
frequency difference
Variable
delay
Pump
Probe

Figure 4.2

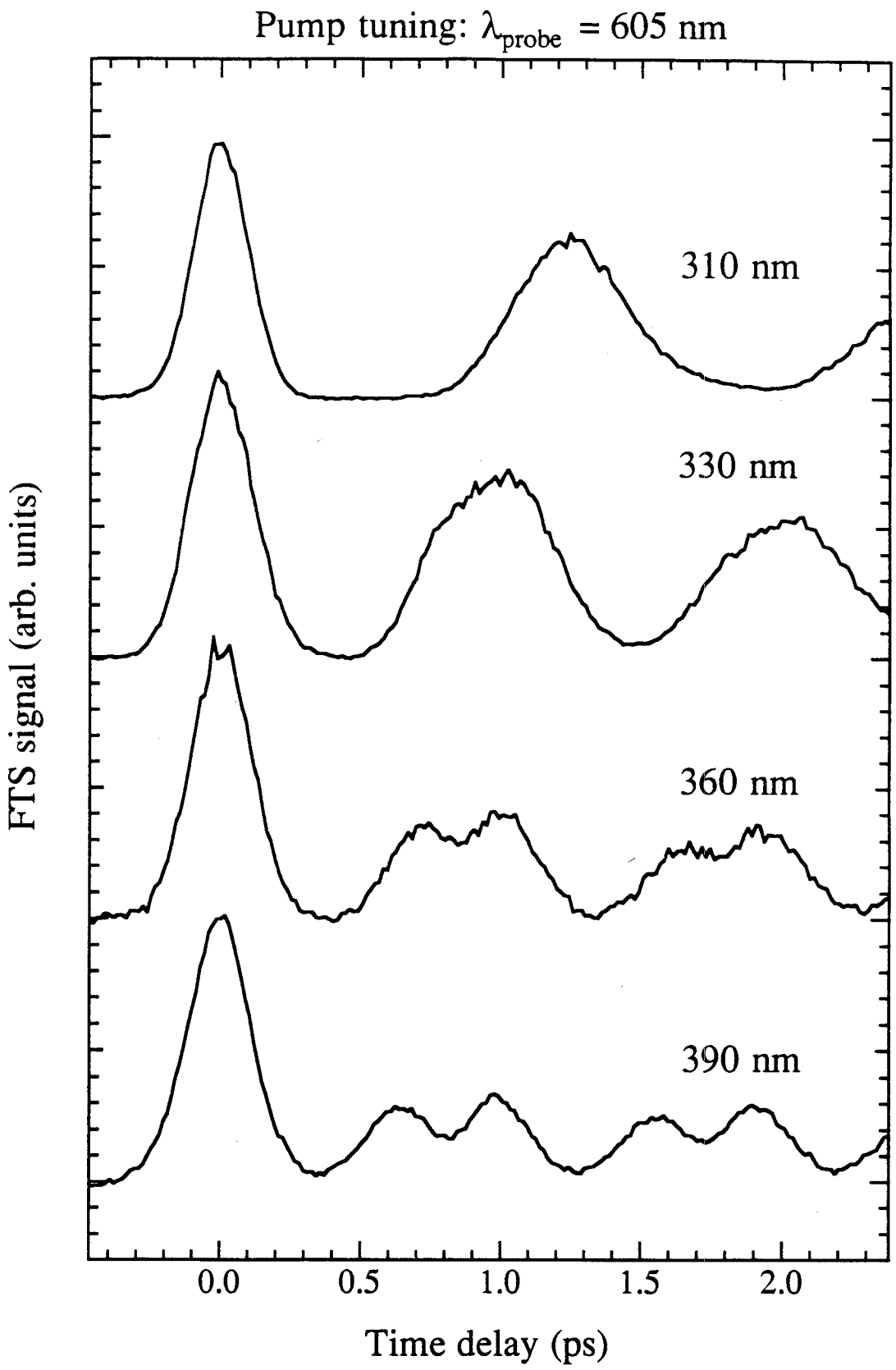
Pump tuning: λ_{probe} = 605 nm
310 nm
330 nm
360 nm
390 nm
FTS signal (arb. units)
0.0
0.5
1.0
1.5
2.0
Time delay (ps)

Figure 4.3

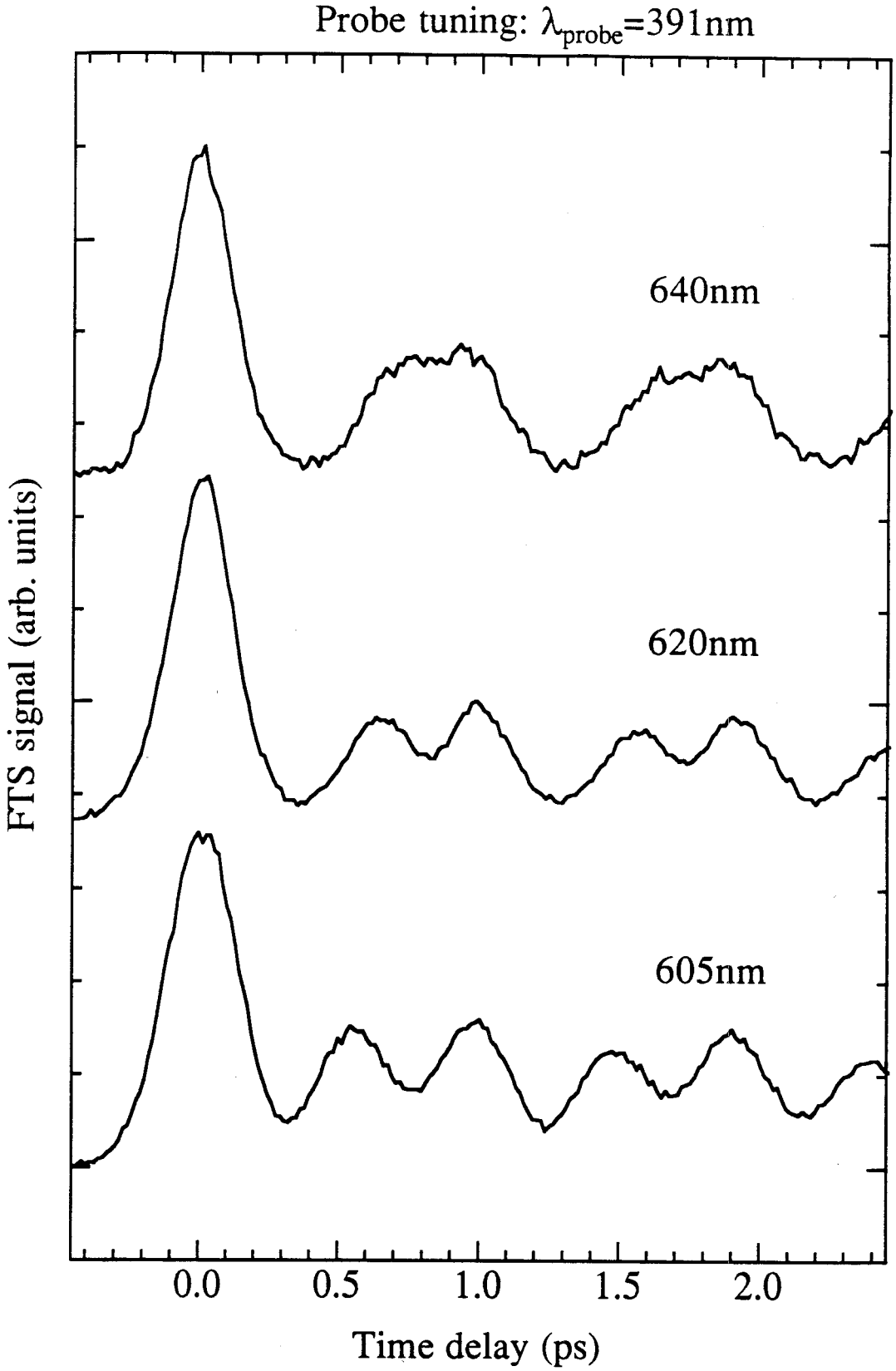
Probe tuning: λ_{probe}=391nm
640nm
620nm
605nm
FTS signal (arb. units)
0.0
0.5
1.0
1.5
2.0
Time delay (ps)

Figure 4.4

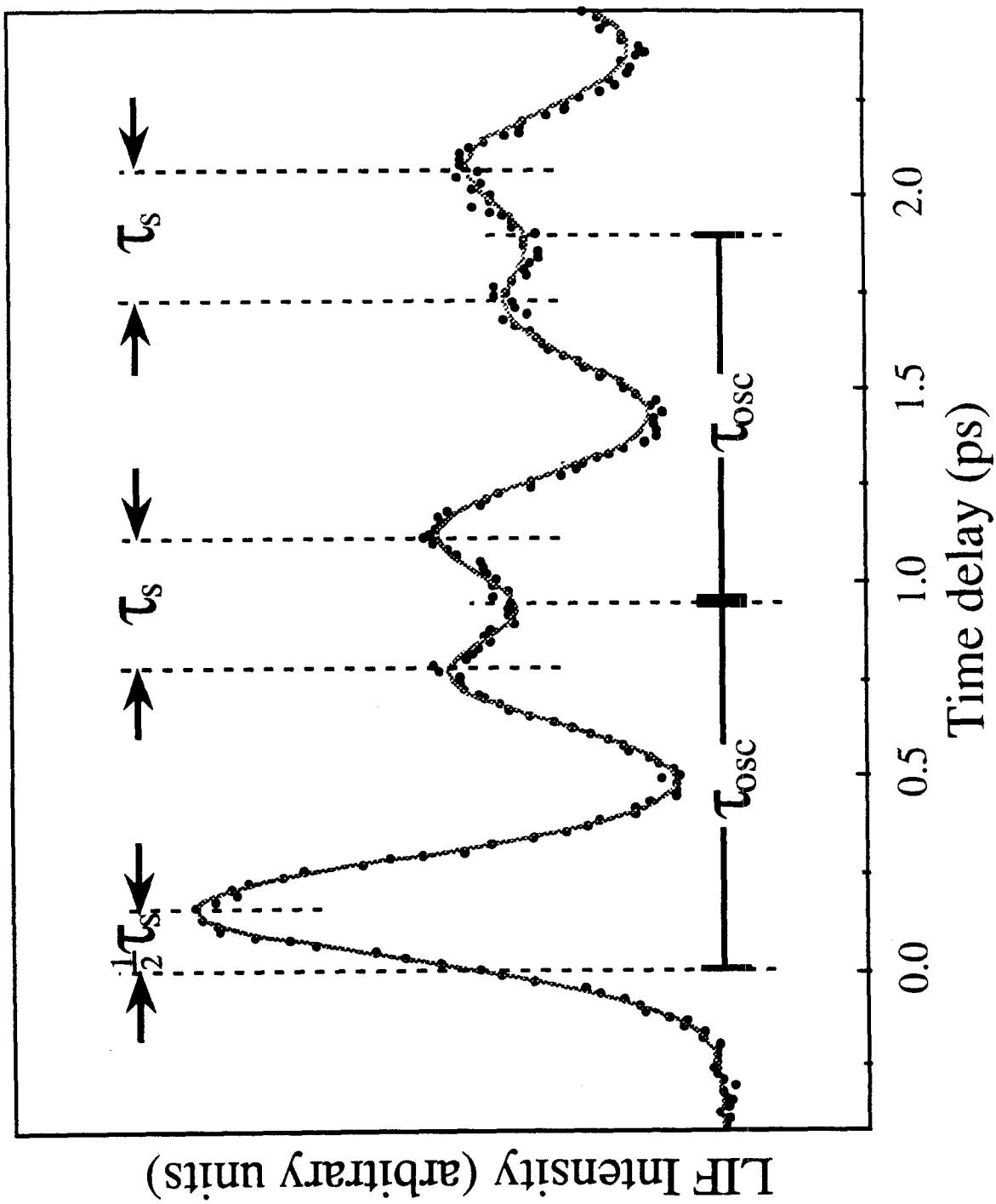
LIF Intensity (arbitrary units)
Time delay (ps)
0.0
0.5
1.0
1.5
2.0
τ_{osc}
τ_{osc}
τ_s
τ_s
$\frac{1}{2}\tau_s$

Figure 4.5

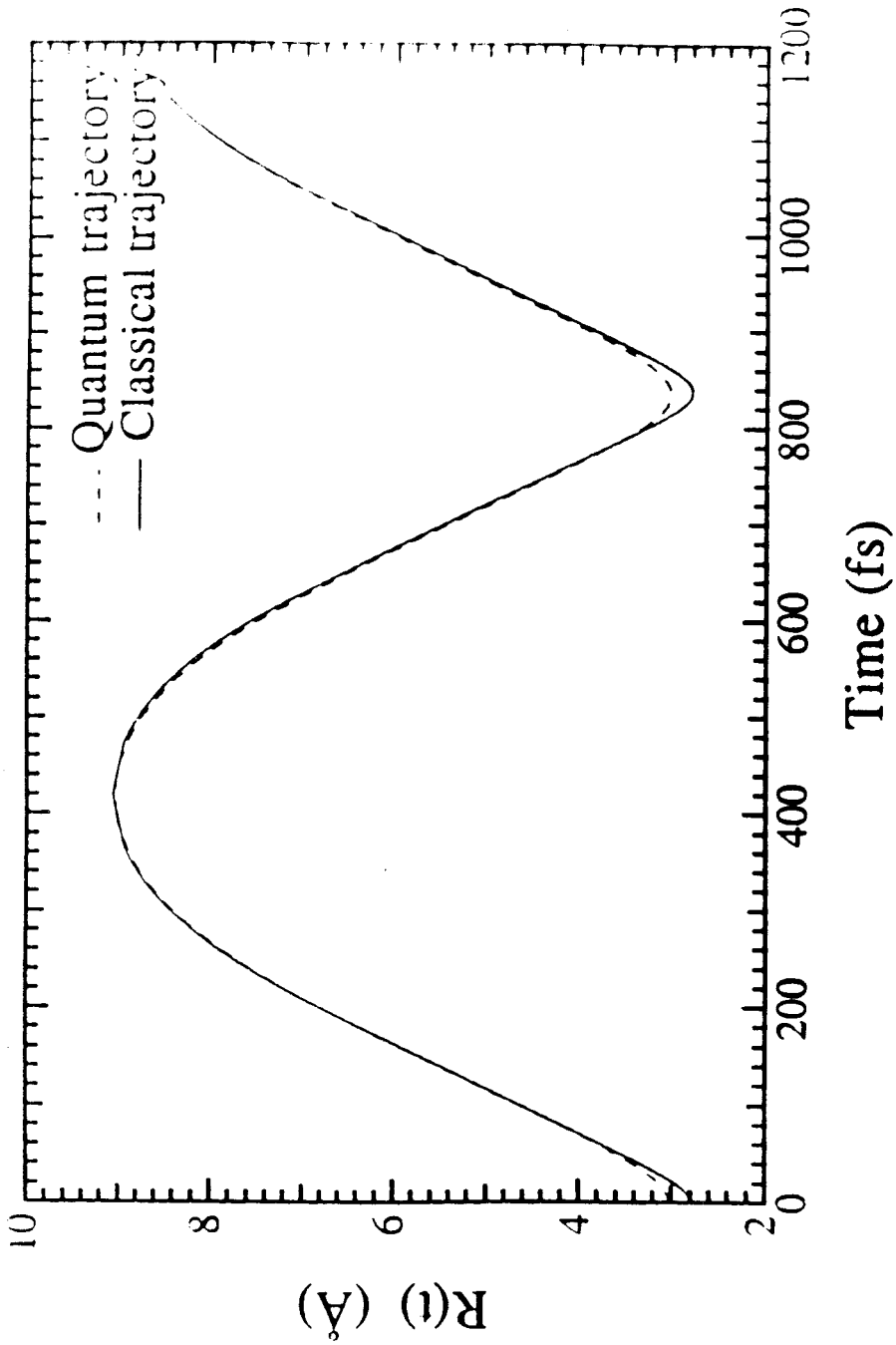
Quantum trajectory
Classical trajectory
R(t) (Å)
Time (fs)
2
4
6
8
10
0
200
400
600
800
1000
1200

Figure 4.6

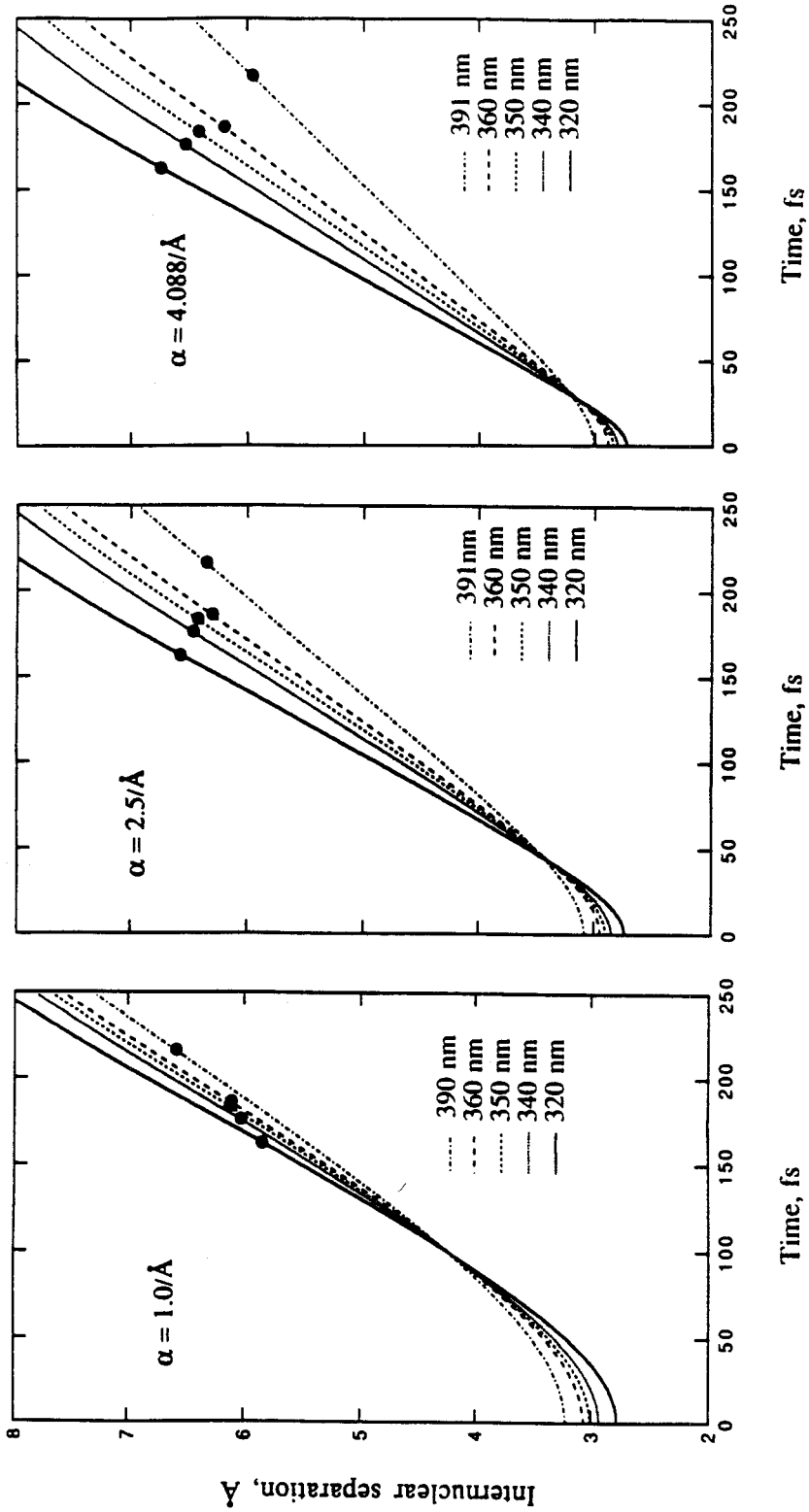
α = 1.0/Å
α = 2.5/Å
α = 4.088/Å
390 nm
391nm
391 nm
360 nm
350 nm
340 nm
320 nm
Internuclear separation, Å
Time, fs

Figure 4.7

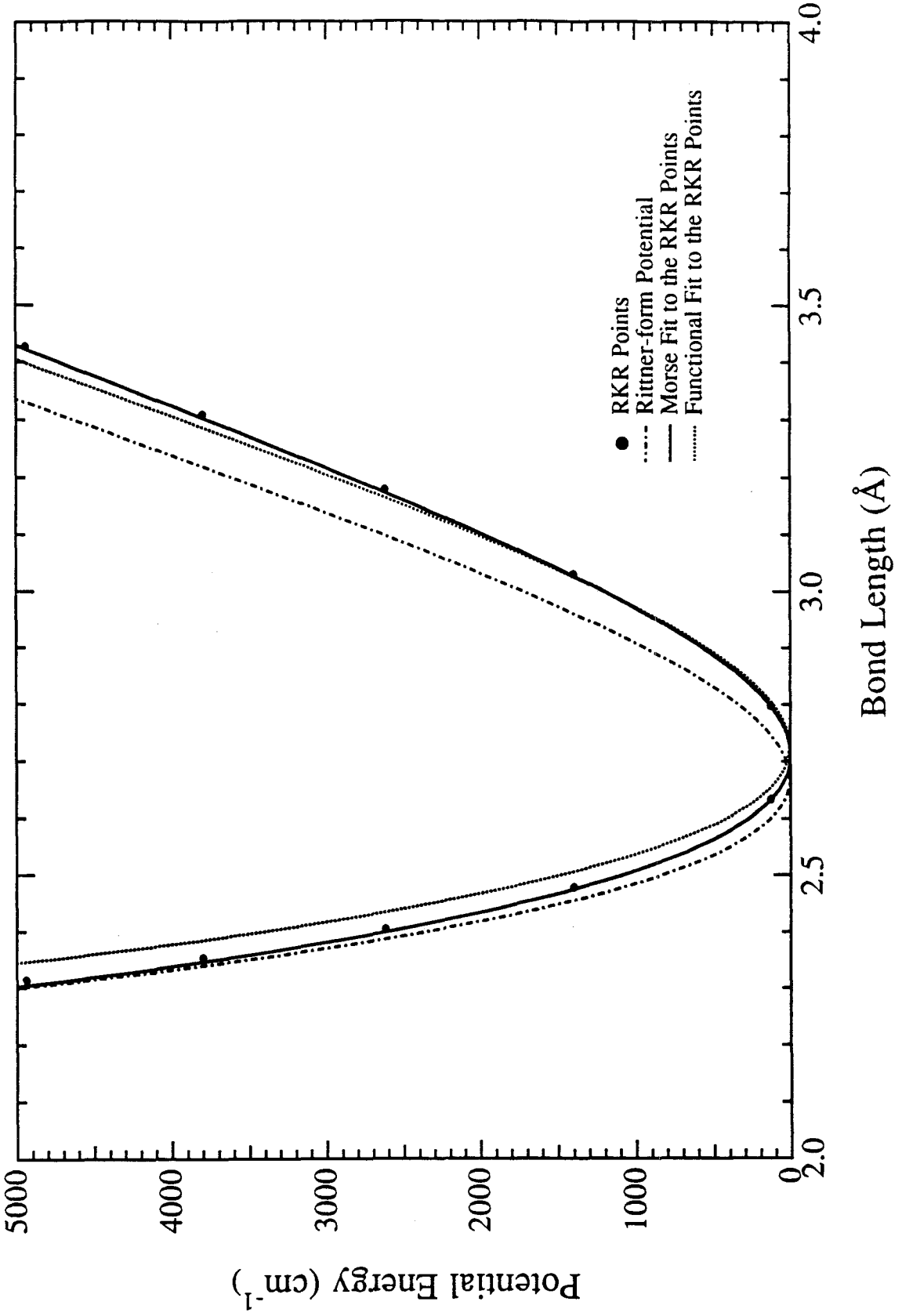
Potential Energy (cm-1)
5000
4000
3000
2000
1000
0
2.0
2.5
3.0
3.5
4.0
Bond Length (Å)
RKR Points
Rittner-form Potential
Morse Fit to the RKR Points
Functional Fit to the RKR Points

Figure 4.8

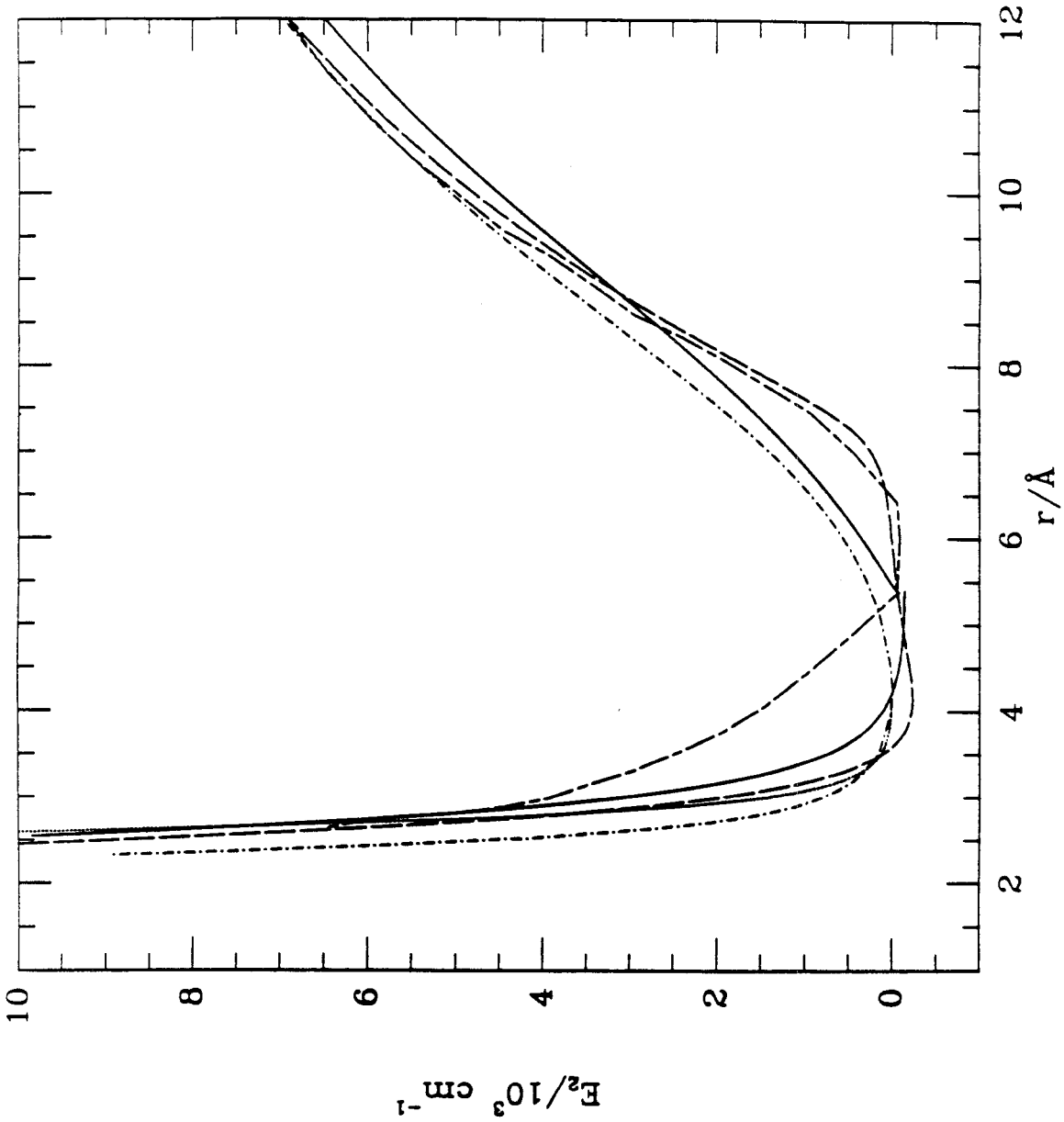

Figure 4.9

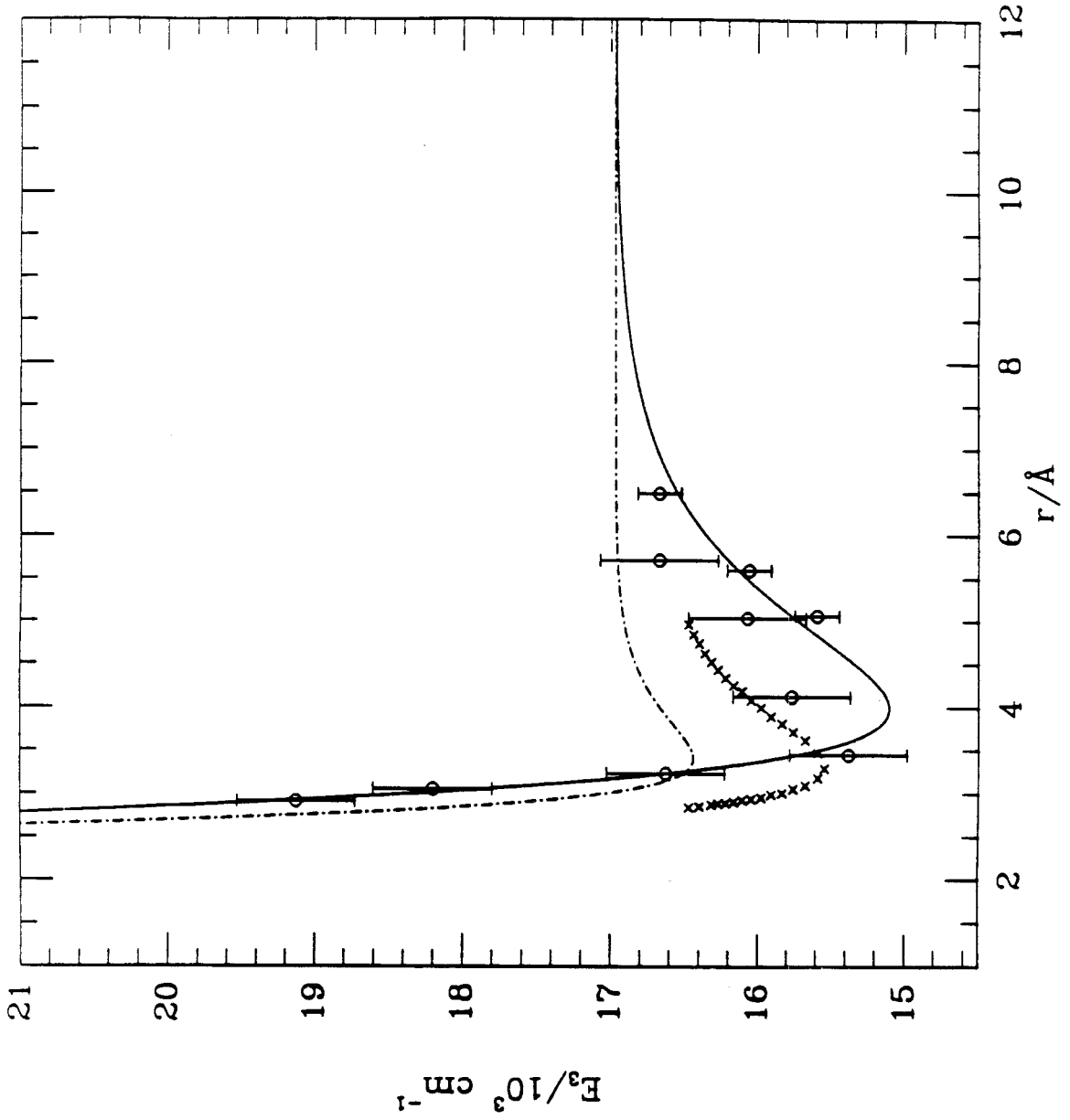

Figure 4.10

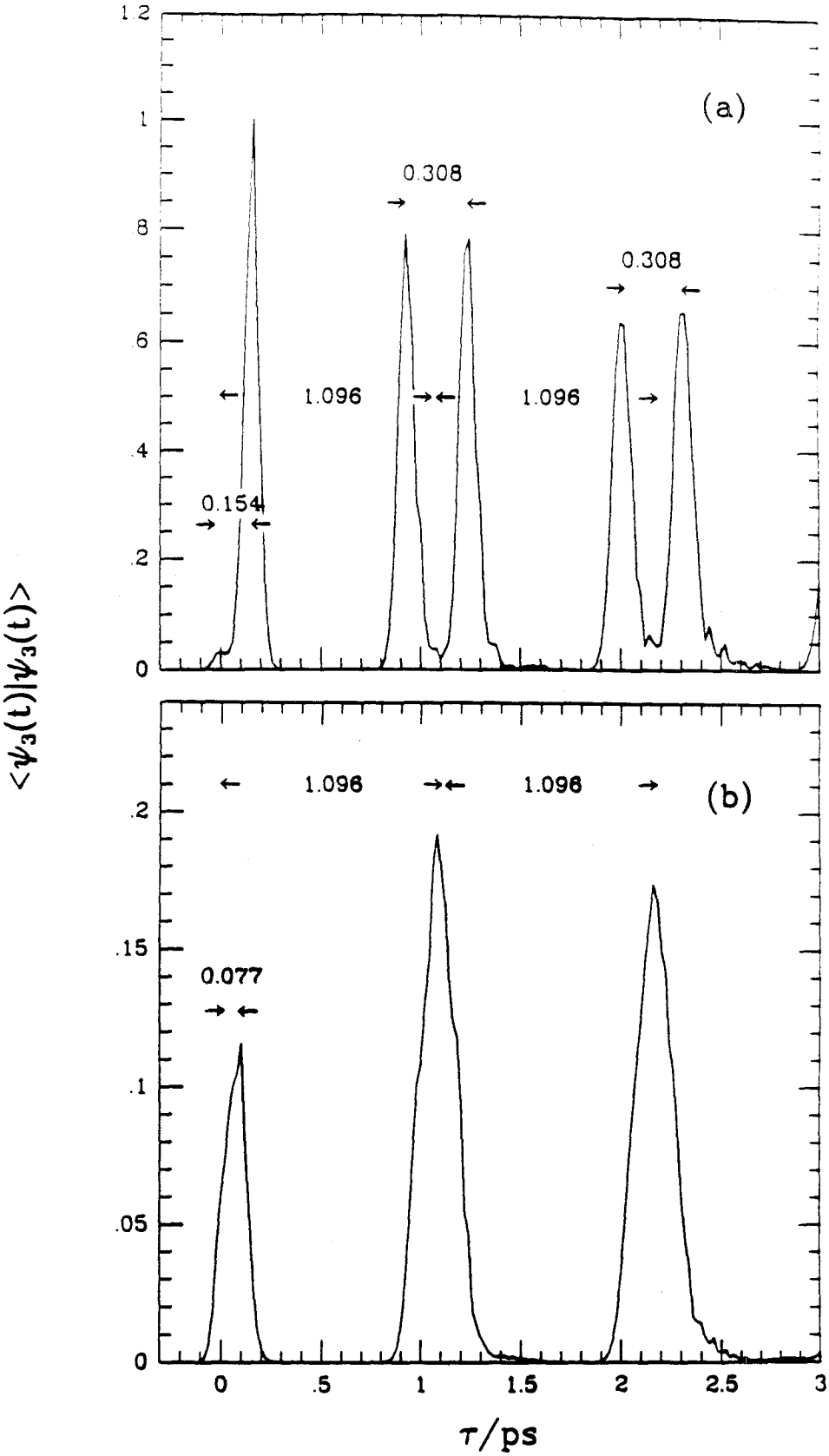
(a)
0.308
0.308
1.096
1.096
0.154
(b)
1.096
1.096
0.077
$\langle\psi_3(t)|\psi_3(t)\rangle$
τ/ps

Figure 4.11

Chapter 5

Long-Time Behavior of Wave-Packet Motion in the Dissociative Reaction of NaI

I. Introduction

In the last two chapters, real-time dynamics of the wave packet motion in the dissociative reaction of NaI were considered in detail. The timescale involved was from 100 fs to 10 ps, in which a number of important aspects of the wave-packet dynamics were discussed, including dephasing, population decay induced by the Landau-Zener curve crossing, and the coupling matrix element in Chapter 3, and direct inversion to the relevant potentials in chapter 4.

In this chapter, the main focus will be shifted to the long-time behavior of the wave-packet motion in the predissociation reaction of NaI $\rightarrow$ Na + I. By "long time," the timescale of interest is up to 40 ps; in other words, the long-time behavior refers to the wave-packet dynamics after many oscillations, as opposed to only the first few oscillations considered in two previous chapters. As will be seen in the following sections, there are some unique and interesting features of the wave-packet dynamics on this timescale that were neither anticipated, nor easily explainable.

The remainder of this chapter is organized as follows: The next section presents experimental observations on the long-time behavior of the wave-packet dynamics, followed by discussions about the possible mechanisms that are responsible. This chapter is summarized in the last section.

II. Experimental Results

The experimental setup for observing the long-time dynamics of wave-packet evolution was identical with the arrangement described in Chapter 3. The only differences

in procedure were that a typical transient considered in this chapter covered about 40 ps delay time compared to about 10 ps as discussed in Chapter 3, and 4 ps in Chapter 4, since the long time dynamics were the main focus here; longer averaging times were also required in order to obtain a very high signal-to-noise ratio as needed in the FTS transients, since much of the signal has decayed at such long delay time.

Figure 5.1 shows the experimental transient with a pump wavelength of 310 nm and a probe wavelength of 620 nm. As can be seen from the upper panel of this figure, the quantum-beat pattern (periodic oscillations) exhibits a prominent recurrence feature around 30 ps. The lower panel shows an augmented version of those recurrence peaks. The observation of this interesting feature has been previously published, along with a simple, preliminary theoretical model.[1] Chapman and Child presented a more elaborate semiclassical model to explain this recurrence.[2] More recently, Meier, Engel, and Briggs addressed the recurrence problem by a fully quantum-dynamical method.[3] Even though the calculations carried out by these workers differed in many ways, the underlying physical principles and the main conclusions were essentially the same (see later).

Since the publication of Ref. 1, more experiments have been carried out to explore the effects various experimental parameters may have on the long-time recurrence behavior. In this section, a complete account of the new experimental observations of these long-time recurrences is given, including power dependence, polarization dependence, and pump wavelength dependence. The theoretical aspects of this work, especially the contributions by Chapman and Child[2] and by Meier, Engel, and Briggs[3] are deferred to the next section.

At the pump/probe combination of 310 nm and 620 nm, the power of the pump and probe beams was varied by a factor of 10; no appreciable change in the waveform of the long time transient was observed. From this observation, we can conclude that the

recurrence is not caused by non-linear optical processes like Rabi-cycling or multiphoton absorption. Furthermore, the polarization of the pump and probe beams was also varied such that the polarization directions of pump and probe beams were either parallel or perpendicular to each other, no discernible change in the overall waveform and the phase of the recurrence peaks was observed either. Thus, the recurrence is not due to rotational alignment.[4]

While the probe wavelength was fixed at 620 nm, the pump wavelength was varied from 295 nm to 330 nm. The corresponding transients are displayed in Figures 5.2 and 5.3. At 330 nm or longer wavelength, the oscillations in the transients decay smoothly and recurrences are essentially absent. At 325 nm, a group of weak recurrence peaks appeared, centered around 30 ps. When the wavelength was further tuned to the blue to 321 nm, the transient had very strong recurrence peaks, and there is only a "node" between the recurrence oscillations and the early decaying oscillations. It is interesting to note that the overall envelope of the recurrence peaks is symmetric; it becomes noticeable around 20 ps, grows in gradually and reaches a maximum around 30 ps; after 40 ps, it becomes unnoticeable again.

When the wavelength is tuned to an even shorter wavelength than 321 nm, the recurrence peaks are always present. However, the relatively "flat "region between the first group of decaying oscillations and the second group of recurrence oscillations increased as the pump wavelength was decreased. When a close inspection is focused on the "flat" region, it turns out to be rather chaotic around both end regions that are neighboring the two groups of periodic oscillations; while the middle part displays an oscillation of very small amplitude, the frequency of this oscillation is exactly twice of the fundamental frequency. The overall envelope of the recurrence signal remained symmetric; its number of peaks was approximately twice the number of the initial damped oscillations.

To demonstrate the effects of fine-tuning the pump wavelength, Figure 5.4 shows three transients with pump wavelengths 1 nm apart, centered around 321 nm. As can be seen from this figure, the recurrence peaks are present in all the transients, and the overall appearances of the transients are quite similar. This will be a critical test in evaluating the merits of different theoretical models.

III. Discussions

Recurrences of wave-packet evolutions have been observed experimentally in bound molecular systems[5] as well as in atomic systems (Rydberg wave packets)[6] previously. The origins of these recurrences (or "revivals," as called by physicists[6]) are the anharmonicities in the eigen-energy spectrum. Consider a Morse oscillator as an example, if a coherent vibrational wave packet is formed in the bound Morse potential with its energy spread covering a number of vibrational eigenstates, its wave function can be expressed as a superposition of vibrational eigenstates:

$$\Psi(R,t) = \sum_n A_n \Phi_n(R) exp(-i2\pi E_n t/h), \qquad (5.1)$$

where R is the displacement coordinate, $\Phi_n(R)$ is the nth vibrational eigenfunction with E_n being its energy eigenvalue, and A_n is the amplitude that is determined by the preparation process, *i.e.*, transition dipole moment and laser spectral profile. Initially, all the frequency components are in phase, so the wave packet will oscillate from one turning point to the other with a period T determined by the average energy spacing of vibrational eigenstates that compose the wave packet, where T equals the inverse of the average frequency spacing v ($T = 1/v$, $v_n = dE_n/dn$). However, the vibrational spacing in a Morse potential well is not uniform because of the anharmonicity; thus, the wave packet will become more and more

delocalized when the different frequency components gradually get out of phase with each other. When $t = \Delta T/2$, the spread of the wave packet will reach a maximum, where ΔT is the inverse of the anharmonicity constant, *i.e.*, the difference in the vibrational spacings ($\Delta T = 1/\Delta v$, $\Delta v_n = d^2E_n/dn^2$). In contrast, when $t = \Delta T$, all the frequency components will be in phase again, just as when $t = 0$. Thus, the wave packet in a Morse potential goes through a complete dephasing and rephasing process when a time ΔT elapses. The revival time for the atomic Rydberg wave packet can be treated similarly by considering its energy spectrum.[6]

For the NaI case in hand, the situation is much more complex. The recurrence time as predicted by the anharmonicity would be about 300 ps, which is 10 times longer than the experimentally observed time.[1] Rotational recurrence time for NaI in the excited covalent state is about 700 ps, not to mention the insensitivity of the recurrences peaks to the relative polarizations of the pump and probe pulses, ruling out the possibility of rotational alignment causing the recurrences.[1]

The key to understanding the origins of the recurrences in the photodissociation of NaI, we believe, is to recognize the fact that the covalent state of NaI is neither completely bound nor dissociative; rather, it is predissociative. The eigenstates of such a system have finite, oscillatory lifetimes, as has been discussed in Chapter 2. To reflect this fact, Eq. (5.1) must be modified to include lifetime factors besides the purely imaginary phase factors:

$$\Psi(R,t) = \sum_n A_n \Phi_n(R) \exp(-\Gamma_n t/2) \exp(-2\pi\imath E_n t/h), \qquad (5.2)$$

where Γ_n is the lifetime of the nth eigenstate. With these ideas in mind, we simulated the experimental transient with the following equation[1]:

$$S(t) = \int_{R_1}^{R_2} |\Psi(R,t)|^2 g(R) dR, \qquad (5.3)$$

where $g(R)$ represents the "window" opened by the probe pulse and it is taken to be a Gaussian with a width of about 0.5 Å. Γ_n needed for this calculation was obtained from Ref. 7, while the eigenfunctions were obtained by solving the one-dimensional Schroedinger equation with the potential parameters listed in Ref. 11 (see Table 2.3) via a Numerov-integration routine.[8] Figure 5.5 summarizes the results from this theoretical simulation. The physics behind figure 5.5 is quite simple; the initial pump pulse prepares a wave packet that covers two sets of long-lived states spaced about 10 eigen levels, after about 10 ps, the short-lived states have essentially decayed into free atoms, while the two groups of long-lived states interfere with each other. Since the vibrational-spacing difference between these two sets of long-lived states is about 1 cm^{-1} (10 x 0.1 cm^{-1} = 1 cm^{-1}), the recurrence signal will occur at the inverse of 1 cm^{-1}, *i.e.*, ~ 30 ps. Another factor considered in this simulation is the initial Boltzmann distribution of ground-state vibrational levels. The upper panel of Fig. 5.5 shows the result of Boltzmann averaging.

Despite the apparent success of this intuitively logical model, it *cannot* explain the pump wavelength dependence of recurrence signals. On the basis of this model, the recurrence peaks will be observed only when the pump pulse covers two groups of long-lived states with equal weights. If the wavelength is detuned by half of the spectral width of the femtosecond pulse, the recurrence will disappear. Since we do not have *a priori* knowledge about location of long lived states, it seems to suggest that the fact that we observe recurrence signal is purely accidental. However, as Figure 5.3 shows, when the wavelength is detuned ± 1 nm from 321 nm, the transients are essentially indistinguishable from that seen at 321 nm. Another deficiency in this treatment was that only the vibrational lifetimes for rotationless molecules was considered; the rotational Boltzmann distributions were totally ignored. Child and his coworkers have pointed out that in a curve-crossing

system, the lifetime varies with the rotational quantum number for the same vibrational state.[10] Since the essence of the theory proposed in Ref. 1 is about the distribution of lifetimes, it is certainly not appropriate to represent the lifetimes of many rotational states that belong to the same vibrational state by only one of their members, while the lifetime is a sensitive function of the rotational quantum number.

To explain the recurrence in the predissociation of NaI, Chapman and Child adopted a semiclassical treatment in which rotational distributions were considered explicitly. The basic physics involved in this theoretical work is very similar to the one discussed in Ref. 1, namely, the inhomogeneous lifetime distribution as a result of the interaction between the two diabatic electronic states. These workers employed a simpler approach to simulate the FTS transient than Ref. 1, the autocorrelation function of the time-dependent wavefunction that composes of a superposition of vibrational eigenstates; *i.e.*:

$$S(t) = |\langle \Psi(R, t)|\Psi(R,0)\rangle|^2 = \sum_{j,k} |A_j|^2 |A_k|^2 \cos(2\pi(E_j - E_k)t/h), \qquad (5.3)$$

where the decay-time constants are contained in the coefficients A_j and A_k. By this method, the FTS signal $S(t)$ is represented by the overlap integral between the time-dependent wavefunction and the wavefunction at time $t = 0$ (assuming that the vibrational eigenfunctions are orthonormal). This is equivalent to probing the wave-packet motion by monitoring at the position of its initial preparation. In the actual experiment, the probe "window" is located at longer r and the width is much broader; thus, the transients simulated via this method may be shifted to earlier time and the peaks may be sharper than the experimentally observed ones, but the overall characteristics of the experimental transients like the oscillation period and Landau-Zener decay are faithfully reproduced.[2] Even though the spatial dependence of the probe window is oversimplified, the efficiency

gained in computing time outweighs the minor inaccuracies that it introduces.

Chapman and Child[2] computed the individual rovibrational linewidths through the semiclassical theory developed by Child and coworkers[10] with the potential parameters listed in Ref. 11 (see Table 2.3 in this thesis) and with hybrid-RKR potentials based on the spectroscopic data reported by Tiemann and coworkers.[7] Then, these workers investigated the effects of the pump-pulse wavelength and spectral width (*i.e.*, pulse duration) on the time dependence of the wave-packet propagation, which is described by Eq. (5.3). The conclusion they reached was that in order to observe long-time recurrence, the pump wavelength had to be centered around one group of short-lived states, and its width was such that it would cover two sets of long-lived states. Chapman and Child also considered the effects of rotational distribution by selectively averaging over the initial Boltzmann distribution (T = 650 °C) with j = 0, 10, ... 120. What they found was that the recurrence time was shifted to ~ 20 ps from ~ 30 ps after such averaging, for both the potential cited by Ref. 11 and the hybrid-RKR potential they derived (see Fig. 11 and Fig. 14 in Ref. 2).

Besides the same problem as faced by Ref. 1, *i.e.*, that the wavelength dependence was too sensitive, the results from selective Boltzmann averaging raise two questions: One is why the recurrence time is shifted; the other is whether the recurrence signal will survive a complete Boltzmann averaging.

Very recently, Meier, Engel, and Briggs[3] addressed this recurrence problem with a time-dependent quantal dynamical calculation. The methodology is very close to the approach described in the previous chapter in spirit, except that these workers replaced the probe process by the method employed in Ref. 1, namely, it is represented by a Guassian window centered around 2.7 Å with a width of ~ 0.5 Å. With the split-operator algorithm, these workers were able to propagate the wave packet for as long as 60 ps. By using the same potential parameters as in Ref. 11, they found that for a 60 fs pump pulse with a

wavelength of 311 nm, the wave packet partially rephases at ~ 25 ps; however, if the wavelength is tuned to 310 nm, the simulated signal decays much more slowly and exhibits no recurrence behavior (see Ref. 3, Fig. 3). When a close inspection of the asymptotic energy spectra of the wave packets pumped by 310 nm and 311 nm was taken after a time delay of 14 ps from the initial preparation, it was revealed that the wave packet prepared by the 311 nm pulse centered around one group of short-lived states, while the one initiated by the 310 nm pulse centered around one group of long-lived states, resulting in its slower decay rate (see Ref. 3, Figs. 4 & 5). When a different set of potential parameters[12] was utilized, they found that a strong recurrence feature appeared around 30 ps for a pump wavelength of 310 nm (see Ref. 3, Fig. 10), contrary to the lack of a recurrence signal found for the previous potential, even though the transients were very similar for the first 10 ps. This demonstrated an interesting point, that fine details of a potential could have profound impact on the subtle details of the wave-packet motion, like the long-time recurrence behavior. Boltzmann averaging was also considered for the initial thermal distribution of vibrational states; the result seemed to suggest that recurrence occurred only for $v'' = 1$, and the thermal averaging diminished the overall recurrence signal (see Ref. 3, Fig. 9). Even though no new results were obtained in this work beyond what had been learned in Refs. 1 & 2, this rigorous and fully quantal treatment does give us more confidence in the validity of the simple models developed before.[1,2] It would be very informative if the same calculations could be performed for different rotational states and rotational Boltzmann averaging were carried out. However, the cost of CPU time required for such calculations may prove to be prohibitively high.

To further address this long-time recurrence problem and to answer the questions remaining from Refs. 1-3, the approach developed by Chapman and Child is followed in this chapter because it reasonably reproduces the essential features (oscillation and decay) of the experimental transients, and its demand for CPU time is rather modest. First, the

vibrational eigenstates are solved for both the bound diabatic potential well and the adiabatic one, with energy ranging from 2500 cm-^{1} to 8500 cm^{-1} above the covalent atomic limit.[8] Rotational energy is taken into account by adding a term $h^2J(J+1)/8\pi^2\mu r^2$ to both the potentials and solving the one-dimensional Schroedinger equation for each J level, with J ranging from 0 to 130 to cover the thermal distribution. Then the lifetime and position of the mixed states are calculated by the method developed by Child and coworkers[10] with the equations outlined in Chapter 2. Finally, the FTS transients are calculated by Eq. (5.3), where the coefficients are taken to be a Gaussian with a FWHM of 300 cm^{-1} to 400 cm^{-1}.

Figure 5.6 shows the vibrational eigen energies for both the diabatic and the adiabatic potentials plotted against J(J+1). As can be seen from this figure, the vibrational states for v" = 262 (diabatic potential) and v' = 153 are very close, and therefore the mixed states would be expected to be long-lived. 310 cm^{-1} above this group of long-lived states, there exists another set of coincident states, with v" = 270 and v' = 162. In general, the long-lived states and the short-lived states followed each other in an almost periodic pattern while climbing up the energy ladder.

No Rotational Averaging

When the excitation energy is set to 30426 cm^{-1} with a FWHM of 400 cm^{-1} for a single rotational level (J = 40), the simualted transient is presented in Figure 5.7. Clearly, a recurrence feature appears at ~ 25 ps. The high-frequency modulations on the recurrence peaks are an indication of the partial revival phenomenon[6] and were also present in the semiclassical[2] and quantal simulations.[3] The temporal resolution is ~ 100 fs in the FTS experiments; therefore, these high-frequency oscillations are not expected to be observed experimentally.

Selective Rotational Averaging

Figure 5.8 displays the transient after selective rotational averaging (J = 0, 10, ··· , 120); the recurrence feature remains clearly visible, though the relative amplitude is smaller than for a transient from a single rotational level. This is in agreement with the result obtained by Chapman and Child.[2] Furthermore, the simulated transient obtained here is more robust to the rotational averaging than the one given by Ref. 2, its maximum stays around ~ 25 ps, unshifted from the recurrence time for a transient from a single rotational level.

Complete Rotational Averaging

The complete rotational averaging is obtained by summing all the rotational states with their respective Boltzmann weights. The transient is shown in Figure 5.9, with its recurrence oscillations still centered around 25 ps and its high frequency modulations completely averaged out. This is an important result in the sense that it establishes that the recurrence from single rotational levels can survive the rotational averaging, though maybe under the most favorable conditions, despite the fact that the vibrational spacing varies from one rotational state to the other, as is induced by the centrifugal effect.

When the pump energy is detuned by only 100 cm^{-1} from 30426 cm^{-1}, however, the simulated transient exhibits a series of smooth, damped oscillations; the recurrence feature is clearly absent. Thus, this model is still not able to explain the wavelength dependence of the recurrence signals as observed experimentally, even though it shows remarkable robustness towards rotational thermal averaging.

To explore the effects that a different set of energy levels may have on the simulated transients, the energy levels of the adiabatic and diabatic potentials are calculated with the Dunham parameters given in Ref. 7. Once again, the recurrence features are present in the simulated transients under only some special conditions; a pump wavelength chosen

without *a priori* knowledge of the eigen energy structure normally does not produce any recurrence signal in the calculated transient (see Figure 5.11).

Vibrational Averaging

Figure 5.12 shows the effects of vibrational Boltzmann averaging at 320 nm, where the recurrence signal was the strongest experimentally. The calculation was carried out with potentials cited in Ref. 11, and the Franck-Condon factors for v" = 0, 1, and 2 were obtained by the same Condon reflection method as described in Chapter 4. Contrary to the results obtained in Ref. 1 (Fig. 5.5), recurrence features are definitely absent in this simulated FTS transient. The reason for the discrepancy was that in the calculation performed in Ref. 1, the recurrences were already present in the individual vibrational component; thus, the Boltzmann averaging could only enhance the recurrences; on the other hand, recurrences were absent from each of the transients from the vibrational states in the present calculation; the sum, therefore, did not present any recurrences. It should be noted that if two vibrational components have the same weight (combining the Boltzmann and the Franck-Condon factors), the sum will show recurrence features, since they are spaced by ~ 260 cm^{-1}; the frequency-spacing difference between the two components will be about 1 cm^{-1} so that the recurrence signal will appear around 30 ps. However, this requirement is too stringent to explain the wide spectral range in which recurrence signals were observed.

IV. Summary

In this chapter, a complete account of the experimental results regarding the long-time behavior of the NaI FTS transients is given for the first time. A number of theoretical approaches have also been discussed and compared. The consensus among all the theoretical models is that the recurrence of the wave-packet propagation must be caused by the special nature of the potentials in which the wave packet evolves. In the case of NaI, the uniqueness of the potentials involved is the non-adiabatic interaction between the

covalent and ionic states, which causes the lifetimes of the eigenstates to oscillate. The semiclassical model is able to display recurrence features in simulated transients despite averaging over a wide thermal distribution of rotational states. However, all the theoretical models developed thus far lack the robustness with respect to pump-wavelength tuning as exhibited by the experimentally observed transients (see Figure 5.4). The oscillation in the lifetimes of eigenstates, which has played a central role in the current theoretical endeavors, therefore, may be only *one* of the causes for the recurrences, not the only reason. The deficiencies in current theoretical models calls for other mechanisms to be sought in order to understand completely the deceivingly simple long-time recurrences in the wave-packet motion of NaI. For example, the contributions to the FTS signal from species other than the NaI monomer, $(NaI)_2$ or $(NaI)_n$, where $n > 2$ may be considered; or the effect of the very high electric field introduced by the intense femtosecond pulses on the position of eigen energy levels, *i.e.*, the dynamic Stark effect, may also be of concern. To explore these seemingly remote possibilities, more experiments will be needed, along with more refined theories. It is hoped that the publication of the experimental results will serve the purpose of stimulating further theoretical interests toward solving this long-time recurrence problem in the FTS experiments of NaI predissociation.

V. References

1. P. Cong, A. Mokhtari, and A. H. Zewail, *Chem. Phys. Lett.* **172**, 109 (1990).
2. S. Chapman and M. S. Child, *J. Phys. Chem.* 95, 578 (1991).
3. Ch. Meier, V. Engel, and J. S. Briggs, preprint.
4. P. M. Felker and A. H. Zewail, *J. Chem. Phys.* 86, 2460 (1987);
   J. S. Baskin, P. M. Felker, and A. H. Zewail, *J. Chem. Phys.* **86**, 2483 (1987).
5. R. M. Bowman, M. Dantus, and A. H. Zewail, *Chem. Phys. Lett.* **166**, 459 (1989);
   M. Dantus, R. M. Bowman, and A. H. Zewail, *Nature* **343**, 737 (1990).
6. J. A. Yeazell, M. Mallalieu, and C. R. Stroud, *Phys. Rev. Lett.* **64**, 2007 (1990);
   J. Parker and C. R. Stroud, *Phys. Rev. Lett.* **56**, 716 (1986);
   I. Sh. Averbukh and N. F. Perelman, *Phys. Lett.* **139 A,** 449 (1989);
   G. Alber and P. Zoller, *Phys. Reports* **199**, 231 (1991).
7. S. H. Schaefer, D. Bender, and E. Tiemann, *Chem. Phys.* **89**, 65 (1984);
   S. H. Schaefer, D. Bender, and E. Tiemann, *Chem. Phys. Lett.* **166**, 273 (1982).
8. R. B. Johnson, *J. Chem. Phys.* **67**, 4086 (1977).
9. See Chapter 4 of this thesis for the location of the probe windows.
10. M. S. Child, in *Semiclassical Methods in Molecular Scattering and Spectroscopy*, ed. M. S. Child, page 127, Reidal, Dordrecht (1980), and references therein.
11. T. S. Rose, M. J. Rosker, and A. H. Zewail, *J. Chem. Phys.* **91**, 7415 (1989).
12. J. Wang, A. J. Blake, D. G. McCoy, and L. Torop, *Chem. Phys. Lett.* **175**, 225 (1990).

VI. Figures

Captions:

Figure 5.1

Experimental FTS transient of NaI over the range from 0 to 40 ps. Adopted from Ref. 1. Top: the transient obtained with a pump wavelength of 310 nm and probe wavelength of 620 nm. Bottom: Modulated part of the experimental FTS transient obtained by subtracting the decay caused by the Landau-Zener leaking of the wave packet. Note that the signal after 10 ps was multiplied by 10 for clarity.

Figure 5.2

Long experimental FTS transients of NaI that show the effect of pump-wavelength tuning. The pump wavelength was tuned from 330 nm to 317 nm, while the probe wavelength was fixed at 620 nm.

Figure 5.3

Continuation of Figure 5.2, with pump wavelength tuned from 310 nm to 294.5 nm. The probe wavelength remained at 620 nm.

Figure 5.4

The effects of pump-wavelength fine-tuning. The experimental transients were taken at 322 nm, 321 nm, and 320 nm. They all exhibited strong recurrences centered around 28 ps.

Figure 5.5

Simulation of the FTS experiment in NaI, using the potential parameters cited in

Ref. 11. Adopted from Ref. 1. The exciting pulse (60 fs) has a spectral width of 250 cm^{-1} around 310 nm. The pulse prepares an initial coherent superposition of the eigenstates in the adiabatic well. The local average vibrational spacing is 27 cm^{-1}. The prepared states have different lifetimes, ranging typically from 1 to 600 ps, as calculated from the spectroscopic data given in Ref. 7. In the packet, the short-lived states decay within 10 ps, while the sets of long-lived states, separated by ~ 270 cm^{-1} (i.e., 10 quantum numbers), are responsible for the rephasing observed around 30 ps. In the top part, the signal is averaged over the thermally populated levels v" = 0, 1, and 2 in the ground state, while in the bottom part the contribution of the single level v" = 0 is given.

Figure 5.6

The eigen values of the diabatic (open squares) and adiabatic (filled squares) states plotted against J(J+1), where J is the rotational quantum number. Please note the close resemblance of this figure with Figure 3 in Ref. 2. The energy scale is shifted up by 100 cm^{-1} in this figure as compared with Figure 3 of Ref. 2, which may be caused by differences in the potential parameters and the algorithms employed in these two independent calculations.

Figure 5.7

The simulated transient for a single rotational level, J =40, with a pump energy of 30426 cm^{-1} and a spectral width of 400 cm^{-1} (FWHM), calculated by Eq. (5.3)

Figure 5.8

The selectively averaged calculated transient with the same pump pulse as in Figure 5.6, sum over J = 0, 10, ··· , 120, with appropriate Boltzmann weighting factors for a sample temperature of 1000 K.

Figure 5.9

The simulated FTS transient after complete thermal averaging (T = 1000 K). The pump-laser pulse centered at 30426 cm^{-1} with FWHM = 400 cm^{-1}.

Figure 5.10

The calculated transient obtained under the same conditions as Figure 5.9, except that the center of the pump pulse is changed to 30326 cm^{-1}. Please note the clear absence of recurrences around 30 ps in this transient.

Figure 5.11

The simulated transient with eigen energies determined by the Dunham parameters reported in Ref. 7. The pump wavelength was 320 nm, with spectral width of 300 cm^{-1} (FWHM). Rotational states from J = 0 to J = 150 were summed together according to their Boltzmann weights at 1000 K.

Figure 5.12

The result of vibrational Boltzmann averaging. The v" = 1 transient was not plotted because its diminishing Franck-Condon factor at 320 nm rendered its contribution to the overall transient negligible. The curves for individual vibrational states were obtained in the same way as for Figure 5.9.

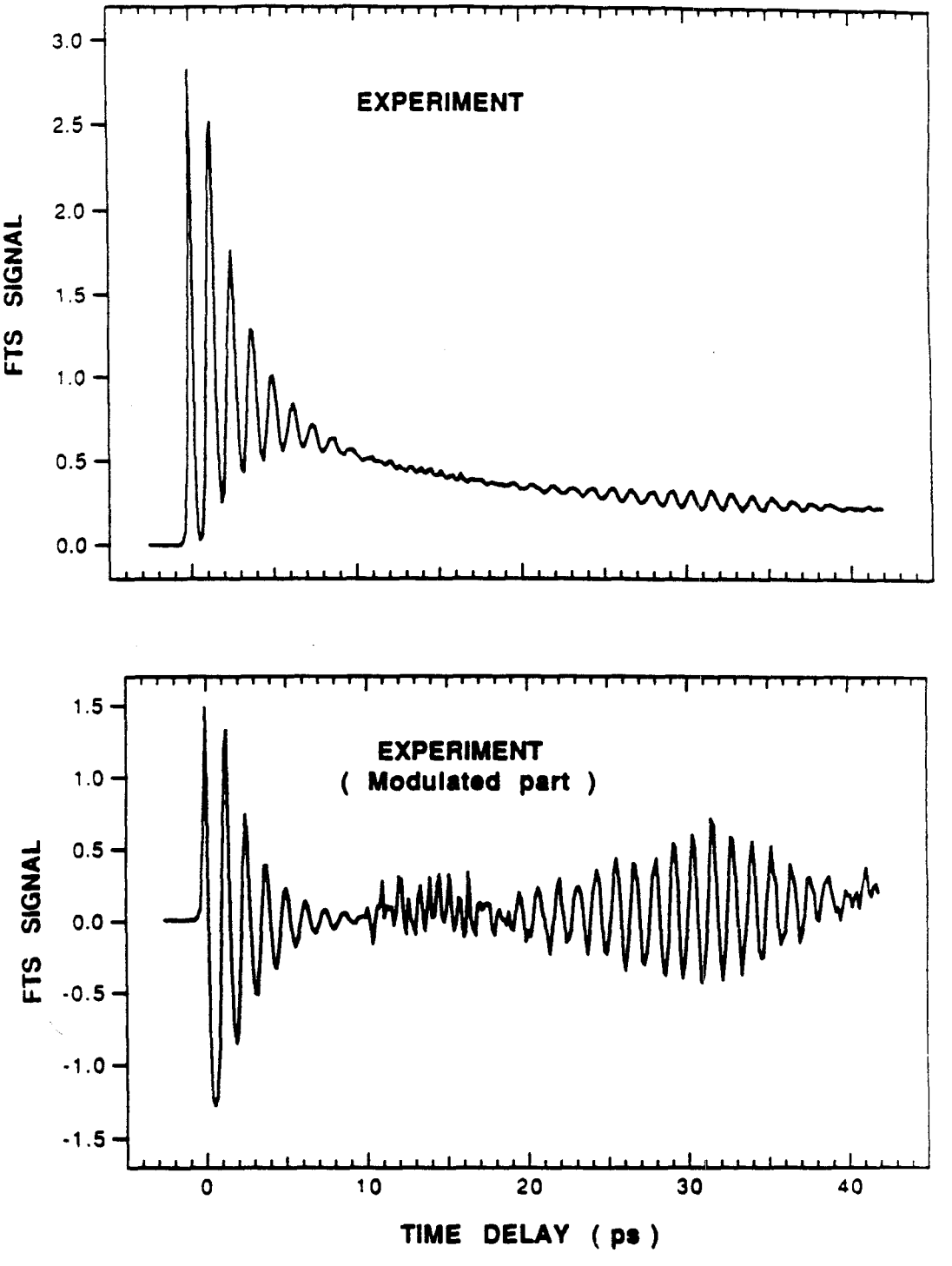
EXPERIMENT
FTS SIGNAL
3.0
2.5
2.0
1.5
1.0
0.5
0.0
EXPERIMENT
(Modulated part)
FTS SIGNAL
1.5
1.0
0.5
0.0
-0.5
-1.0
-1.5
0
10
20
30
40
TIME DELAY (ps)

Figure 5.1

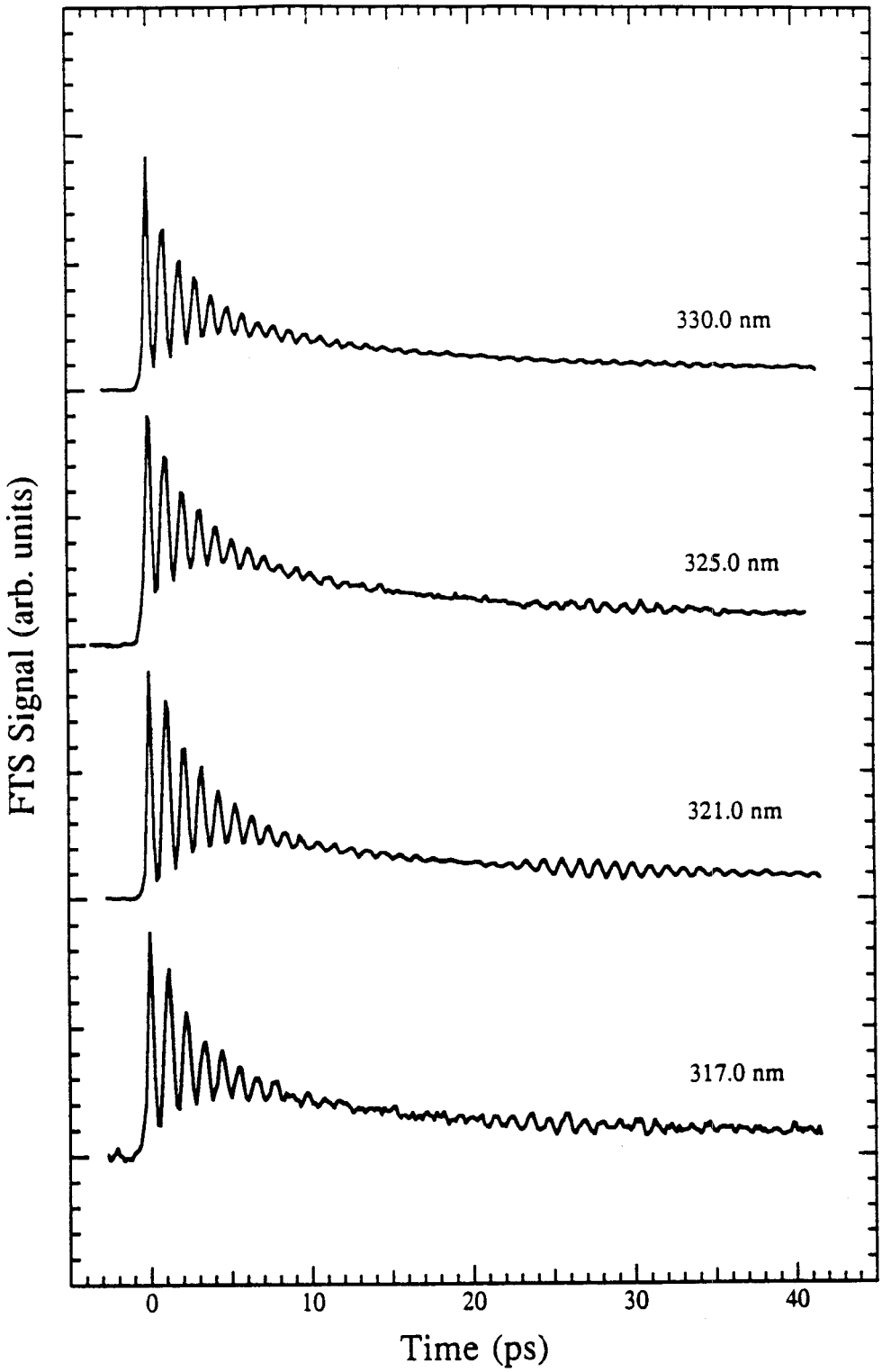
330.0 nm
325.0 nm
321.0 nm
317.0 nm
FTS Signal (arb. units)
0
10
20
30
40
Time (ps)

Figure 5.2

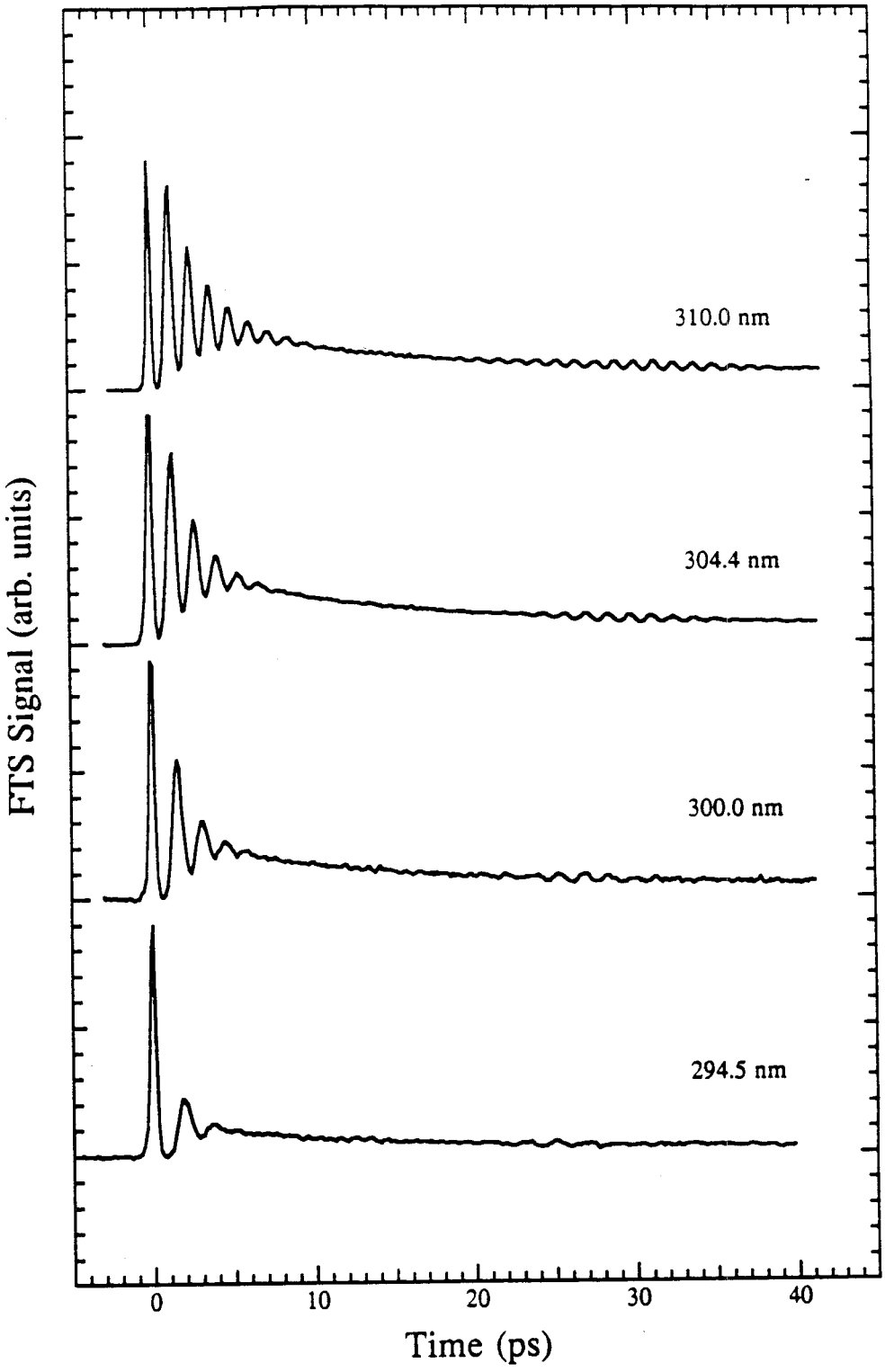
FTS Signal (arb. units)
310.0 nm
304.4 nm
300.0 nm
294.5 nm
0
10
20
30
40
Time (ps)

Figure 5.3

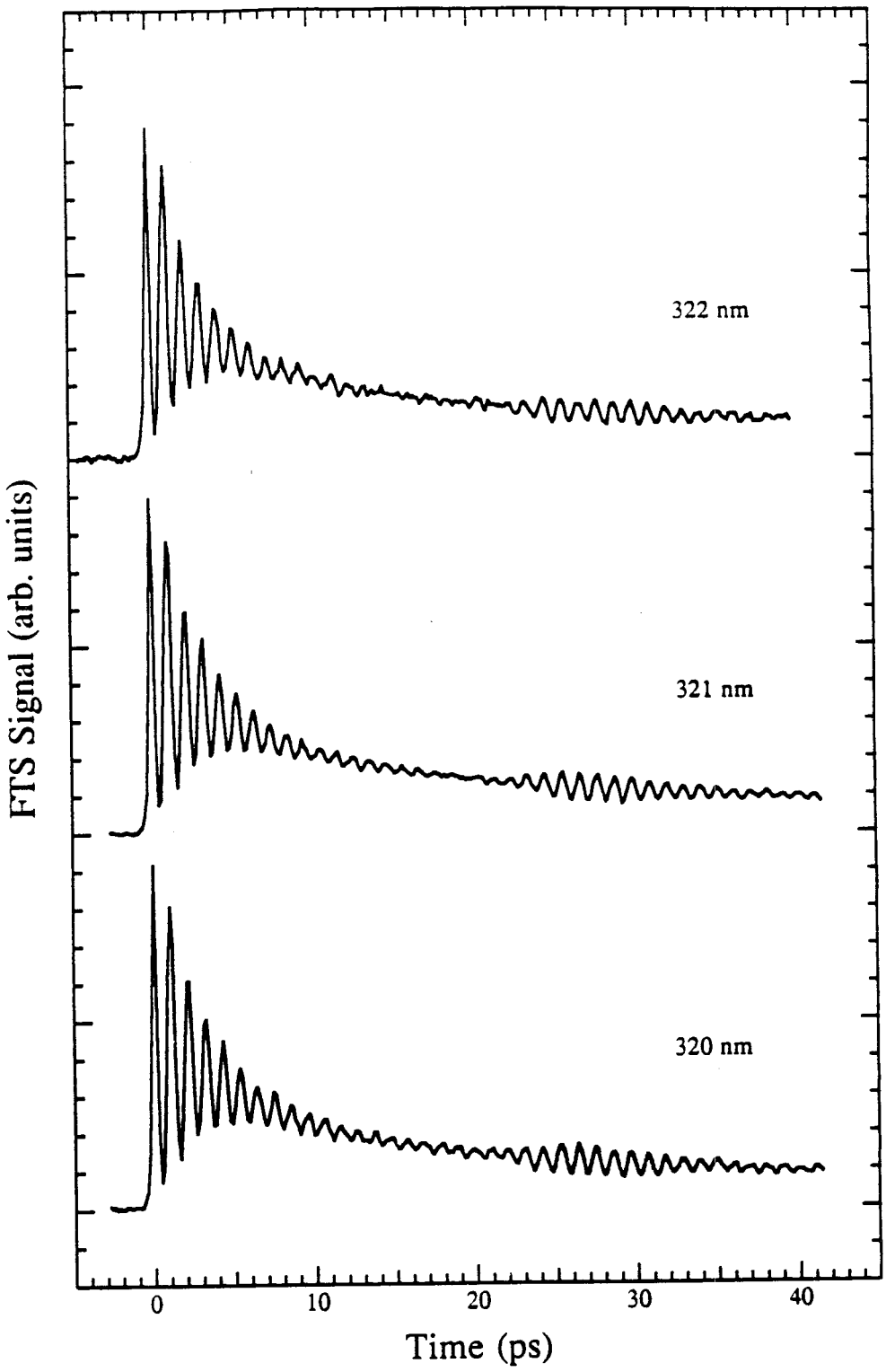

Figure 5.4

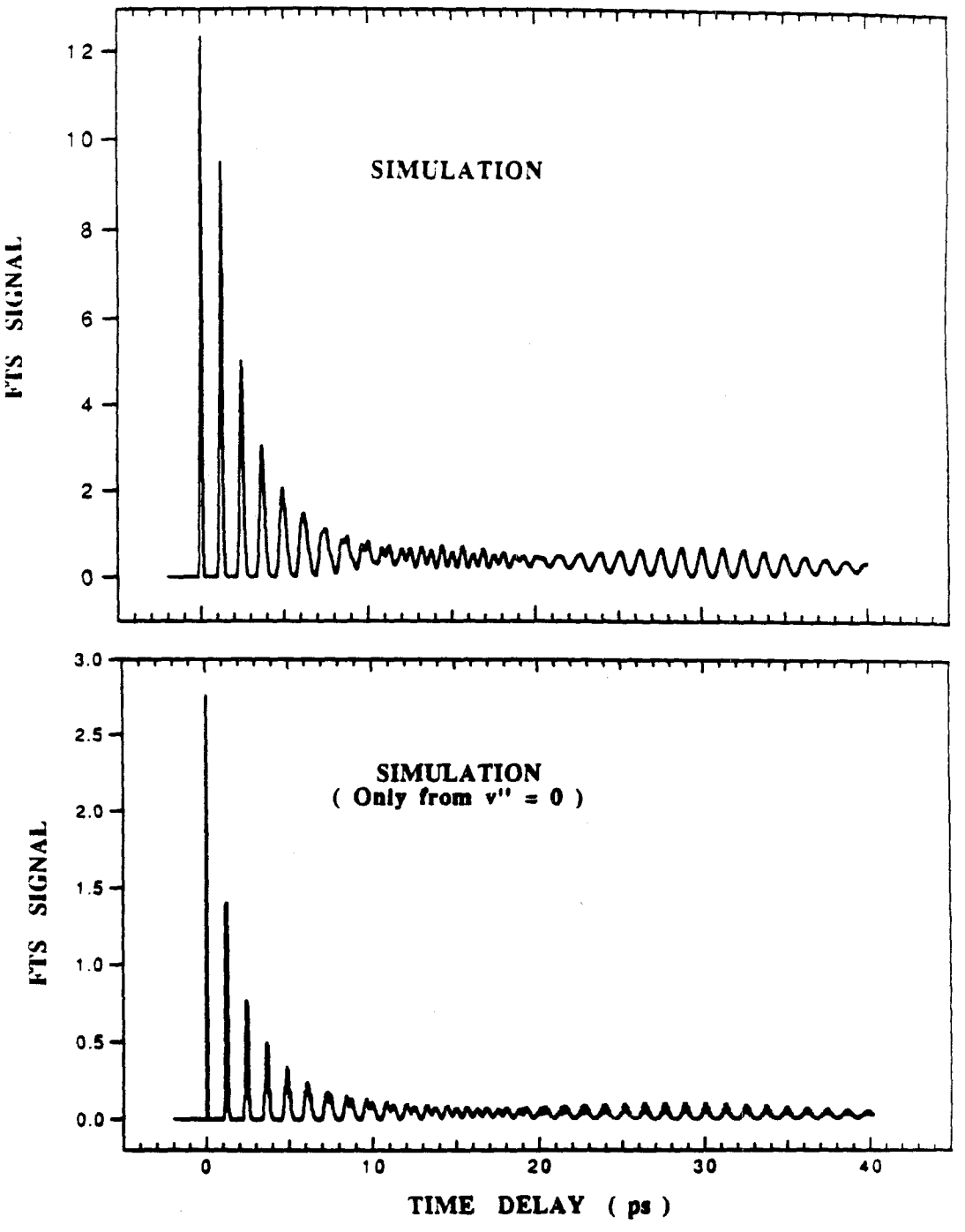
SIMULATION
FTS SIGNAL
12
10
8
6
4
2
0
SIMULATION
(Only from v'' = 0)
FTS SIGNAL
3.0
2.5
2.0
1.5
1.0
0.5
0.0
0
10
20
30
40
TIME DELAY (ps)

Figure 5.5

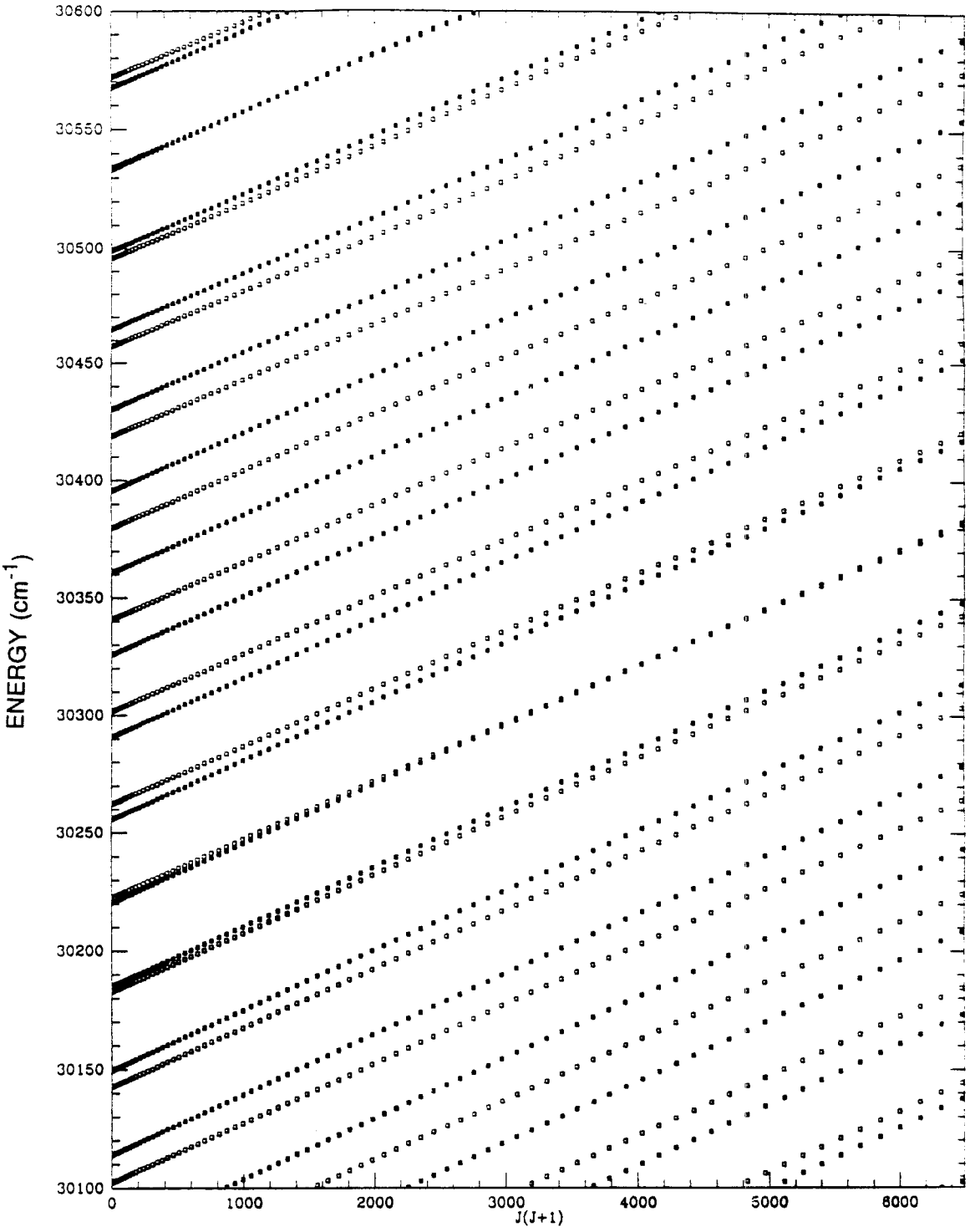
30600
30550
30500
30450
30400
30350
30300
30250
30200
30150
30100
ENERGY (cm-1)
0
1000
2000
3000
4000
5000
6000
J(J+1)

Figure 5.6

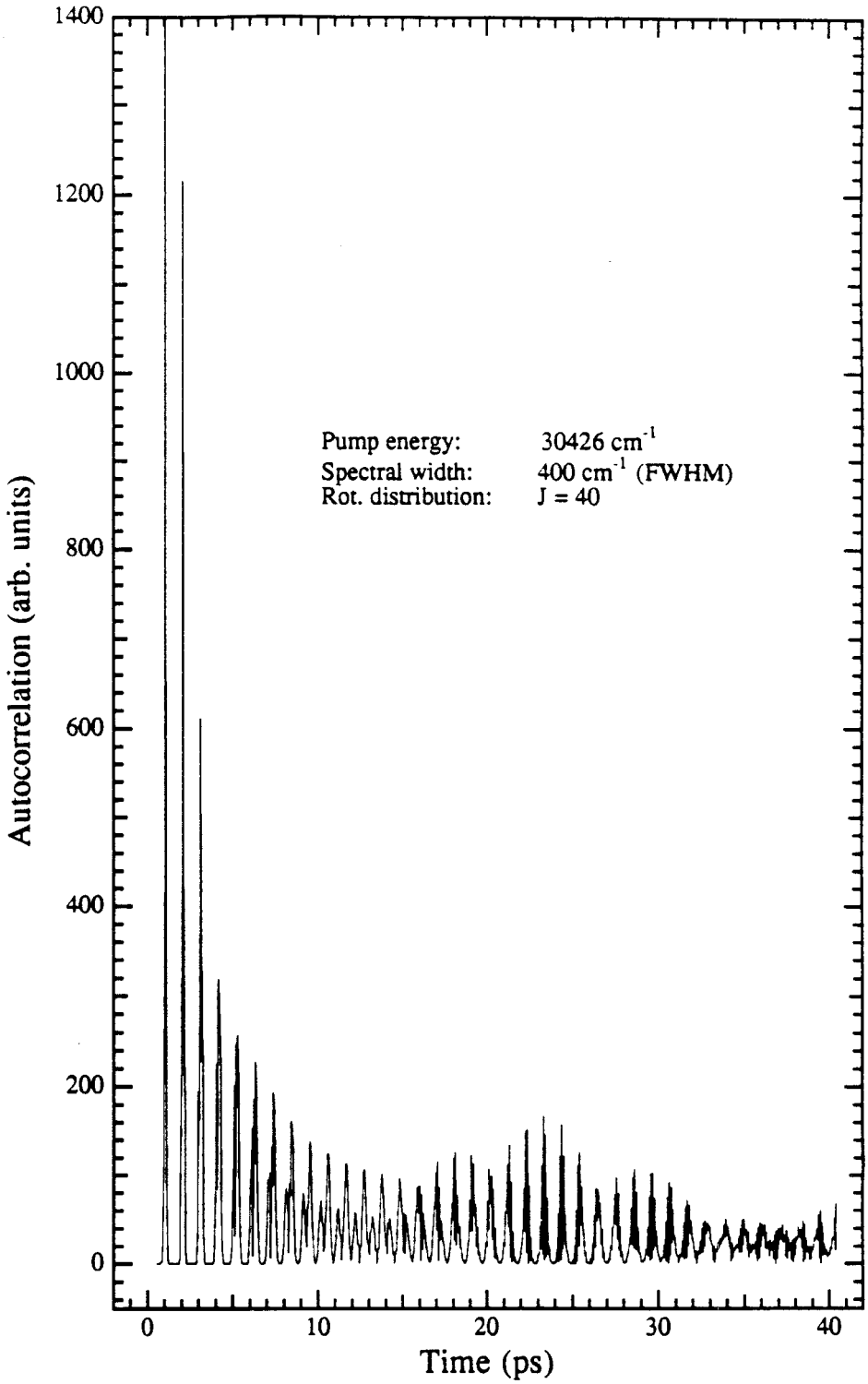
Autocorrelation (arb. units)
Time (ps)
Pump energy: 30426 cm-1
Spectral width: 400 cm-1 (FWHM)
Rot. distribution: J = 40
0
200
400
600
800
1000
1200
1400
0
10
20
30
40

Figure 5.7

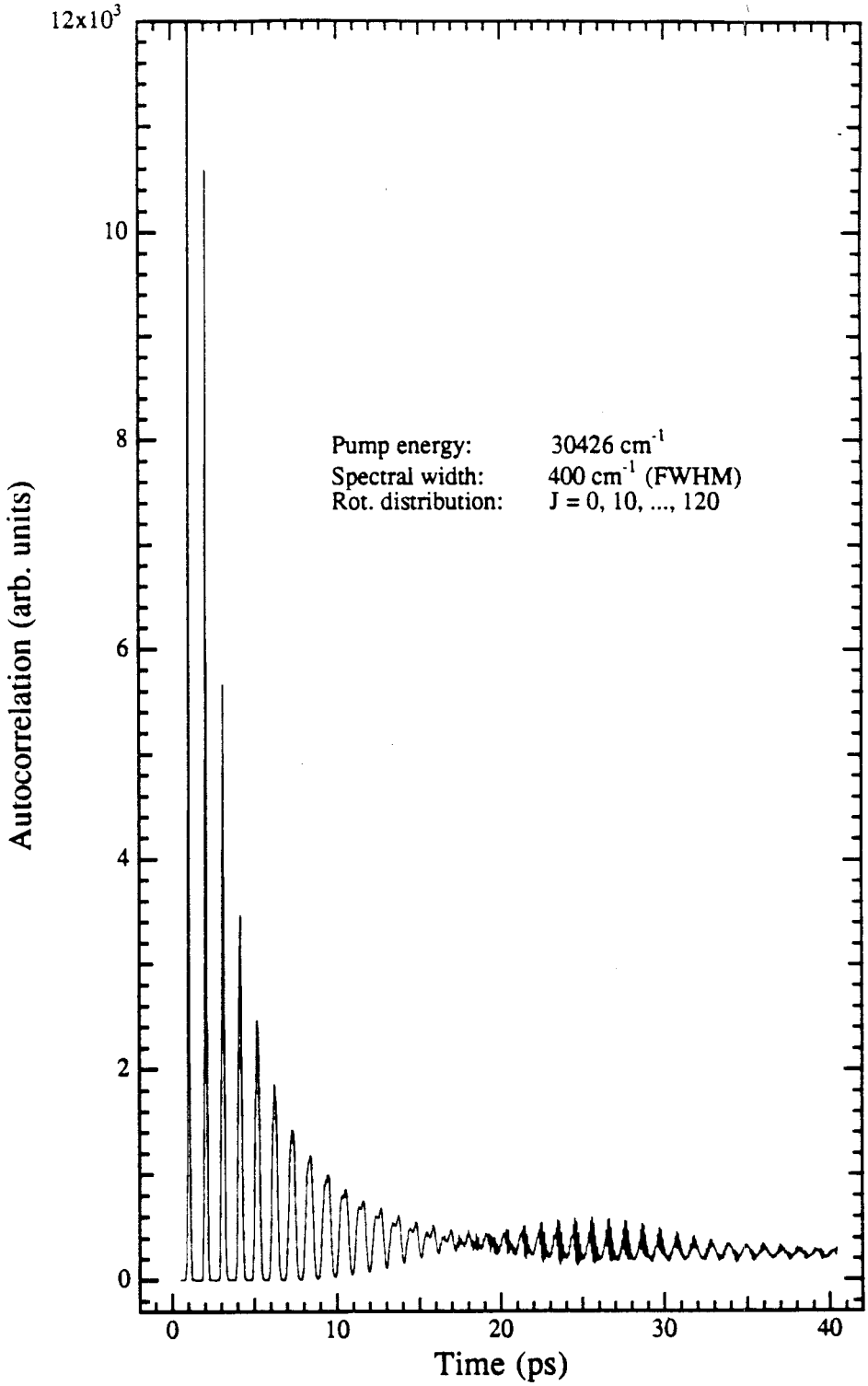
12x10^3
10
8
6
4
2
0
Autocorrelation (arb. units)
Pump energy: 30426 cm^-1
Spectral width: 400 cm^-1 (FWHM)
Rot. distribution: J = 0, 10, ..., 120
0
10
20
30
40
Time (ps)

Figure 5.8

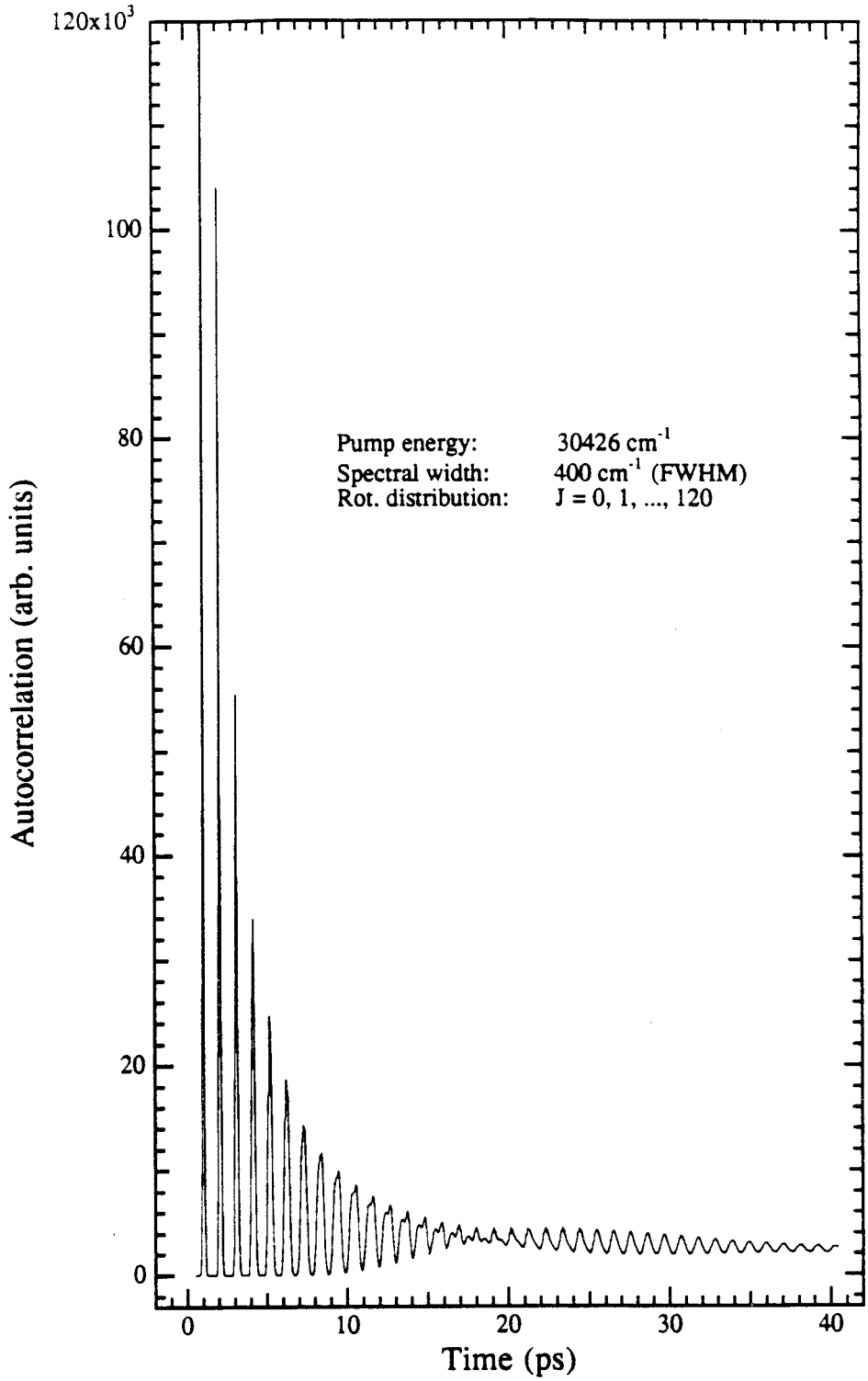
120x10^3
100
80
60
40
20
0
Autocorrelation (arb. units)
Pump energy: 30426 cm^-1
Spectral width: 400 cm^-1 (FWHM)
Rot. distribution: J = 0, 1, ..., 120
0
10
20
30
40
Time (ps)

Figure 5.9

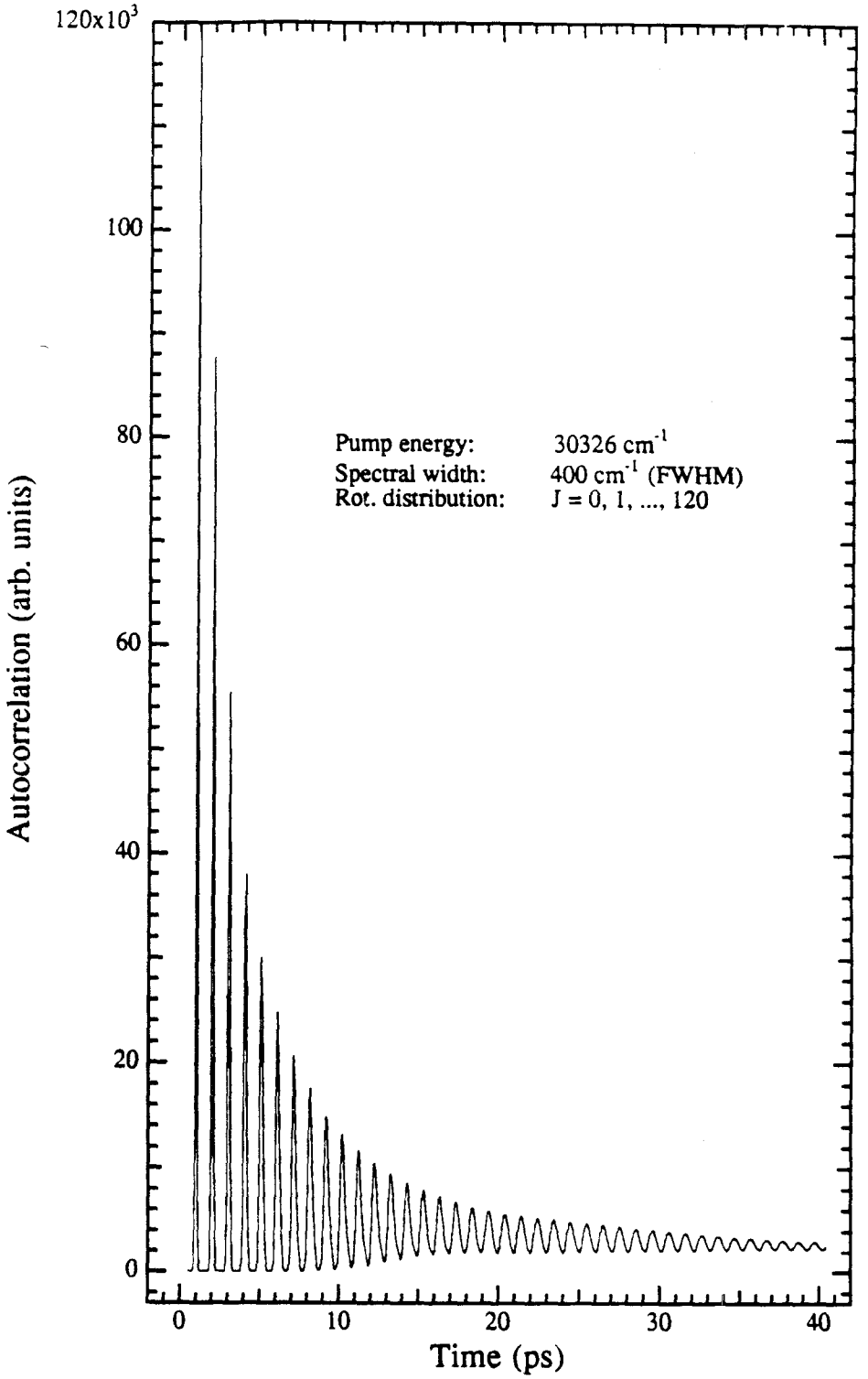
120x10^3
100
80
60
40
20
0
Autocorrelation (arb. units)
Pump energy: 30326 cm-1
Spectral width: 400 cm-1 (FWHM)
Rot. distribution: J = 0, 1, ..., 120
0
10
20
30
40
Time (ps)

Figure 5.10

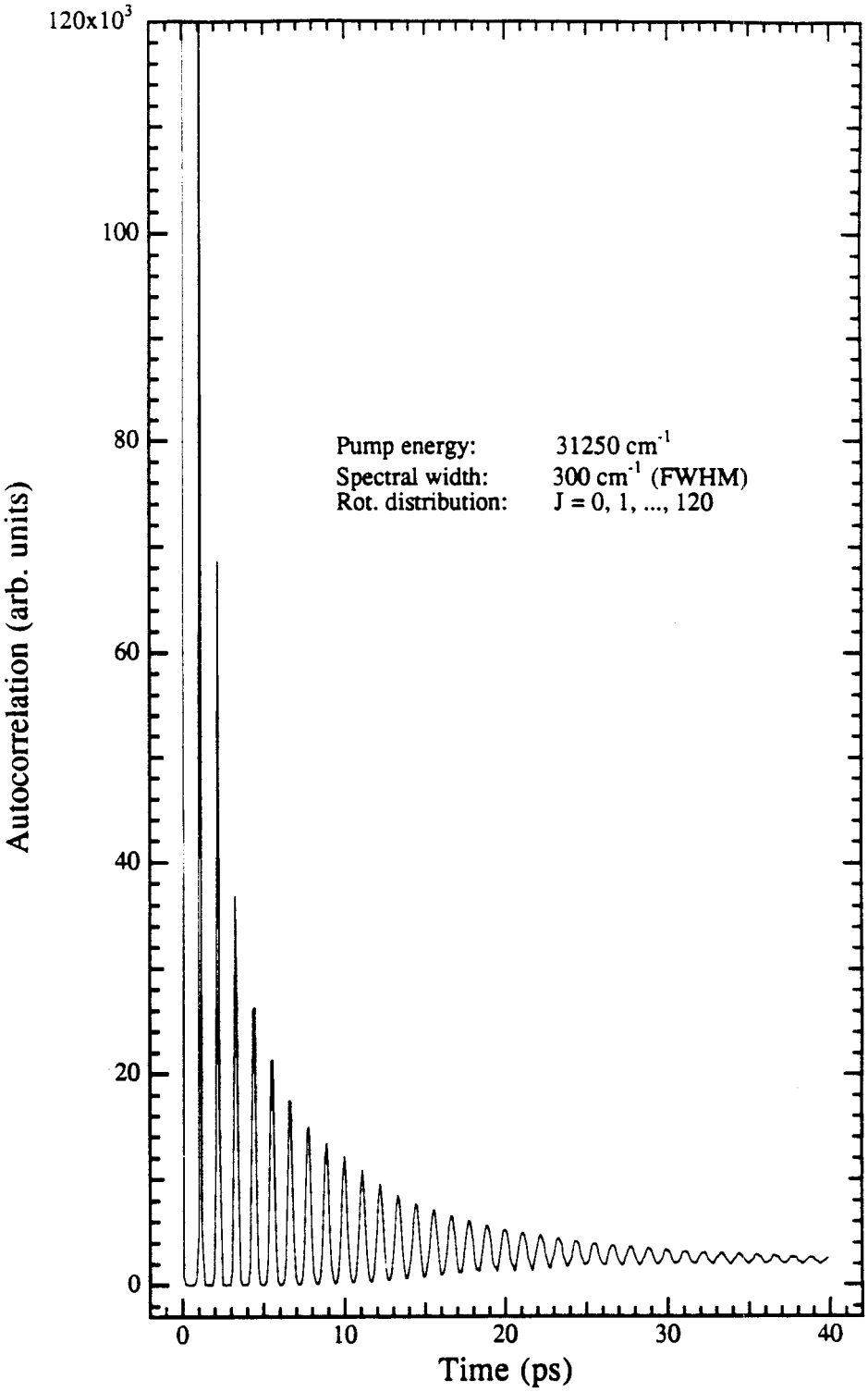
120x10^3
100
80
60
40
20
0
Autocorrelation (arb. units)
Pump energy: 31250 cm^-1
Spectral width: 300 cm^-1 (FWHM)
Rot. distribution: J = 0, 1, ..., 120
0
10
20
30
40
Time (ps)

Figure 5.11

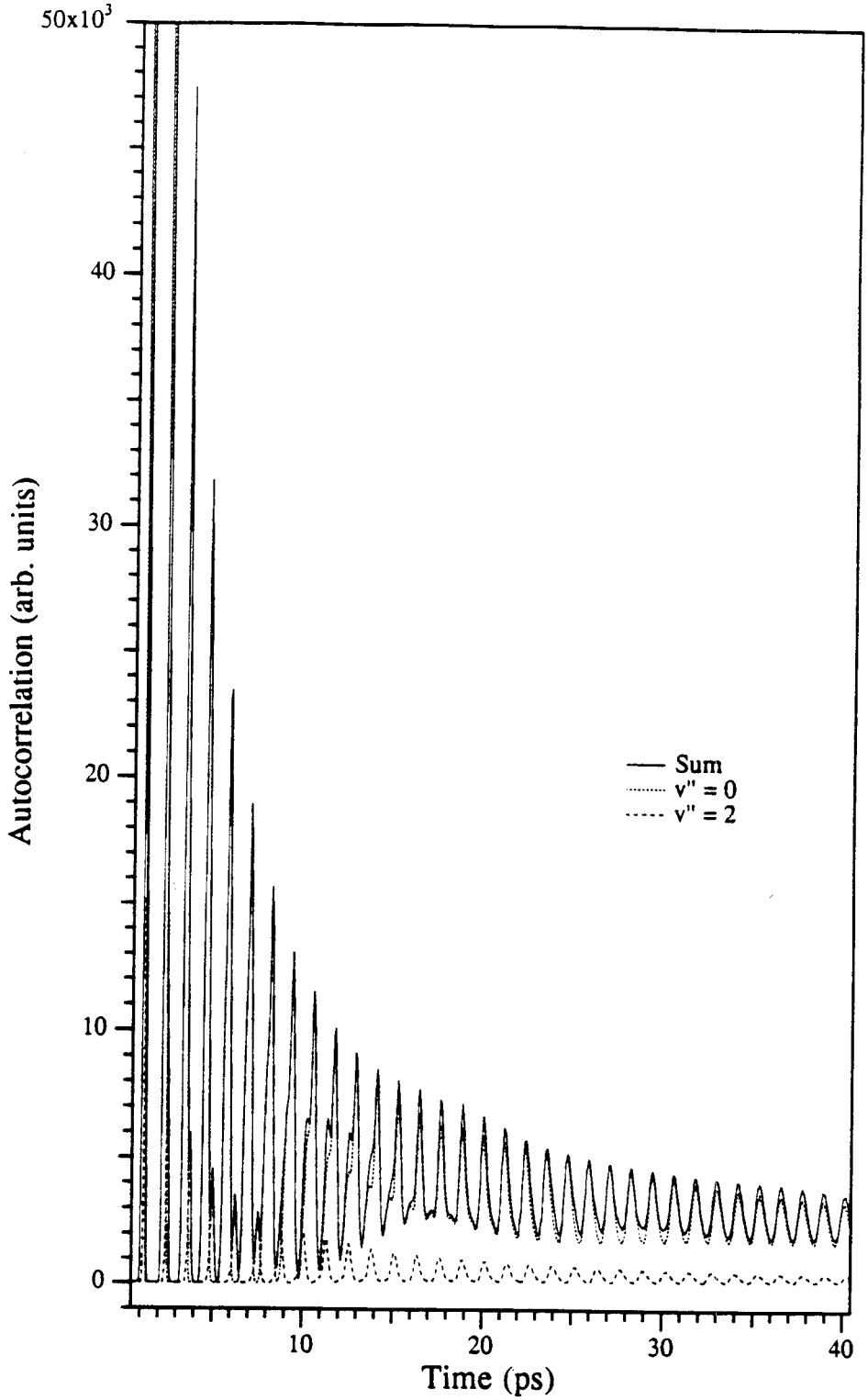
50x10^3
40
30
20
10
0
Autocorrelation (arb. units)
10
20
30
40
Time (ps)
Sum
v" = 0
v" = 2

Figure 5.12

Appendixes

Appendix I

Volume 172, number 2 CHEMICAL PHYSICS LETTERS 31 August 1990

Femtosecond probing of persistent wave packet motion in dissociative reactions: up to 40 ps

P. Cong, A. Mokhtari and A.H. Zewail

Arthur Amos Noyes Laboratory of Chemical Physics [1,2], California Institute of Technology, Pasadena, CA 91125, USA

Received 27 June 1990; in final form 9 July 1990

Femtosecond probing of nuclear motion in an alkali halide (NaI) reaction reveals a persistent wave packet, recurring at long times up to 40 ps. The detection of both "free" Na atoms and "transient" $[Na...I]^*$ indicates non-exponential dynamics through the crossing zone of the covalent and ionic potential energy curves. These observations are related to the nature of the motion, and the level structure making the packet.

On the femtosecond time scale, it is possible to monitor the nuclear motion on a potential energy surface (for recent reviews, see ref. [1]). The traditional picture for describing wave packet dynamics in such molecular systems is the following. After the initial preparation of an "intact" wave packet at time zero on a potential surface, the motion leads to rapid dephasing and spreading, especially if the potential is anharmonic (see e.g. ref. [2,3]). For alkali halides (MX) predissociation reactions [4], an oscillatory motion of the wave packet, due to the avoided crossing between the covalent and ionic potentials (fig. 1), was observed. In view of the fact that these are reactive systems and the potential is very unusual and far from harmonic, two questions are important: how long does the motion persist and what is the nature of the spread of the packet as MX goes to M and X?

In this Letter, we report on a striking observation of wave packet motion in the NaI reaction up to 40 ps. The packet is coherently persistent over these times and, in a simple picture, this time corresponds to a motion distance of about 400 Å. Furthermore, it is shown that the decay of the oscillatory motion of the packets is non-exponential. This decay results from the dephasing of the packet and its leakage of

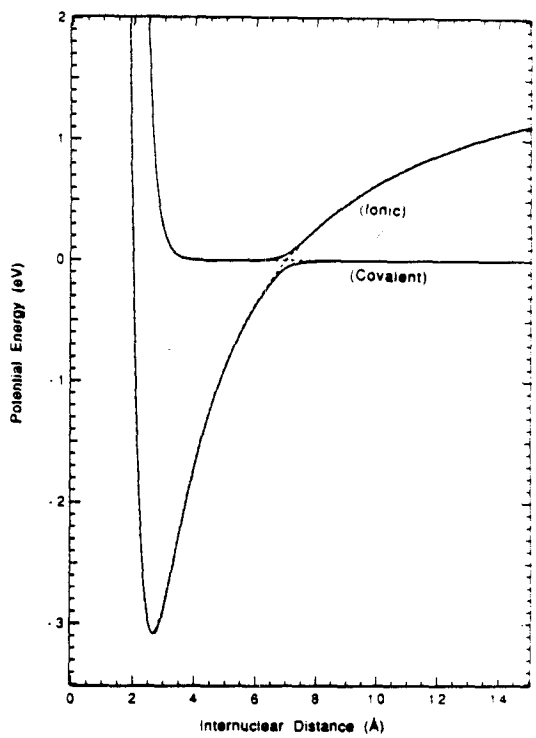

Fig. 1. Potential energy curves of NaI. The solid curves are the adiabatic potentials and the dashed curves are the diabatic ones. These curves are obtained by using the parameters in ref. [4].

[1] This work was supported by the Air Force Office of Scientific Research, and the National Science Foundation.

[2] Contribution No. 8144.

the packet through the (Landau–Zener) avoided crossing between the covalent and ionic potential curves.

The experimental methodology of femtosecond transition-state spectroscopy (FTS) [1], as applied to the study of alkali halide reactions, has been presented elsewhere [4]. Briefly, the laser pulses were generated in a colliding pulse mode-locked ring dye laser (CPM). These pulses (60 fs) were amplified, and were used to generate a continuum; the continuum was filtered and further amplified. As shown before [4], both the free Na atoms and the quasi-bound transition states $[Na...I]^{*}$ can be detected, depending on the detuning of the probe wavelength.

Fig. 2 shows typical FTS transients obtained over the range 0–40 ps. The initial ten oscillations have been observed before [4] and related to the motion between the covalent and ionic curves. The striking new feature here is the apparent continuation (recurrence) of the motion for up to 40 ps. The apparent period remains the same in the range 20–40 ps, but looks "chaotic" in the intermediate region. The overall decay reflects the dephasing and the "leakage" from the avoided crossing zone to form Na+I.

For a bound system (e.g. I_2 in the B state), recurrences have been observed [5]. In that case, the recurrences occur at times precisely determined by the anharmonicity (or in general the difference between adjacent vibrational spacings) of the potential energy curve [6]. Here, the ≈ 30 ps recurrence time does not correspond to the temporally [4] and spectroscopically [7] measured anharmonicity. The anharmonicity (≈ 0.1 cm^{-1}) corresponds to a recurrence time of about 333 ps in this case. Furthermore, rephasing due to rotations [8] of NaI is not possible. This is because rotational rephasing occurs at times determined by $1/2B$ (B is the rotational constant) and this occurs on a time scale an order of magnitude longer; for NaI in the excited state, $B = 745$ MHz [7], time $1/2B = 671$ ps. We have also confirmed this by the lack of polarization effects [8] on the recurrences. The question then is: what is the origin of this persistent motion?

Fig. 3 shows the spreading of the packet and the leakage leading to the formation of Na+I. The oscillations peak amplitude decays faster than the area. In ref. [4], we discussed the effect of the spreading of the wave packet in measuring the actual decay due to the crossing of NaI to form Na+I. However, here it is shown that over the 40 ps time scale, both the decay and the rise of free Na are non-exponential and that we can now separate the population build-up from the dephasing. The $\tau = 6$ ps, measured for the decay of the area and build-up of Na population (at shorter times) gives the probability for the diabatic crossing to form Na+I [4] [#1]. On the other hand, the peak decay indicates that the initial dephasing is faster (3 ps), and this explains some features of the quantum [9,10] versus classical [4,11] calculations, and the linear-response [12] and semiclassical [13] findings.

The non-exponentiality of the decay reflects the different resonant states in the potential well. Since the quasi-bound states of the well interact with the ground state, different predissociation lifetimes are expected, depending on the effective coupling, as shown rigorously by Child [14]. This well-defined coupling establishes the nature of the eigenstates composing the packet. We have considered the following packet:

$$\Psi(R, t) = \sum_n A_n \Phi_n(R) \exp(-iE_n t/\hbar) , \qquad (1)$$

where R is the reaction coordinate (fig. 1) and A_n is the amplitude. This amplitude is determined by the distribution of eigenstates in the adiabatic well (Franck–Condon factors) and the pulse shape.

The "exact" FTS signal has been calculated [15] over these times using the potential of ref. [4] and the time-dependent methodology of Metiu and coworkers and Gruebele et al. [6,9,16]. However, here we discuss a simplified picture that illustrates the physics. From eq. (1), the signal is written as

$$S(t) = \int_{R_1}^{R_2} |\Psi(R, t)|^2 g(R)\, dR , \qquad (2)$$

where the integration is over the range of R probed, determined by the probe pulse. This window in R is

[#1] Recently, we have measured the Landau–Zener escaping probability (P) in the region from 300 to 330 nm. Over this region, the relationship between ln P versus inverse recoil velocity gives a coupling matrix element of 380 cm^{-1}, consistent with the results in ref. [4].

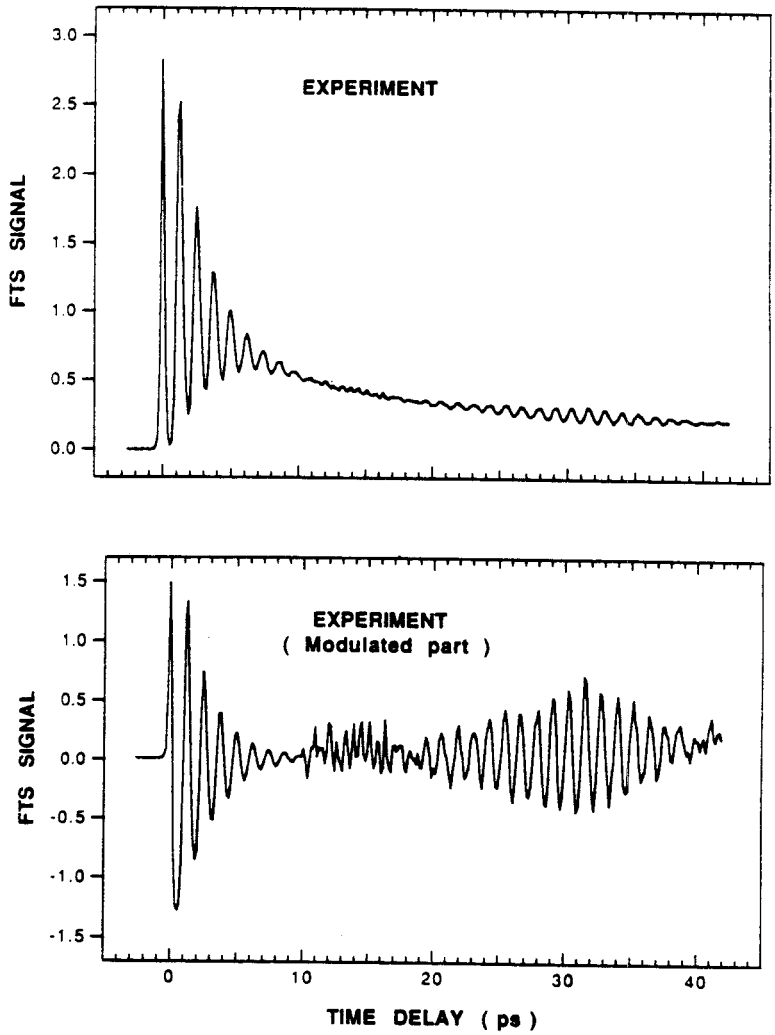

Fig. 2. Top: Experimental FTS of transient $[Na...I]^{**}$ over the range 0–40 ps. The pump wavelength was at 310 nm, while the probe wavelength was at 620 nm. Similar experiments were performed at different pump wavelengths (see text). Bottom: Modulated part of experimental FTS obtained by subtracting the decay caused by dephasing and (Landau–Zener) leaking of the wave packet. Note that the signal after 10 ps was multiplied by 10 for clarity.

typically <0.5 Å wide and $g(R)$, taken to be Gaussian, reflects the probe pulse profile.

If we use a Gaussian envelope for A_n with a distribution of states determined by the measured anharmonicity, then we obtain a signal reflecting a packet motion that recurs at a time determined only by the anharmonicity, i.e. full recurrence. (For a square envelope preparation, partial recurrences at times shorter than the inverse of the anharmonicity are obtained; recall that the Fourier transform of a

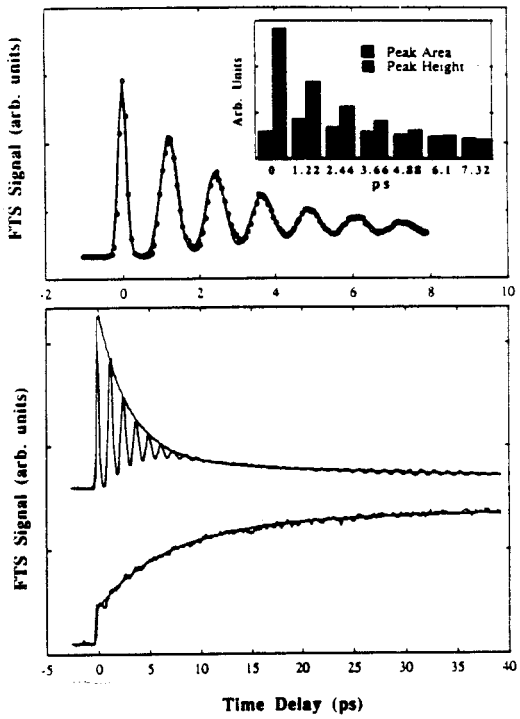

Fig. 3. Decay of transient $[Na...I]^{*}$ and build-up of Na. Top: The first seven oscillations were fitted by a sum of Gaussian functions, each of them was matched to one oscillation. The area covered by each Gaussian and the peak amplitude were plotted against time in the insert. As can be seen from the graph, the peak amplitude decays faster than the area. Bottom: On- and off-resonance FTS transients over the 40 ps range, fitted using a bi-exponential function. The slow components of the two transients are basically the same (47 ps and 40 ps for off- and on-resonance transients, respectively). The off-resonance signal amplitude has a fast-component of 3 ps, but its area decays by 6 ps, which is similar to the fast rise time of free Na.

square pulse in energy gives side bands in time, which can cause partial recurrences.) Clearly, we cannot account for the ≈ 30 ps recurrence by this simple distribution idea. We then considered the nature of the distribution of the Φ_n states by obtaining the eigenfunctions of the potential in ref. [4] and calculating the Franck–Condon factors.

The above equation (1) does not give the decay of the individual n state of the packet. If we now consider all adiabatic states reached by the pulse and take into consideration that the states of the packet have different decay rates (to Na and I), Γ_n, then eq. (1) will include $\exp(-\frac{1}{2}\Gamma_n t)$. With a distribution of Γ_n similar to that of ref. [7], which was obtained by Child's method of analysis [14], we obtain a signal reflecting recurrences at ≈ 30 ps (fig. 4). Also, in fig. 4 we show the effect of the initial population in the $v'' = 0$, 1 and 2 on the observed signal.

The physics is clear. The initial preparation on the femtosecond time scale creates a packet that is localized and spans the states of the adiabatic well. As time goes on, the packet oscillates in the well for the first ≈ 10 ps, and decays by the leakage probability

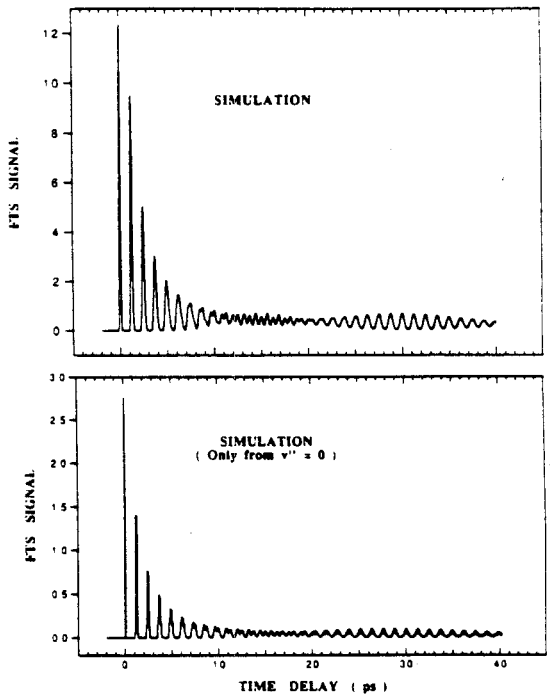

Fig. 4. Simulation of the FTS experiment in NaI, using the potentials in ref. [4]. The exciting pulse (60 fs) has a spectral width of 250 cm^{-1} around 310 nm. The pulse prepares an initial coherent superposition of the eigenstates of the adiabatic well (eq. (1)). The local average vibrational spacing is 27 cm^{-1}. The prepared states have different lifetimes, ranging from typically 1 to 600 ps. In the packet, the short-lived states decay within 10 ps, while the sets of long-lived states, separated by ≈ 270 cm^{-1} (i.e. 10 quantum numbers), are responsible for the rephasing observed around 30 ps. In the top part, the signal is averaged over the thermally populated levels $v'' = 0$, 1 and 2 in the ground state, while in the bottom part the contribution of the single level $v'' = 0$ is given.

to form Na + I. In this domain of time, all short-lived states have essentially decayed, but the long-lived ones are dephasing ("chaotic" or weak signal region) and rephasing (recurrence at the 30 ps region). Thus, the Fourier transform of the FTS signal provides not only the local frequency of the packet oscillation in the well, but also the distribution in the packet levels and the decay characteristics. The early time behavior can be reproduced by classical mechanics [4]. The dephasing and spread in the "chaotic" region are difficult to understand without using the quantized packet of eq. (1).

We have done a number of experiments and calculations to test these ideas. Tuning the probe still shows these long time recurrences. Tuning the pump, however, changes the fundamental period of the oscillation as reported before [4], and also changes the recurrence time: Over the range 290 to 334 nm we observed a recurrence time of ≈ 24 ps (at 290 nm) to ≈ 30 ps (at 310 nm) to ≈ 26–27 ps (at 328 nm). Changing the relative polarization of the pump and probe pulses did not change the phase of the recurrences. These and other experiments like pulse intensity effects and temperature dependences will be detailed later. Finally, we have considered the effect of rephasing between packets initiating from different v'' states. As can be seen from fig. 4, this type of rephasing can lead to an enhancement of the signal in the recurrence region. These points will be discussed in a forthcoming paper.

In conclusion, the persistent evolution of wave packets in reactions of alkali halides is reported. These striking observations in molecular systems reveal the nature of the wave function and the nuclear motion on the surface: oscillations, dephasing and recurrences. The results can be related to the level structure of the packet, but more importantly they indicate the nature of the dynamics at short and long times.

Note. In a beautiful paper by S. Chapman and M.S. Child (private communication) we have learned of the semiclassical treatment of NaI predissociation. Chapman and Child identified the actual levels and decay rates and obtained the delayed recurrences. In our full account of this work quantitive comparison with theory will be made at different energies in order to derive a more accurate potential.

References

[1] A.H. Zewail, Science 242 (1988) 1645;
A.H. Zewail and R.B. Bernstein, Chem. Eng. News 66 (1988) 24;
L.R. Khundkar and A.H. Zewail, Ann. Rev. Phys. Chem. 41 (1990) 15;
M. Gruebele and A.H. Zewail, Phys. Today 43, No. 5 (1990) 24.

[2] E.J. Heller, Accounts Chem. Res. 14 (1981) 368.

[3] D. Imre, J.L. Kinsey, A. Sinha and J. Krenos, J. Phys. Chem. 88 (1984) 3956.

[4] T.S. Rose, M.J. Rosker and A.H. Zewail, J. Chem. Phys. 88 (1988) 6672; 91 (1989) 7415;
M.J. Rosker, T.S. Rose and A.H. Zewail, Chem. Phys. Letters 146 (1988) 175.

[5] R.M. Bowman, M. Dantus and A. H. Zewail, Chem. Phys. Letters 161 (1989) 297;
M. Dantus, R.M. Bowman and A.H. Zewail, Nature 343 (1990) 737.

[6] M. Gruebele, G. Roberts, M. Dantus, R.M. Bowman and A.H. Zewail, Chem. Phys. Letters 166 (1990) 459.

[7] S.H. Schaefer, D. Bender and E. Tiemann, Chem. Phys. 89 (1984) 65; Chem. Phys. Letters 92 (1982) 273.

[8] P.M. Felker and A.H. Zewail, J. Chem. Phys. 86 (1987) 2460;
J.S. Baskin, P.M. Felker and A.H. Zewail, J. Chem. Phys. 86 (1987) 2483.

[9] V. Engel, H. Metiu, R. Almeida, R.A. Marcus and A.H. Zewail, Chem. Phys. Letters 152 (1988) 1;
V. Engel and H. Metiu, J. Chem. Phys. 90 (1989) 6116.

[10] S.E. Choi and J.C. Light, J. Chem. Phys. 90 (1989) 2593.

[11] S.-Y. Lee, W.T. Pollard and R.A. Mathies, J. Chem. Phys. 90 (1989) 6146.

[12] S.H. Lin and B. Fain, Chem. Phys. Letters 155 (1989) 216.

[13] R.A. Marcus, Chem. Phys. Letters 152 (1988) 8.

[14] M.S. Child, in: Semiclassical methods in molecular scattering and spectroscopy, ed. M.S. Child (Reidel, Dordrecht, 1980) p. 127, and references therein.

[15] Work in progress.

[16] M. Gruebele, G. Roberts and A.H. Zewail, Phil. Trans. Roy. Soc. London A (1990), in press.

Appendix II

Direct femtosecond mapping of trajectories in a chemical reaction

A. Mokhtari, P. Cong, J. L. Herek & A. H. Zewail

Arthur Amos Noyes Laboratory of Chemical Physics,
California Institute of Technology, Pasadena, California 91125, USA

IN chemical reactions, the dynamics of the transition from reagents to products can be described by the trajectories of particles (or rigorously, of quantum mechanical wave packets) moving on a potential-energy surface. Here we use femtosecond pulsed laser techniques to follow directly the evolution in space and time of such trajectories during the breakage of a chemical bond in the dissociation of sodium iodide. The bond breakage can be described in terms of the time evolution of a single reaction coordinate, the internuclear separation. As the velocities of the separating fragments are typically of the order of a kilometre per second, a time resolution of a few tens of femtoseconds is required[1,2] to view the motions on a molecular distance scale of less than an ångstrom. The resolution obtained here permits the direct visualization of the wave packet's motion and provides snapshots of the trajectories along the reaction coordinate.

The potential-energy surface (PES) for the NaI reaction (Fig. 1) involves two channels; one describes the covalent character of the bond ($Na + I$) and the other the ionic character ($Na^+ + I^-$). The two potential curves intersect at an internuclear separation R of 7 Å. When NaI is promoted with a femtosecond (pump) pulse to the covalent curve at $R \simeq 2.7$ Å, the wavefunction (or, more accurately, the wave packet) moves towards the ionic curve and then returns with a period determined by the shape of the PES and the total energy in the bond[3,4]. Using a femtosecond probe pulse, we can monitor the oscillation of this activated complex[5], $[Na\cdots I]^{\ddagger}$, as it decays, on a picosecond timescale, to give Na and I (Fig. 1 inset).

Figure 2 shows trajectories in the R-t domain. Both classical newtonian mechanics[3,4,6] and quantum mechanics[7] calculations have been performed; here we consider the former approach to illustrate the methodology. As shown in Fig. 2, the wave packet changes direction as R and t change, starting from the initial time zero at $R \simeq 2.7$ Å. After half a period the packet has reached the ionic turning point, and after a complete period it has returned to the covalent turning point. At or near the ionic-covalent crossing, the packet splits; some continues to move in the direction of increasing R, becoming Na and I, and the rest remains as $[Na\cdots I]^{\ddagger}$, oscillating between the covalent and ionic points. (See also Fig. 1.)

To observe the motion of the trajectories, a window in $R(t)$ must be opened with sufficient distance resolution ΔR to allow us to view the directionality of the packet at different times. If the window is stepped continuously along R, then we can map out the motion and characteristics of the PES. For a given resolution, the temporal motion represents a 'snapshot' of the

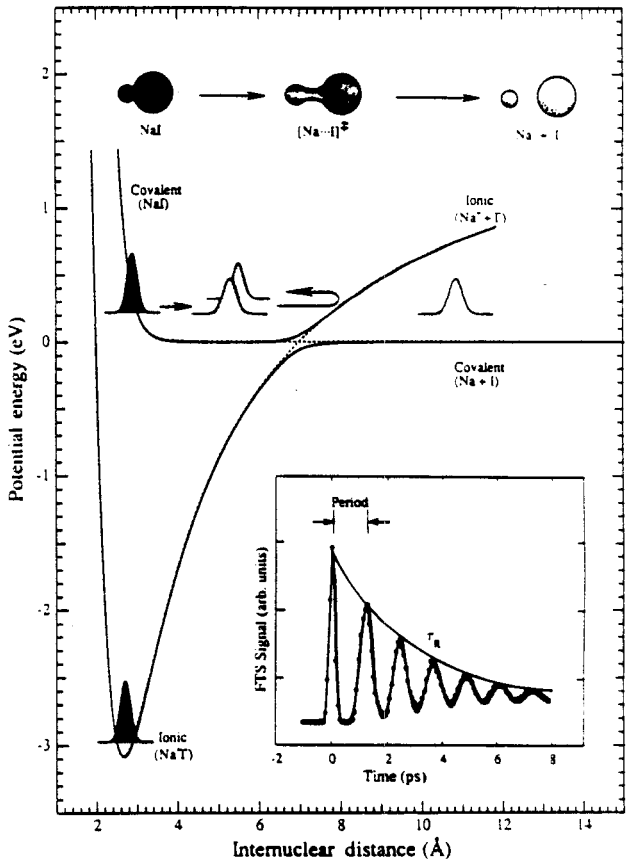

FIG. 1 Schematic diagram of the wave-packet motion in the dissociation reaction of NaI. The femtosecond pump pulse 'transfers' the ground-state wavefunction to the adiabatic potential formed by the avoided crossing of the ionic and covalent curves. The wave packet then moves back and forth, leaking a little (~10%) to Na + I every time it approaches the crossing region. The probe femtosecond pulse monitors this oscillatory motion and the decay (τ_R), as shown in the insert.

PES at this particular R. For example, a window at $R = 3$ Å will give the snapshot shown at the bottom of Fig. 2, which is basically the oscillatory motion displayed in Fig. 1. On the other hand, if a snapshot is taken at $R = 4.5$ Å, the oscillatory motion displays a splitting because at this distance the packet is going in and out of the probing ΔR window. At longer R the splitting increases in time, because the distance the trajectory travels is longer. The observation of such splittings would indicate two important points. First, it would mean that the window opened in R is sufficiently narrow[7] to resolve the nuclear motion in and out of that region of the PES. Second, the splitting gives a time (at each R) that is directly related to the clocking time, defined[3] by the distance travelled from time zero to the probing point on the PES.

The experiments required pump and probe pulses tunable between 310 nm and 390 nm, and between 590 nm and 700 nm, respectively. Briefly, a colliding-pulse mode-locked ring dye laser, generating 50-fs pulses around 620 nm, was amplified in a Nd:YAG-pumped four-stage dye amplifier. The output pulses from the amplifier were temporally recompressed in a sequence of four high-refractive-index glass prisms. The tunability on the probe arm was achieved by generating a white-light continuum, and the same procedure was used on the pump arm, except that the light was further amplified in a flowing cell of the appropriate laser dye (pumped by 532-nm pulses from the Nd:YAG source). We used nonlinear doubling and mixing techniques for conversion to ultraviolet. The pump and probe beams were focused in a NaI reaction chamber and the laser-induced fluorescence was collected perpendicular to the propagation direction of the pump and probe beams. The time delay between the pump and probe was controlled by a high-precision Michelson interferometer and the experiments were controlled by a computer. The range of R probed is shown in Fig. 3.

Figure 4 shows our experimental observations for the NaI reaction. The packet was prepared by a femtosecond pulse at a wavelength λ_1. To probe at different R, we used another femtosecond pulse of different wavelength λ_2. For a given total energy in the bond, determined by λ_1, both the time and the λ_2 can be changed systematically to obtain the snapshots at different R. In Fig. 4, we show three snapshots for $\lambda_1 = 391$ nm as examples of the many snapshots we took. The evolution of the splitting as λ_2 decreases (that is, as R increases) is evident. The splitting at $\lambda_2 = 620$ nm, for example, is 350 fs. This gives a clocking time for the packet to reach the window on the PES of 175 fs. The actual distance being probed is 5.6 Å, as determined by the velocity of recoil. The window resolution is very appropriate for the dynamical motion of chemical reactions: the temporal splitting observed gives an experimental $\Delta R = 0.5$ Å on the PES. The potential for these types of reactions is quite flat at intermediate R (see Fig. 1), and therefore even better resolution may be achieved in other reactions.

For NaI dissociation, the probe at λ_2 excites the wave packet to an upper surface corresponding to the $Na^+ + I^-$ channel. The relationship between λ_2 and R is direct if this upper surface is flat at longer R, as discussed in refs 3 and 4. We have determined that there is a well (depth $\approx 1{,}500$ cm^{-1}, which is deeper than the well reported in ref. 10) in the region probed, which allows us to look at the different regions of the PES shown in Fig. 3. For a given λ_2, we can determine characteristics of the covalent curve by changing λ_1—direct clocking on the lower surface.

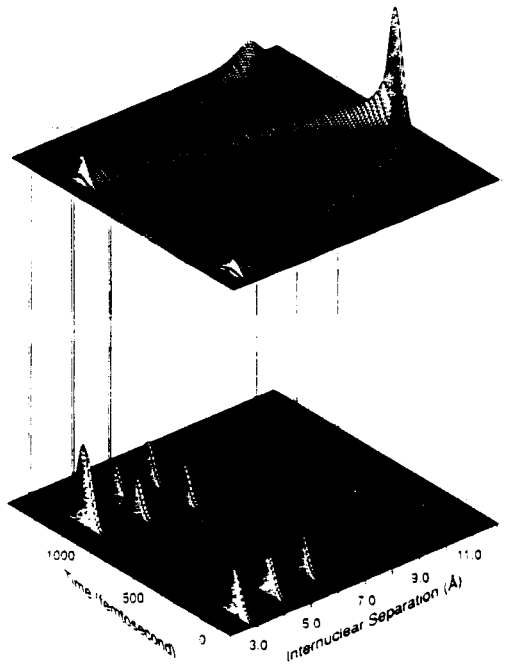

FIG. 2 Classical mechanics simulation of the wave-packet motion with a femtosecond pump pulse at 320 nm. The upper plot shows the wave-packet motion in the two-dimensional space of time and internuclear separation. For simplicity, we do not show the leakage at the crossing point. The lower plot shows the snapshots of the wave-packet motion at different internuclear separations. Note the evolution of the splitting.

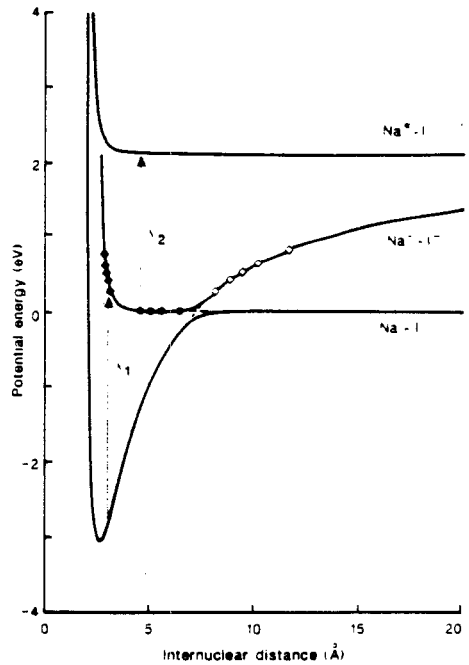

FIG. 3 The range of internuclear distances probed in the experiments. The filled diamonds represent the range that can be reached by pump (λ_1 pulses, the filled circles show the internuclear separations accessed by the probe (λ_2) pulses, and the open diamonds show the points that can be obtained from the oscillation periods. The potentials drawn are taken from ref. 2. We plan to use the snapshots results to deduce more accurate potentials[8].

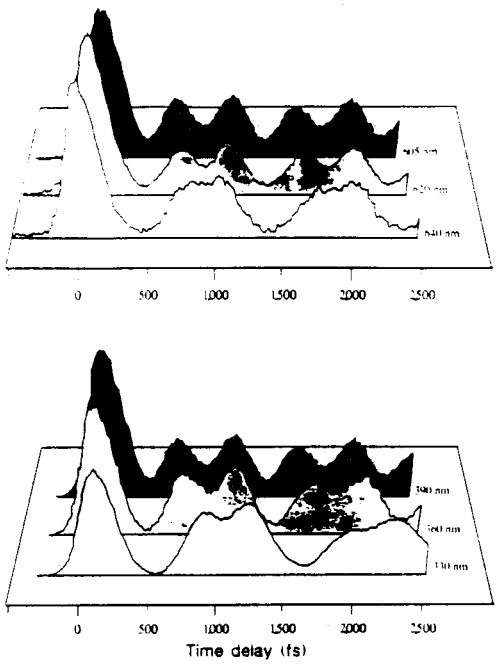

FIG. 4 Experimental femtosecond snapshots of NaI reaction. The upper panel shows the snapshots taken at different probe wavelengths for a wave packet prepared by exciting the NaI molecule at 391 nm (fixed total energy in the bond). The lower panel shows the snapshots taken at a constant λ_2 of 605 nm, while varying the original position (R_0) of the wave packet (different total energies).

Changing the total energy $E_t = \frac{1}{2}\mu v^2$ and repeating the probing gives the motion on different parts of the PES. The reduced mass μ is constant and by changing λ_1 or E_t one changes the velocity of recoil v. As E_t is decreased, we expect the velocity to decrease and the distance travelled by the wave packet, to a given R, to also decrease. Depending on the PES, these two effects determine whether or not the splitting will increase or decrease with E_t. Figure 4 shows three snapshots at different λ_1. We observe an increase in the splitting as E_t is lowered. We also observe a decrease in the period. The latter is consistent with the potential 'narrowing' in R at lower E_t. The former indicates that the covalent side of the potential is very repulsive at short R and is dominated by velocity (not distance) effects, as shown in Fig. 3.

Theoretically, the use of classical mechanics may be sufficient to describe the global motion on the PES. In fact, the results of our experiments and the classical mechanics calculations in Fig. 2 are in agreement. We have, however, done quantum mechanical calculations to justify the agreement between the classical trajectory $R(t)$ and the quantum mechanical expectation value $\langle R(t) \rangle$ (ref. 11). Quantum mechanical calculations at three pump wavelengths, 310 nm, 350 nm and 390 nm indicate that the results agree with those for classical mechanics. The only discrepancy occurs close to the turning point on the steep repulsive branch—this arises because the average position of the wave packet does not reach the classical turning point. Rigorous quantum mechanical calculations of the wave-packet propagation[12] have shown evidence for the splitting; the interpretation did not address the clocking and mapping-of-trajectories aspect of the problem. For NaI, the reduced mass is relatively heavy and the spread of the wave packet, a quantum mechanical feature, is only expected at longer times[11]. More theoretical and experimental work is in progress.

The results reported here show that the motion of the nuclear wave packet during the breaking of the NaI bond can be probed with an experimental resolution of ~0.5 Å of internuclear separation. The position of the probing 'window' can be varied to map the trajectories $R(t)$. The packet is observed in real time for both contraction and extension of the NaI chemical bond as it passes through the window in both directions. The range of internuclear distances probed—up to 6.5 Å on the covalent and 12 Å on the ionic curves—shows the ability of the method to yield direct information on the potential-energy curves at large internuclear separations. This development promises a wide range of applications to other reactions, including those characterized by multidimensional potential-energy surfaces.

Received 12 October; accepted 22 October 1990.

1. Zewail, A. H. *Science* **242**, 1645–1653 (1988).
2. Khundkar, L. R. & Zewail, A. H. *A. Rev. phys. Chem.* **41**, 15–40 (1990).
3. Rose, T. S., Rosker, M. J. & Zewail, A. H. *J. chem. Phys.* **88**, 6672 (1988); **91**, 7415–7436 (1989).
4. Rosker, M. J., Rose, T. S. & Zewail, A. H. *Chem. Phys. Lett.* **146**, 175 (1988).
5. Atkins, P. W. *Physical Chemistry* 4th edn (Oxford University Press, New York, 1990).
6. Lee, S.-Y., Pollard, W. T. & Mathies, R. A. *J. chem. Phys.* **90**, 6146–6150 (1989).
7. Engel, V., Metiu, H., Almeida, R., Marcus, R. A. & Zewail, A. H. *Chem. Phys. Lett.* **152**, 1 (1988).
8. Bernstein, R. B. & Zewail, A. H. *J. chem. Phys.* **90**, 829–842 (1989).
9. Rosker, M. J., Dantus, M. & Zewail, A. H. *Science* **241**, 1200–1202 (1988).
10. Bower, R. D. *et al. J. chem. Phys.* **89**, 4478–4489 (1988).
11. Cong, P., Mokhtari, A. & Zewail, A. H. *Chem. Phys. Lett.* **172**, 109 (1990).
12. Engel, V. & Metiu, H. *J. chem. Phys.* **91**, 1596–1602 (1989).

ACKNOWLEDGEMENTS. This work was supported by the US Air Force.